Equivalence Principle Tests and Direct Searches for Ultra-Light Dark Matter with Fused-Silica Torsion Fibers

Erik A. Shaw

A dissertation submitted in partial fulfillment of the requirements for the degree of:

Doctor of Philosophy

University of Washington

2023

Reading Committee:

Jens Gundlach, Chair

Blayne Heckel

Jason Detwiler

Program Authorized to Offer Degree:

Physics

University of Washington

Abstract

Equivalence Principle Tests and Direct Searches for Ultra-Light Dark Matter with Fused-Silica Torsion Fibers

Erik A. Shaw

Chair of the Supervisory Committee:

Jens H. Gundlach

Department of Physics

Torsion balances are precision instruments for testing gravity and other experiments. However, they are limited by thermal noise and angular readout noise. This dissertation presents research and development in producing and using fused-silica fibers, which can achieve much lower thermal noise. Employing these fibers, we demonstrate significantly improved sensitivity compared to the tungsten fibers we have traditionally used. Combined with new analysis techniques, we used the fibers to perform a dark matter experiment, resulting in new ultra-light dark matter limits. We also demonstrate significant progress towards an improved equivalence principle test. Looking to the future, we can use these fibers to enable various scientific campaigns that significantly improve on important constraints.

Contents

List of Figures

Acknowledgements

I want to acknowledge all the people who have supported me as I did the work presented in this dissertation. This work required continuous support to make it possible. I want to thank my advisor Jens Gundlach and professors, Blayne Heckel and Eric Adelberger, for their input during meetings on resolving issues I faced over the years. And I received much support from fellow grad students, postdocs, and undergraduate students. Mainly, I'd like to thank Charlie Hagedorn, who acted like a second advisor and was actively helpful in furthering work on our Equivalence Principle (EP) test while he was still a grad student and then as a postdoc. More recently, postdoc Conner Gettings has provided much-needed support on the continued development of the EP test after Charlie Hagedorn left. Over the years, I have had many helpful discussions with other grad students like John Lee, Michael Ross (now a postdoc), Matt Turner, Will Terrano, and the postdoc Krishna Venkateswara. Undergraduate students have helped to further aspects of what I have worked on: Joey Turnbull, Kassandra Weber, Jade Cox, Yifei Bai, and Jason Lim. In addition, I thank my family and friends for their support and encouragement throughout my graduate studies and my housemates for not kicking me out of an affordable living situation on a graduate student salary.

Chapter 1

Motivation and Background

> "Whenever an observer detects the local presence of a force that acts on all objects in direct proportion to the inertial mass of each object, that observer is in an accelerated frame of reference." Albert Einstein

The torsion balance was first developed contemporaneously around 1777 by Charles-Augustin de Coulomb [1], who used it to measure the electrostatic force, and by Henry Cavendish [2] to measure the gravitational constant. Since then, it has been used as a cutting-edge instrument to measure weak forces. In recent times, our research group has used it to test the Equivalence Principle (EP) [3, 4, 5, 6, 7, 8], Gravity at short ranges [9, 10, 11, 12, 13, 14], tests of Lorentz symmetry [15, 16, 17, 18] and a measurement of the gravitational constant G [19] with unprecedented precision. This chapter discusses the history of theoretical and experimental developments relevant to our field that motivate a new generation of experimental campaigns to utilize the enhanced sensitivity of fused-silica torsion fibers. We describe in detail how torsion balances can be used to search for EP-violating forces from hypothetical bosons mediating a fifth force and for ultra-light dark matter (ULDM), as well as to set various other important constraints.

1.1 Pre-modern Development of the EP

The topic of how different types of materials fall has fascinated scholars since antiquity. The first attempts to discuss it relied on the intuitive understanding of nature devised by Aristotle, Aristotelian "physics", that posited that heavier objects fall faster towards the center of the universe (which Aristotle thought was the Earth) [20]. Also of note is that religious texts promoted this perspective on cosmology (i.e. geocentrism), and it was, for many centuries, part of the teachings of the Roman Catholic Church. It was not until the Scientific Revolution that empirical science disproved these false ideas. One major event during the Scientific Revolution's start was Nicolai Copernicus's work "De revolutionibus orbium coelestium" which theorized a new heliocentric universe model backed up loosely by observational facts. This work inspired later luminaries in the Scientific Revolution who were excited that empiricism could provide new ways of looking at the world.

Galileo was a proponent of this heliocentric model and also promoted the idea of the universality of free fall, now known as the equivalence principle (EP). His experiments between 1589 and 1592 demonstrated this idea empirically. Allegedly, he dropped iron and wooden balls from the leaning tower of Pisa and observed that acceleration is independent of weight. Following this discovery, which was at odds with the conventional wisdom of Aristotle and the church, Kepler and Newton reiterated Galileo's idea in their theories about planetary motion and gravitation, respectively. In Kepler's "Astronomia Nova", published in 1609, he devised a thought experiment about what would happen if something stopped the Moon in its orbit and dropped it towards the Earth. He correctly assumed, based on Galileo's new intuition, that there was a mutual attraction that would cause both to move towards each other, by amounts d_{M} for the Moon and d_{E} for the Earth, based on the ratio of their masses $m_{\mathrm{M}}/m_{\mathrm{E}} = d_{\mathrm{E}}/d_{\mathrm{M}}$. Newton, in his "Principia Mathematica" published in 1689, defined inertial mass $\boldsymbol{F} = m_i\boldsymbol{a}$ as the proportionality factor that relates the acceleration of an

object to a known applied force. This mass was assumed to be different from the mass in Newton's equation for the gravitational acceleration of a test body, $\boldsymbol{F} = m_i\boldsymbol{a} = Gm_gM\boldsymbol{r}/r^3$, where G is the gravitational constant, m_g is the gravitational mass, M is the gravitational mass of the source, and $\boldsymbol{r}$ is the distance vector from the source to the object in question. Newton's formulas clarified the idea of the universality of free fall as a test of the equivalence of gravitational and inertial mass for all materials, $m_i = m_g$.

This concept opened up the possibility of deriving equations to quantitatively measure the EP. The starting point of a quantitative test is to measure the gravitational mass, and any relevant dimensions or timing uncertainties, of two compositions to determine the scale of the acceleration due to gravity on each composition. In the case of Galileo's test, the time of flight (TOF) of each test mass is $t = \sqrt{2hm_i/(m_gg)}$ where h is the height and g is the gravitational acceleration at the surface of the Earth. If the same relation does not hold for different materials, there would be an observable difference in TOF. It is unclear whether he actually performed a TOF test or just proposed it as a thought experiment, but he also tested this with an inclined plane experiment where issues of air resistance and timing are reduced. Newton tested these ideas with a clever experiment with two pendulums. The basic idea of his experiment is that the period of the pendulum becomes $T = 2\pi\sqrt{Lm_i/(m_gg)}$ where L is the length of the pendulum. Hence, pendulums with the same length will oscillate at slightly different frequencies if this relationship is composition dependent. He put the same weight of different materials in identical boxes and hung them from 11-foot cords. The result was the observation that the pendulums swung in unison for an extended period. Since then, improved versions of these experiments, Galilean and Newtonian [21, 22], have been attempted.

1.2 Modern Developments of the EP

Another theoretical breakthrough of import to the development of tests of the EP was General Relativity (GR). The geometric nature of the theory dictates that $m_i = m_g$ must be true. All particles equivalently move along geodesics according to the geodesic equation

$$\frac{d^2x^\lambda}{dt^2} + \Gamma^\lambda_{\mu\nu}\frac{dx^\mu}{dt}\frac{dx^\nu}{dt} = 0, \tag{1.1}$$

where $\Gamma^\lambda_{\mu\nu}$ are the local Christoffel symbols of the metric that describe how a vector transforms under parallel transport in a curved spacetime, x^μ is the spacetime coordinate of the particle, and t is time. Weinberg noted that this equation can be derived starting from the EP [23]. Additionally, Einstein obtained a critical insight that led to the formulation of GR from a thought experiment positing the equivalence between a gravitational field and an accelerated reference frame. So, precision tests of the EP are an important constraint on the properties of a quantum theory of gravity. Many expect that the EP needs to be violated at some level to unify GR with the Standard Model (SM). GR elevated the EP from a hypothesis based on empirical observations to a central theoretical foundation of our best theory of gravity. GR also leads to the concept of Einstein's EP, which expands on the Weak EP, $m_i = m_g$, with the statement that the outcome of any local non-gravitational experiment in free fall is independent of the velocity and location of the laboratory. Another expansion, the Strong EP, includes that free fall is independent of the gravitational binding energy of a body.

Around the same time, Roland von Eötvös made a significant innovation of central importance to our research group, a torsion balance test of the EP. The torsion balance consisted of a rod suspended horizontally with a fiber with two test masses of different compositions on the ends of the rod, as shown in Figure 1.1. If the EP holds, there would be

no torque due to gravity on the masses. See Appendix A for a derivation of how this setup tests the EP. In short form, the main property of torsion balances is that the thin torsion fibers provide a weak spring sensitive to a minuscule torque about the fiber τ_z, which is given by

$$\tau_z = \frac{(\boldsymbol{r}_B - \boldsymbol{r}_A) \cdot (\boldsymbol{F}_A \times \boldsymbol{F}_B)}{|\boldsymbol{F}_A + \boldsymbol{F}_B|}, \tag{1.2}$$

where $\boldsymbol{F}_A$ and $\boldsymbol{F}_B$ are the forces on the two test bodies. This torque is only sensitive to forces acting in different directions or, alternatively, the difference in magnitude between the projections of the forces onto the plane perpendicular to the fiber axis. Hence, the sensitivity to the Earth's gravitational field comes solely from the centripetal force from Earth's rotation, causing the fiber axis to be slightly off local down resulting in a sideways acceleration on the balance of 1.68 cm/s^2, a factor 583 smaller than $g = 9.8$ m/s^2. If the acceleration due to gravity is different, the net force (centripetal plus gravitational) will point in slightly different directions resulting in a torque and associated differential acceleration with scale set by the lever arm and mass of the composition dipole. Gravity gradients are the main systematic that cause local down to be different for test masses A and B, mimicking the effect of an EP violation. In honor of Eötvös, the field now presents EP results as constraints on the Eötvös parameter

$$\eta = \frac{\Delta a}{\overline{a}} = 2\frac{a_A - a_B}{a_A + a_B}, \tag{1.3}$$

which is the ratio between the differential acceleration on two test bodies $\Delta a = a_A - a_B$ and the average local acceleration $\overline{a} = (a_A + a_B)/2$. Eötvös first achieved a limit of $\eta = 5 \times 10^{-8}$ [24]. Despite sensing a much smaller gravitational acceleration than previous constraints, the sensitivity of torsion balances enabled an improvement of several orders of magnitude. Later Eötvös modified the same basic design to what he called the "horizontal variometer" that had one of the two test masses hanging from a fiber. Pekar and Feteke published results obtained with this apparatus in 1922 [25] achieving a limit of $\approx 2 \times 10^{-9}$.

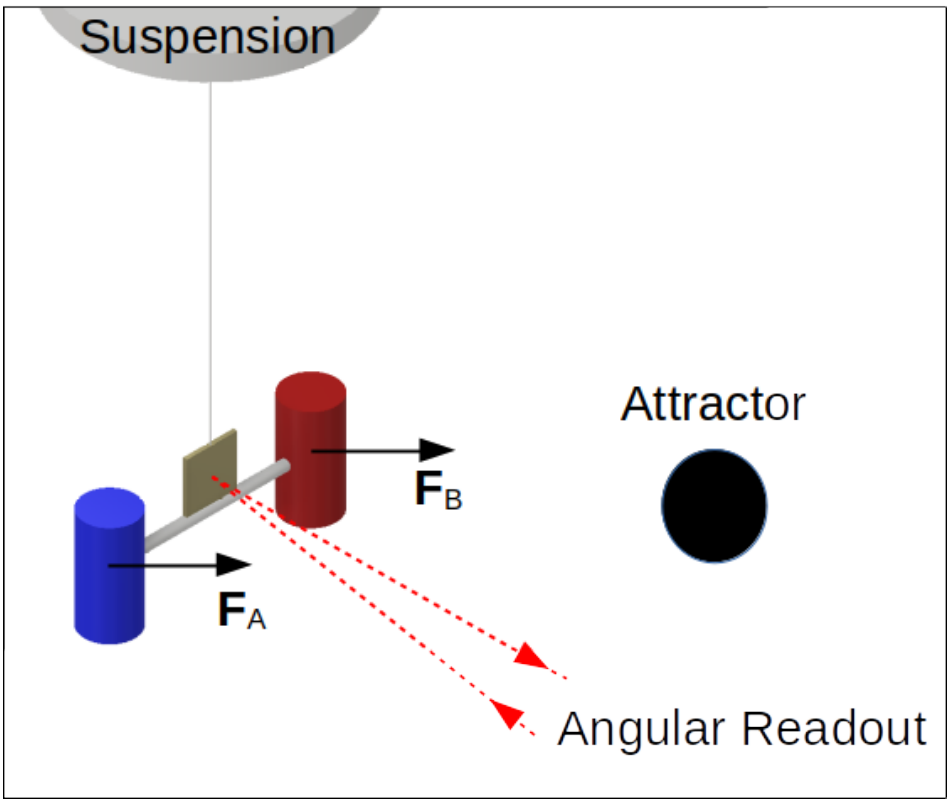

Figure 1.1: Torsion balances consist of a pendulum body suspended with a torsion fiber with two test-mass distributions A and B of different compositions indicated by the blue and red cylinders. The test-masses experience forces $\boldsymbol{F}_A$ and $\boldsymbol{F}_B$ from an attractor, which could be any material. The readout measures the deflection of light off a mirror on the pendulum.

Another major improvement in tests of the EP was the realization by Dicke and others in the 1960s and 70s [26, 27] that for torsion balances, the Sun is as good of a source mass as the Earth. While the Sun signal is somewhat weaker than the Earth signal, the Sun signal is a modulated signal that allows rejection of local gravity gradients and other systematics not modulated once per day. The drawback is that systematics are prominent at this frequency, notably temperature changes, the tilt of the apparatus, and daily variations of the Earth's magnetic field. Addressing these was technically challenging at the time and these tests were already phenomenally precise, constraining $\eta < 10^{-12}$, so research into improvements stalled.

In 1986 Ephraim Fischbach reanalyzed the Eötvös experiment and brought renewed

interest to the field of EP tests [28]. He noted that the Eötvös experiment had tested a wide variety of composition dipoles (Cu-Pt, Magnalium-Pt, Asbestos-Cu, and many more) and came up with a theoretical framework for what could be an explanation for an EP violation seen in different materials based on quantum numbers associated with electrically neutral matter. Because of the differences in binding energies between different electrically-neutral materials, there is a slightly different number of baryons for a given mass of something. Then, if there were a new gauge boson that mediated a force coupled to baryon number, it would introduce a new non-Newtonian component to the potential experienced by a test body in EP tests

$$V_{i,A} = V_G(r)\left(1+\tilde{\alpha}\left(\frac{\tilde{q}}{\mu}\right)_i\left(\frac{\tilde{q}}{\mu}\right)_A e^{-r/\lambda}\right), \tag{1.4}$$

where $\tilde{q}/\mu$ is the charge per atomic mass unit (u), λ is the length scale of the new force, and $V_G(r)$ is the Newtonian potential between a test mass indexed with i and the source distribution A. We parametrize the strength of this new force with the dimensionless strength parameter

$$\tilde{\alpha} = \pm\frac{\tilde{g}^2}{4\pi G u^2}, \tag{1.5}$$

with a novel coupling $\tilde{g}$. Fischbach found that after accounting for the charge B/μ of the compositions tested in the Eötvös experiment, he had found compelling evidence of a new "fifth force" that would not have been obvious looking at the scatter in the measurements in a random order before the advent of quantum mechanics and particle physics. The "fifth force" mediated by this particle was several orders of magnitude less than gravity, with $\tilde{\alpha} = -(7.2 \pm 3.6) \times 10^{-3}$ and $\lambda = 200 \pm 50$ m. At the time, it was plausible that subsequent tests by Dicke had missed this because of the use of the Sun as a source. Other than the strange prediction of a repulsive force and the potential that systematics were the cause of this relationship, there was no compelling reason to dismiss this result. This motivated new terrestrial experiments to test the existence of such an intermediate-range force. Our group started based on this new

framework to conduct EP tests and quickly disproved the result with a novel experimental design [29]. The main achievement was developing a rotating torsion balance to continuously modulate a potential EP signal rather than periodically flipping π rad between equal and opposite EP violation orientations. Another achievement was finding ways to constrain the gravity gradient systematic by designing a more compact, symmetric pendulum and compensating for local field gradients with carefully placed masses around the apparatus. Since then, we have greatly improved the sensitivity by making numerous refinements to the same basic experimental design. We discuss recent improvements in Chapters 2 through 5. Recently there was the first precision space-based test of the EP, MICROSCOPE [30, 31]. This experiment drastically improves on $\eta_{\oplus}$, the Eötvös parameter using the Earth as a long-range source. It is critical to note, however, that terrestrial torsion-balance tests are still valuable due to sensitivity to intermediate-range forces and astrophysical sources and the ability to test a variety of exotic composition dipoles in a shorter time. Figure 1.2 shows an overview of the history of EP test results presented here.

1.3 Other Theoretical Motivations for EP Tests

As noted, Fischbach suggested a parameterization of EP tests based on "charges" per atomic mass unit $(\tilde{q}/\mu)$ of electrically neutral matter, and in particular, he thought there was a coupling to baryon number ($\tilde{q} = B$). More generally, there are several different constituents of atoms of interest; neutrons, N, or protons and electrons, Z. To parametrize results for an arbitrary charge, we generally use the parameter $\tilde{\psi}$ constrained to $-\pi/2 < \tilde{\psi} \leq \pi/2$:

$$\tilde{q}(\tilde{\psi}) = Z\cos\tilde{\psi} + N\sin\tilde{\psi}, \tag{1.6}$$

where for neutral matter $\tan\tilde{\psi} = \tilde{q}_n/(\tilde{q}_e + \tilde{q}_p)$. From this expression, there exists for any material an angle, $\tan\tilde{\psi}_0 = -Z/N$, at which the resultant charge of the material is zero.

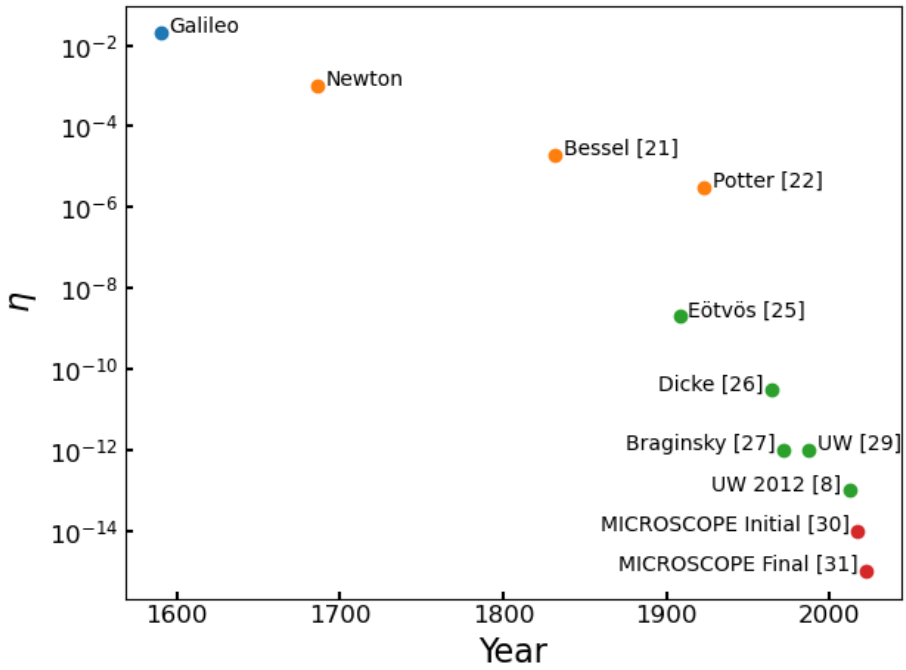

Figure 1.2: Overview of the history of EP tests. Blue denotes Galilean TOF tests, orange are Newtonian pendulum tests, green are Eötvös style torsion balance tests, and brown are the space-based MICROSCOPE experiment.

There are several standard charges B $= \tilde{q}(\pi/4)$, L $= \tilde{q}(0)$, and B-L$=$ N $= \tilde{q}(\pi/2)$ that are particularly well motivated as supersymmetric theories conserve B-L while violating B and L separately. Some models even propose B-L as the charge of a global $U(1)$ symmetry [32]. Other $SO(10)$ unified models predict B-L and B+L violations that could account for baryogenesis [33]. Figure 1.3 shows the variation in these standard charges for common elements with atomic numbers ranging from 1 (hydrogen) to about 82 (lead).

In addition to the basic charges, more exotic combinations could be of interest; one of the few observable predictions of string theory is the existence of Dilatons, a scalar partner to the graviton, that would interact with electrically neutral matter in a way that violates EP. Kaplan and Wise [34] point out that the dilaton would have an observable EP violation in addition to primary dilaton coupling to the gluon field strength, which does not violate EP. Since no observations have confirmed this, we presume that the dilaton is massive, and thus

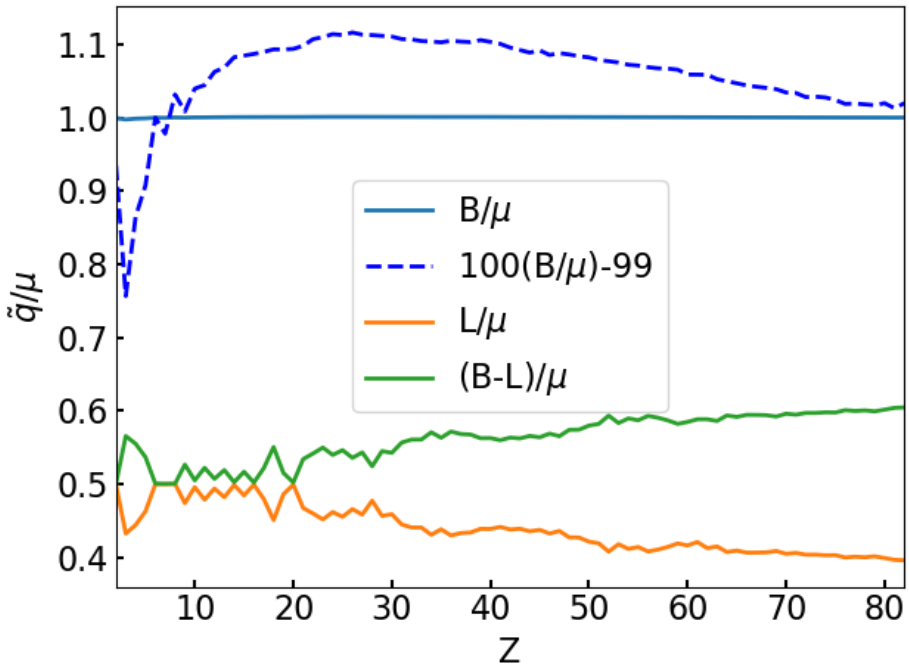

Figure 1.3: Variation of charge values for common elements with $100(B/\mu) - 99$ added as a visual aid to make out the minuscule variations in B/μ.

the coupling has a range as in Equation 1.4.

In addition to the Weak EP, torsion balances can test the Strong EP. The Strong EP includes the idea that gravitational binding energy differences do not affect bodies' gravitational acceleration. Combining results of lunar laser ranging (LLR) [35] with results using a composition dipole that mimics the Earth-Moon charge dipole falling towards the Sun, provides an unambiguous constraint on this principle. Improvements in LLR could motivate a more sensitive measurement with our Earth-Moon pendulum in the future.

Additionally, torsion balance tests are still the most sensitive EP tests using astrophysical sources. As noted MICROSCOPE sets the best long-range constraints towards the Earth. However, our raw sensitivity to differential accelerations is still unmatched, which makes us particularly sensitive to astrophysical sources. The acceleration towards the Sun is 2.8 times smaller than towards the Earth in our experiments (0.6 cm/s^2 vs. 1.68 cm/s^2) but is interesting

given that the Sun consists primarily of hydrogen. Hence, $\left(\frac{L}{\mu}\right) \approx 1$ for the Sun, a factor two times greater than the Earth. We can also analyze data to look for a signal towards the galactic center; estimates are that about 25% of any acceleration towards the galactic center is due to dark matter [36]. While most of the mass is dark matter towards the galactic center, there is also a significant amount of dark matter away from the galactic center that leads to the 25% figure. Hence, this analysis can set EP constraints of ordinary matter accelerating towards galactic dark matter at the level of $\eta_{DM} < 10^{-4}$ [8].

Some argue that EP tests preclude antimatter from accelerating differently from ordinary matter to high precision, which suggests that experiments like AEgIS [37] are unlikely to produce valuable results. In response to the AEgIS proposal, Alves *et al.* [38] concluded that any asymmetry between matter and antimatter was already well constrained by torsion balances. They determined that the antiquark energy fraction carried by nucleons varies significantly between compositions. For example, with a Be-Ti composition dipole, the difference in the nuclear mass fractions is $\approx 10^{-3}$, and antiquarks carry about 10% of the energy in a nucleon. Hence, our EP test constrained the quark-antiquark antimatter asymmetry to better than about 10^{-9}. Presumably the asymmetry would be the same in a hydrogen-antihydrogen test. Nevertheless, the AEgIS collaboration continues to push forward in the hopes of achieving a precision test of the Weak EP with antihydrogen.

Another use for an EP apparatus is testing for Lorentz and charge, parity, and time reversal symmetry (CPT) Violations [15]. These tests search for preferred-frame interactions of numerous forms: $V = -\boldsymbol{\sigma}^e \cdot \boldsymbol{A}$, $V = -B\boldsymbol{\sigma}^e \cdot \boldsymbol{v}/c$, or $V = -\sum \sigma_i^e C_{ij} v_j/c$. Here $\boldsymbol{\sigma}^e$ is the spin dipole, $\boldsymbol{A}$ is a preferred direction with respect to the cosmos, and $\boldsymbol{v}$ the velocity with respect to the cosmic microwave background (CMB). We developed a spin-dipole pendulum that was highly sensitive to such interactions, which contained $\approx 10^{23}$ polarized electrons. These searches are motivated by many different observations. Mainly, the CMB provides a preferred frame, which may lead to measurable effects, so we analyze for accelerations towards the

CMB with various pendulum dipoles. Additionally, Kostelecký's team [39] proposed that such violations could be a signature of modifications to the standard particle model of the constituents of matter, such as string theory. Further work established the sensitivity of an EP test with a spin-polarized dipole coupling to such violations [40].

Another interesting possibility is predicted topological defects in scalar fields that would create "bubblelike" defects surrounding dense objects such as the Earth or the Galactic center [41, 42]. These defects would produce apparent spatial variations in the fundamental constants, in this case, the fine structure constant, that would exert differential accelerations on EP experiments. The theory predicts that the mass of a test body M varies in space and time due to the contributions of the fundamental constants to the mass-energy of electrically neutral matter. This variation leads to an additional acceleration

$$\delta \boldsymbol{a} = -\frac{\boldsymbol{\nabla} M}{M} - \frac{\dot{M}}{M}\boldsymbol{v}, \tag{1.7}$$

where $\mathbf{v}$ is the velocity of the test body. Precision clocks have already constrained temporal variations of fundamental constants with high precision. Future torsion-balance tests may measure some spatial variation.

1.4 Dark Matter Detection with Torsion Balances

1.4.1 Dark Matter Overview

One of the greatest mysteries in physics is what dark matter is. Physicists have fixated on this topic in recent decades, but the history of the idea is much longer than there has been active interest in discovering what it is. The idea that there are things out there we cannot detect dates back to 1884 when Lord Kelvin gave a talk in which he inferred the existence of dark bodies that he estimated to make up most of the mass in the Milky Way [43]. When Fritz

Zwicky analyzed the Coma Cluster in 1933 [44], he found compelling evidence that a large proportion of matter was unaccounted for, which Zwicky coined “dark matter”. It was not until decades after these first hints of dark matter that it became well-established as a central mystery in astrophysics, with detailed studies of rotation curves in the 1960s and 1970s. An influential paper by Vera Rubin and Kent Ford gave an overview of their studies and showed convincingly that most galaxies have about six times more dark matter than visible matter [45].

Recent explorations of dark matter have focused on the possibility that it consists of particles beyond the standard model. This model has the most explanatory power compared to existing theories that modify general relativity. A full accounting of all the evidence is beyond the scope of this dissertation. However, we present a couple of observations here. Perhaps the most dramatic success of modeling dark matter as a new particle is the agreement of the ΛCDM model (Λ is the cosmological constant and CDM stands for cold dark matter) with measurements of the cosmic microwave background [46]. These observations of the CMB also set constraints on the universe’s composition, limiting baryonic matter to be less than 5% of the universe’s energy density, precluding the possibility that unobserved baryonic matter explains dark matter. Another often-cited observation is a weak-lensing mass reconstruction of the Bullet Cluster [47]. Researchers found that a subcluster had fallen through the central cluster causing significant heating and clustering of the ordinary matter (primarily gas). The observed effect was that the lensing predicted a mass peak spatially displaced from the one determined from X-ray observations, pointing to the existence of dark matter that had not merged with the primary cluster after infall. There was such a pronounced difference that modified theories of gravity have long had trouble eliminating the need for a dark matter particle explanation.

The first experimental searches were focused on Weakly Interacting Massive Particles (WIMPs) because of enthusiasm about the "WIMP miracle" [48]. Theorists predicted

supersymmetric partners with electroweak interactions weighing around 10 GeV to a couple of TeV, and calculations show that the creation of such particles during the big bang would account for the abundance we observe today. For more on WIMP constraints, a review article such as by Roszkowski *et al.* [49] would provide more insight than there is space for here. In short, there is little parameter space remaining between current constraints and an irreducible neutrino background [50]. A final generation of detectors may reach that "neutrino fog". Moreover, as stated in the review article, the constraints are already well below the electroweak scale required for the "WIMP miracle" that motivated these searches in the first place. Despite all this, there may still be hope for this candidate with experiments ongoing and plans for upgrades. Unfortunately, after many impressive experiments, no reproducible signal has suggested the existence of WIMPs.

Despite its explanatory power, ΛCDM has some issues predicting many astrophysical observations that further call into question the CDM assumption of that theory in favor of a different sort of dark matter. One long-standing issue is the core/cusp problem [51], which is the discrepancy between N-body simulations and observed distributions of dark matter in low surface brightness disk and gas-rich dwarf galaxies. Namely, observations point to a smoother distribution at the core of these galaxies, whereas N-body simulations that assume CDM predict a sharply cusped distribution. Very light dark matter with astrophysical scale DeBroglie wavelengths is a natural solution to this problem, hypothetically allowing for the observed smoothing. On more careful examination, this claim is questionable [52], but there are also more optimistic analyses of a light candidate [53]. A recent review states consensus has yet to be reached [54]. However, there has been progress in reconciling CDM with existing observational discrepancies. Another problem is anomalies between the predicted and observed brightnesses and positions of multiply lensed images when CDM is assumed [55]. Again, dark matter lighter than CDM provides a solution. There are more observations of note [55]; hence, growing evidence calls into question the CDM assumption.

So, research has refocused around a new class of particles that we term ultra-light dark matter (ULDM) [56]. Nobody agrees on the terminology yet; some call it wave, "fuzzy", ΨDM, bosonic dark matter, or even a virialized ultra-light field (VULF). In any case, for dark matter masses $m_{\rm DM} \leq 1$ eV/c^2, the dark matter number density is large enough that the particles behave more like a classical field than individual particles. Dark matter particles in our galaxy are highly nonrelativistic with a local velocity distribution peaked at $v_{\rm DM} \approx 10^{-3}c$ [57]. As explained below, the field would oscillate at a Compton frequency

$$f_{\rm DM} = \frac{m_{\rm DM}c^2}{h}[1 + (v_{\rm DM}/c)^2/2], \tag{1.8}$$

where c is the speed of light and h is Planck's constant. The second term is the fractional spread $\delta f_{\rm DM}/f_{\rm DM} = (v_{\rm DM}/c)^2 \approx 10^{-6}$. Hence, the field would be coherent for about 10^6 oscillation periods resulting in a coherence time:

$$t_c = 1/\delta f_{\rm DM} = \frac{h}{m_{\rm DM}v_{\rm DM}^2}. \tag{1.9}$$

Say you have a particle with $m_{\rm DM} = 10^{-16}$ eV/c^2. Plugging in you find a coherence time of 2.6 years, a signal with frequency 24.2 mHz oscillating a million times.

Why these dark matter fields oscillate at this particular frequency may need to be clarified. The most straightforward explanation is to start by saying, in the regime of masses of interest, each particle behaves like a wave rather than a particle. This fixed frequency is a fundamental difference between matter waves and light waves that have a fixed velocity c and variable energy. In contrast, matter waves have no fixed velocity and a fixed energy mc^2. De Broglie stated to this point "that to each portion of energy with a proper mass m_0 one may associate a periodic phenomenon of the frequency ν_0, such that one finds: $h\nu_0 = m_0c^2$" [58]. In other words, matter quanta have a fixed frequency. Suppose there are N oscillating matter waves acting on a location in space with random phases. The resultant field has the same frequency,

a random phase, and a total amplitude in the large N limit $\propto \sqrt{N}$. Additionally, in the case of dark matter in our galaxy, the particle waves have a velocity distribution that results in the coherence time of the signal. This is introduced in more detail in Hui [56].

Many have reported searches for ULDM recently. The most interesting candidate is the Peccei-Quinn axion [59] because it would resolve the strong CP problem. The primary experimental technique to detect the axion is axion-to-photon conversion in ultrasensitive electromagnetic cavities immersed in strong magnetic fields [60]. Searches span the mass range 10^{-6} eV/$c^2 \lesssim m_{DM} \lesssim 10^{-3}$ eV/c^2 [61, 62]. Notably, the ADMX collaboration [63] has definitively excluded such dark-matter axions with masses between 2.7 μeV/c^2 and 4.2 μeV/c^2.

Beyond axions, there have been many other constraints. Ultrastable clocks [64, 65] and gravitational-wave detectors [66] constrain the couplings of scalar dilaton ULDM with masses between 10^{-21} and 10^{-5} eV/c^2. Various experimental approaches constrain the couplings of pseudoscalar axion or axion-like ULDM. Spin-precession experiments [67, 68, 69] constrain the coupling of pseudoscalar axion-like ULDM with masses between 10^{-23} and 10^{-18} eV/c^2.

1.4.2 Vector ULDM

Fewer groups have searched for vector ULDM, with most focusing on dark photons [70, 71]. In this dissertation, we present limits on vector ULDM coupled to B-L, B, and L (B and L are baryon number and lepton number, respectively); the B-L coupling is particularly fascinating, as noted in the previous section. A coherent vector boson wave couples to laboratory objects like a time-varying "electric" field $\tilde{\boldsymbol{E}}$ interacting with "charges" $\tilde{q}$ on the objects with a coupling constant $\tilde{g}$. If the dark matter consists predominantly of such bosons, $\tilde{E} \approx \sqrt{\rho_{DM}\hbar c} = 7.7 \times 10^3$ eV/m [72] where $\rho_{DM} \approx 0.3$ GeV/cm^3 is the local dark-matter density assumed for this dissertation. The direction of $\tilde{\boldsymbol{E}}$ is expected to be random but steady

for times less than the coherence time t_c [72, 73]. The force on a "charge" $\tilde{q}$ is

$$\boldsymbol{F}_{DM} = \tilde{q}\tilde{g}(\hbar c)^{-1/2}\tilde{\boldsymbol{E}}. \tag{1.10}$$

For example, the B-L "charge" of a test-body consisting of electrically neutral atoms is $(q_{\mathrm{B-L}}/\mu)(m_T/u) = (N/\mu)(m_T/u)$, where N is the number of neutrons, m_T is the test-body mass, and μ is atomic mass in atomic mass units (u). We search for these forces using a torsion pendulum containing a "charge" dipole. The differential acceleration (force/mass) of the two "charges" is given by

$$\Delta a_{B-L} = g_{B-L}\sqrt{\rho_{DM}}\,\Delta_{B-L}/u\ , \tag{1.11}$$

where $\Delta_{B-L} = (N_1/\mu_1) - (N_2/\mu_2)$ is the difference in the charge-to-mass ratios of the two atomic species in the dipole. This differential acceleration and details of the pendulum predict the ULDM torque signal on a torsion balance, which we describe in more detail in Chapter 6.

1.4.3 Spin-coupled ULDM

For spin-coupled ULDM we often use the term axion, but this is not the Peccei-Quinn axion. These particles are sometimes termed axion-like particles (ALPs), a class of pseudoscalar particles with numerous couplings to ordinary matter. In this case, the axion "wind" couples to spin-polarized material on the pendulum, producing effects proportional to the velocity $\boldsymbol{v}_a$ of the axion wave relative to our lab. This velocity could have any direction in the solar system frame, and we neglect the small seasonal variation in this velocity in the lab as the Earth orbits the Sun. So, for calculations in this dissertation, this is a constant vector in some random direction. The effect of this relative motion on a torsion balance with a spin-dipole

generated by N_e polarized electrons produces an effective Hamiltonian

$$H_{\text{eff}} = C_e \frac{\tilde{a}_0}{2F_a} \sin(2\pi f_a t + \phi_a) \frac{(\boldsymbol{v_a} \cdot \boldsymbol{\sigma_e})}{c}, \tag{1.12}$$

where C_e is a dimensionless parameter characterizing the ULDM coupling strength to electrons and F_a is the symmetry-breaking scale. The other parameters $\boldsymbol{v}_a$, $\boldsymbol{\sigma}_e$, and ϕ_a are the velocity of the "wind", the spin dipole, and phase of the spin-coupled bosons, respectively. This effective Hamiltonian produces a potential energy on a torsion balance dependent on how well aligned the spin dipole is with the axion "wind", and the angular derivative of this expression is the torque, $E(\phi_{\text{TT}}) \propto \boldsymbol{v_a} \cdot \boldsymbol{\sigma_e} = N_e |\boldsymbol{v_a}| \cos\phi_{\text{TT}} \Rightarrow \tau(\phi_{\text{TT}}) \propto -N_e |\boldsymbol{v_a}| \sin\phi_{\text{TT}}$. Assuming the same local dark matter density as the previous section $a_0 = \sqrt{2\rho_{DM}(\hbar c)^3} \approx 2.2 \times 10^{-3}$ eV^2. The main time variation is at the Compton frequency f_a, but $\boldsymbol{\sigma_e}$ also varies as the Earth rotates.

Chapter 2

Noise Sources

This chapter introduces the two primary intrinsic noise sources of torsion balances, the thermal noise limit of the fiber and the angular readout noise, and how to improve them. It also discusses a variety of background noise sources that impact torsion balance experiments and how to mitigate them to reach the intrinsic noise.

2.1 Equation of Motion and Thermal Noise

An essential consideration in the design of any experiment is noise sources. Modern torsion-balance experiments reach two intrinsic noise limits. The torsion balance's mechanical noise is the primary intrinsic noise source that is hard to improve. Saulson [74] thoroughly treats mechanical noise in a torsion oscillator and other mechanical systems. Here we will outline the main points relevant to torsion balances.

We model torsion balance dynamics by the differential equation for an internally and externally damped harmonic oscillator

$$I\ddot{\theta}(t) + \nu\dot{\theta}(t) + \kappa\left(1 + \frac{i}{Q_i}\right)\theta(t) = \tau(t), \tag{2.1}$$

where $\theta(t)$ is the angular displacement, $\tau(t)$ is the external torque on the pendulum, I is the moment of inertia of the balance, ν is the velocity damping constant, κ is the torsion constant and Q_i is the internal quality factor. The other quality factor impacting loss is velocity damping $Q_v = I\omega_0/\nu$ where $\omega_0 = \sqrt{\kappa/I}$ is the resonant frequency. In our experiments, we have usually addressed all external damping sources such that $\nu \to 0$. For large amplitudes and neglecting torque noise, the general solution to this differential equation when external torques are minimal is

$$\theta(t) = e^{-\alpha t}(a\cos\omega_0 t + b\sin\omega_0 t), \tag{2.2}$$

where the exponential decay rate is related to Q_i via $\alpha^{-1} = 2Q_i/\omega_0$. From this, we see that the quality factor relates to the number of oscillations it takes for internal damping to reduce the amplitude of the oscillations by a factor of $1/e$. From the equation of motion we can derive the response of a torsion pendulum by using a Fourier expansion of $\tau(t)$, $\tau(\omega) = \left(-I\omega^2 + \kappa(1 + i/Q_i)\right)\theta(\omega)$ and the response function is then defined as

$$\Lambda(\omega) \equiv \frac{\kappa\theta(\omega)}{\tau(\omega)} = \frac{1}{(1-\omega^2/\omega_0^2) + i/Q_i}. \tag{2.3}$$

Using the response and the fluctuation-dissipation theorem, we find that $\tau_{th}^2(\omega) = 4k_BTR(\omega)$ where $R(\omega) = \mathrm{Re}[\kappa/(i\omega\Lambda)]$ is the real resistance of the mechanical system [74]. Plugging in, we find that for internal damping

$$\tau_{th}(\omega) = \sqrt{\frac{4k_BT\kappa}{\omega Q_i}}, \tag{2.4}$$

and multiplying by $|\Lambda|/\kappa$ we find the thermal noise spectrum of the twist angle

$$\theta_{th}(\omega) = \sqrt{\frac{4k_BT}{\kappa\omega Q_i}}\frac{1}{\sqrt{(1-\omega^2/\omega_0^2)^2 + 1/Q_i^2}}. \tag{2.5}$$

As can be seen from this equation, there are several avenues to address this noise source: modulate the signal of interest at a higher frequency, reduce the temperature of the experiment T, make a weaker spring κ, and use a lossless material with high Q as the torsion fiber. Figure 2.1 shows the difference in the angle response of two fibers holding the same pendulum.

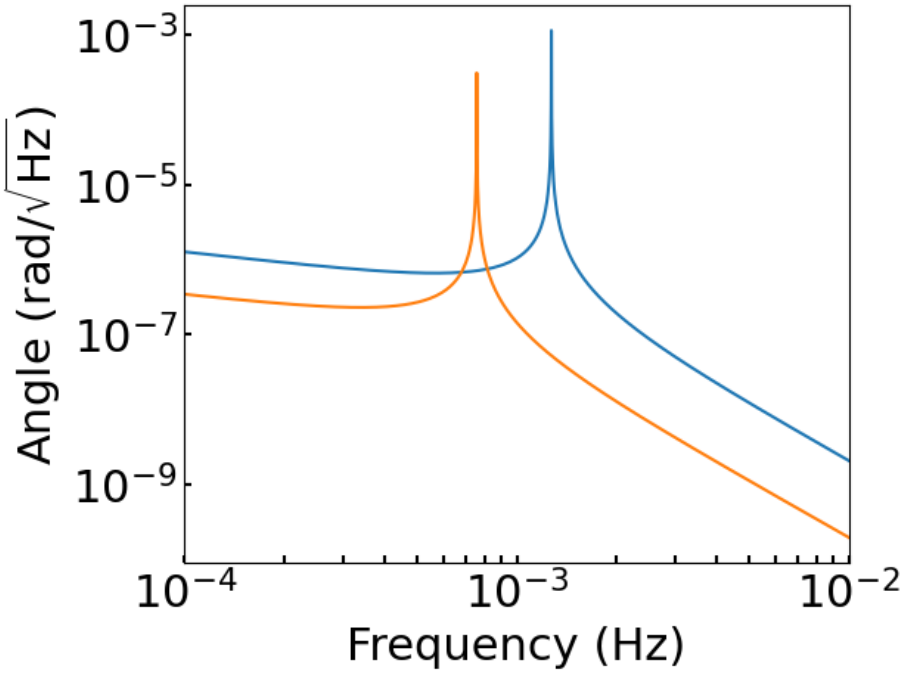

Figure 2.1: Example angle noise of two torsion balances. A tungsten fiber (blue) with $Q = 6,700$ and $\kappa = 2.4$ nJ/rad. And a fused-silica fiber (orange) with $Q = 260,000$ and $\kappa = 0.86$ nJ/rad. These fibers are discussed more in Chapter 3. The pendulum has $I = 3.78 \times 10^{-5}$ kg m^2.

In the context of equivalence principle (EP) tests, the apparatus is rotated with a precision turntable to look for a signal from various sources. It is a challenge to reduce thermal noise by running much faster, but possible. Additionally, as discussed in the next section, the angular readout noise dominates at higher frequencies, thus limiting the benefit of running faster. We actively research both of these possibilities.

A cryogenic torsion balance is possible [75, 76]. However, it is a significant challenge to

design an apparatus that is cooled uniformly, mitigates excess vibrational coupling from the cooling system, and can run stably for the months needed for a science measurement. Our group has demonstrated that we can reach thermal noise in a cryogenic experiment [76], but we could not avoid temperature gradients across the length of the fiber. These gradients led to a higher thermal noise than expected. Another challenge that is in the future for cryogenic experiments is designing a rotational feedthrough that is smooth enough to enable a precision EP measurement. Currently, cryogenic torsion balances can only look at astrophysical signals modulated at the daily frequency, a frequency roughly two orders of magnitude lower in frequency than our turntable generally rotates, hence a 6-10 times higher thermal noise than can be achieved with modern EP tests, along with significant systematic backgrounds. There has been speculation [77], however, that cooper pairs violate the Weak EP due to a breaking of gauge-invariance within superconductors. Testing this possibility with the Sun is possible and there is ongoing work to get publishable results. More research and development is needed to attain results of interest from a cryogenic apparatus.

Making a weaker spring is an attractive option though it has limitations as the fiber also needs to hold the balance. Generally, a weaker spring also means a lighter balance with a smaller coupling to signals of interest. The torsion constant of a given fiber is

$$\kappa = \frac{\pi \mu d^4}{32l}, \tag{2.6}$$

where μ is the shear modulus of the material, d and l are the diameter and length of the fiber, respectively. A material with a lower shear modulus will generally have a lower tensile strength and hold less weight. A thinner fiber will also hold less as the strain on the fiber increases proportional to the decrease in the cross-sectional area. Length is the only parameter that does not necessarily change the tensile strength. A uniform-diameter fiber with any length will hold the same load. To get the best performance for any given material,

we make a uniform fiber that is thick enough to hold the load and is as long as practical to achieve adequate vacuum pressures with additional vacuum volume and avoid systematics that would scale with the length of the fiber.

2.2 Angular Readout Design and Noise

Angular readouts are helpful in many areas of physics. For the Eöt-Wash group, they are an essential component to improve. We look for torques or differential accelerations on the pendulum for our science results. A method of measuring differential acceleration directly via, for example, differential accelerometers with remote readouts does not seem promising; commercially available accelerometers achieve noise of around 100 μm $s^{-2}/\sqrt{Hz}$ whereas torsion balances with an angular readout achieve pm $s^{-2}/\sqrt{Hz}$ noise. Hence, the best avenue to improve the readout is to improve measurements of minuscule angular deflections and then use the angular response of the pendulum to infer the torque.

Figure 2.2 shows the most basic idea for an angular readout, an optical lever. A displacement on the detector, Δy, is related to the angular displacement, $\Delta\theta$, by $\Delta\theta \approx \Delta y/(2l)$ where l is the distance from the primary mirror to the detector. A large lever arm is the simplest way to achieve high sensitivity to angular deflections.

The main drawback of this design is its sensitivity to displacements. Moving the main mirror by Δx along the direction normal to the detector surface also moves the beam spot on the detector an amount $\Delta y = 2\theta\Delta x$. The pendulum swing mode is a significant signal with this angular readout. Modifications to this design that mitigate displacement sensitivity are our traditional autocollimator [78] and the multi-slit autocollimator [79].

The inherent noise of every optical lever design is due to the sensitivity to an angular deflection and how well-resolved and stable the signal from the optical lever is on the detector. As noted, increasing the lever arm improves sensitivity. Improvements are also possible by

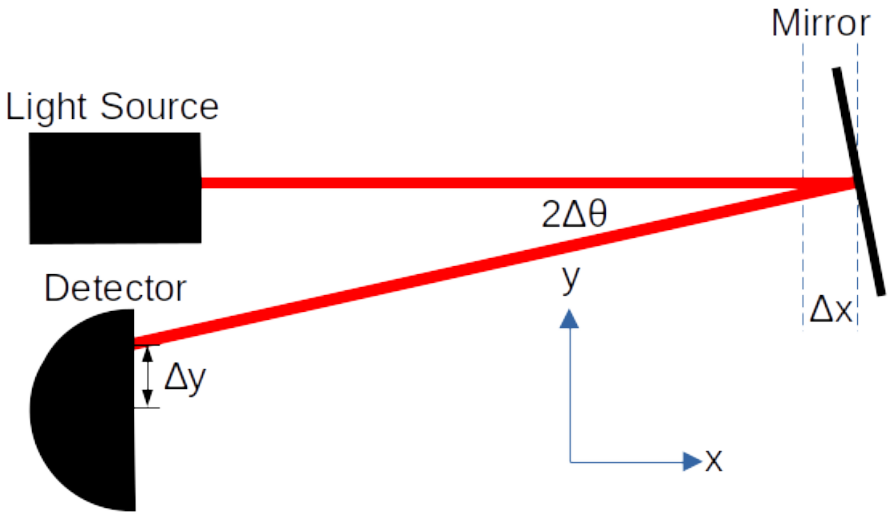

Figure 2.2: Schematic of a simple optical lever. Light from the source is directed towards the main mirror on the right. Then deflected and sensed by a light-sensitive detector on the left.

adding optics that cause multiple bounces off the mirror of interest. Improving the detector resolution can often be done by maximizing the intensity of the light incident on the detector to improve shot noise. The noise could also relate to the stability of the light source. Power fluctuations of incident light on the detector can result in a variation in the uncertainty of each angle measurement.

For many applications, the noise in an optical lever is "white". In other words, the readout noise in angle $\theta_{\text{r.o.}}(\omega) = \Delta\theta_{\text{r.o.}}$ is independent of ω. When we convert torsion-balance angle to torque via Equation 2.3, readout noise shows up at high frequencies as

$$\tau_{\text{r.o.}}(\omega) = \kappa\Delta\theta_{\text{r.o.}}\sqrt{(1-\omega^2/\omega_0^2)^2 + 1/Q_i^2}. \tag{2.7}$$

This equation predicts a general behavior of the torque spectrum $\propto \omega^2$ at the high frequencies where angular readout noise dominates. However, we are interested in the sensitivity down to frequencies as low as 10^{-4} Hz, and there is also distinct low-frequency behavior that usually shows up as $1/\omega$ "pink" angular noise ($\propto \omega$ torque noise). Several effects can cause this. The

main one is sensitivity to temperature fluctuations, which we address by isolating the readout from temperature changes by giving it large thermal mass and shielding and, if that fails, with active feedback. For example, the position sensitive photo-detector (UDT SL3-2) we use in our traditional autocollimator [78] have typical position detection drift of 60 nm K^{-1}.

An interferometric readout is another possible improvement beyond modifications to the simple optical lever. We have developed several interferometric torsion-balance readout schemes in the past [80, 81]. More recently, in collaboration with LIGO, we have also utilized compact homodyne interferometers [82]. The challenges of using interferometers with a torsion balance are their small dynamic range, the need for two mirrors a significant distance apart, and space concerns. We could address the small dynamic range by having an optical lever in addition to an interferometric readout to keep the pendulum within the dynamic range. Also, choosing fibers with low drift can increase the time on the detector. Having two mirrors a significant distance apart is a concern for experiments where we want to minimize gravitational couplings. A clever pendulum design might enable an interferometric readout without sizable gravitational couplings. Fitting all the optics and electronics for an interferometer is also challenging. Homodyne interferometers address many of these concerns; designing pendulums for use with this readout is the main challenge.

2.3 Common Background Noise Sources

2.3.1 Gravity Gradients

The local gravitational field in our laboratory is constantly changing due to the accumulation of groundwater, human activity, and other environmental changes. For instance, the local value of the environmental Q_{21} field (see Appendix B) was measured to be 1.74 g cm^{-3} and varied seasonally by 1% [78]. The changing gravitational field, specifically the field's gradients, can torque the pendulum. These torques can show up as noise and long-term drifts.

The primary noise background at frequencies of interest is the so-called newtonian-noise limit from the seismic field causing density fluctuations [83]. Third-generation gravitational-wave observatories may become sensitive to this phenomenon, but for us this limit is negligible.

There is no way to shield gravitational fields. We minimize the impact of these fields by designing pendulums with negligible gravity gradient couplings. In addition to the pendulum design, we can restrict access to the experimental area and account for the movement of large equipment around the apparatus. We also build gravity gradient compensators to cancel the average gravity gradient signal at a certain point in time. Additionally, there are ongoing developments of an in-situ gravity gradiometer to monitor and consequently correct for the effect of slowly varying gravity gradients.

2.3.2 Seismic Noise

Several factors cause seismic disturbance: anthropogenic activity, microseisms, and earthquakes. How these disturbances impact torsion balances is illustrated in detail by Ritter and Gillies [84]. They can couple directly into the angular readout of the apparatus by inducing relative motion between the pendulum and the detector. Mechanical couplings can torque the pendulum and ring up the resonant mode of the balance.

To improve on this noise source, we use passive seismic isolation. There is ongoing research into an active seismic isolation scheme for our instruments. Additionally, we could work to minimize our angular readout's sensitivity to displacements. Limiting access to the laboratory during a science run could also improve results. Relocating to a remote location could also be beneficial, however, research and development is aided by being located within a research institution with world-class staff and facilities.

2.3.3 Tilt Coupling

If the apparatus tilts, mechanical couplings shift the balance's equilibrium angle. Alternatively, tilt can couple into the readout by changing the pendulum's displacement relative to the detector. These couplings can produce angle shifts as large as 5% of the measured tilt. Many physical phenomenon can cause tilts. For example, temperature gradients can cause an asymmetric thermal expansion of the instrument. High wind speeds can also introduce tilt noise. Anthropogenic activity near the apparatus can impact tilts as well.

Many sources are unavoidable or addressed by mitigating other noise sources by restricting work near the instrument, controlling temperature, passive seismic isolation, etc. Currently, the best way to minimize this is active feedback on the tilt near the suspension point of the balance.

2.3.4 Thermal Effects

Many sensors and mechanical components of torsion balance apparatus are affected by changing ambient temperature and temperature gradients. As noted, these can impact the tilt and the angular readout noise. They can also impact many other auxiliary sensors used to control the apparatus. Tilt sensors, for instance, are temperature sensitive; the Jewel Instruments 755-Series tilt sensors we use are typically biased by temperature changes $\pm$ μrad K^{-1}. So, temperature disturbances can impact the performance of our tilt feedback.

We control the temperature in our laboratory to mitigate the broad impact temperature variation has. Additionally, we enclose all of our experiments in thermal shielding. The experiments' design lessens the impact of thermal gradients with large thermal masses providing inertia against temperature fluctuations.

2.3.5 Magnetic Fields

The effect of magnetic fields can also add background noise that limits the instrument's sensitivity. The main contribution to ambient magnetic fields is the Earth's horizontal field with a measured magnitude of 25 μT. The pendulum is made of non-magnetic material to minize coupling to magnetic fields. However, no materials have zero magnetic susceptibility, so the pendulum can still couple to magnetic fields due to induced magnetic moments from ambient magnetic fields. Hence, a noisy magnetic field environment can produce significant torque noise. Additionally, a constant magnetic field causes eddy current damping of the pendulum, spoiling the Q factor.

If magnetic fields are suspected to be an issue, there are a selection of methods to minimize the effect of magnetic fields. The first is to degauss the pendulum before installation in a controlled environment. Mu-metal shielding further isolates the pendulum from this noise source. Even after degaussing there is often a non-negligible locked-in field from the mu-metal shielding, which would necessitate tuning the measured field out with external Helmholtz coils.

2.3.6 Pressure Changes

An adequate vacuum is necessary to achieve optimal performance. Our experiments have achieved pressures of 10^{-7} to 10^{-6} mbar. Sudden changes in pressure can torque the pendulum. Additionally, high ambient pressure can contribute to gas damping that spoils the Q factor of the balance. This dissertation outlines the first instance of our noise being limited by pressure damping with normal operating pressures.

Trapped volumes can cause pressure spikes within a vacuum chamber. Pressure builds up from natural outgassing until a sudden release of this gas occurs. Removing such trapped volumes can be done by venting the volume. Faulty vacuum seals can also lead to pressure

spikes or elevated pressure levels. Redesigning these can significantly improve performance. Also, replacing defective electronic components that could cause pressure instabilities can be beneficial. A more robust vacuum pump can improve the pressure. It is also essential to clean parts to avoid contamination by materials with poor vacuum qualities.

2.3.7 Electrostatic Effects

Conducting surfaces near the pendulum can contribute to excess noise, particularly if the pendulum is isolated from ground, as is the case with a fused-silica fiber. As the pendulum slowly gains charge, this would introduce slow changes in the equilibrium angle of the pendulum. A charged pendulum could also increase sensitivity due to seismic activity as it causes relative motion between the pendulum and any nearby surfaces.

If this were a problem, we would mitigate it by increasing the distance between the pendulum and nearby conductive surfaces. Any surfaces near the pendulum are gold-coated to ensure optimal surface conductivity, which decreases electrostatic noise. Discharging the pendulum can be done periodically between measurements by touching it with a grounded conducting surface. Conductive coatings have been studied for fused-silica fibers to mitigate this issue for particular use cases [85], but coating always impacts the quality factor of the resultant fiber.

Chapter 3

Fused-Silica Fibers

This chapter overviews the motivation and challenges of manufacturing and utilizing fused-silica fibers in our torsion balance experiments. It outlines basic practical concepts about tuning fiber pulling parameters as well as characterizing and handling fibers. We also introduce some ideas about potential improvements to maximize the performance of fused silica. Further research into these fibers will significantly improve our experiments' sensitivity to new physics.

3.1 Motivation and Challenges of Use

As noted in Equation 2.5 in Chapter 2, the thermal noise for a room temperature experiment can be improved by increasing Q using a low loss material or annealing the fiber. Improvement is also attainable with a smaller κ by changing to a material with a low shear modulus that can hold a large load or using a thinner fiber of the same material. In previous tests, we used a long, thin tungsten fiber [8] (104 cm long, 20 μm thick) with a Q of 6,700 and $\kappa = 2.4$ nJ/rad that held a $\approx$ 70 g pendulum. We produced fused silica fibers with three times smaller κ with Q of 260,000 for our rotating EP test, discussed in Chapter 5, that can hold the same pendulum. Theoretically, this could improve noise by a factor of 10.3 when running at the

same frequency. This recent result demonstrates that fused silica is desirable for the load it can carry for a given κ and its high Q factor.

Fused silica is a phenomenal, readily available material for various applications where low mechanical loss is critical. For example, advanced LIGO, an unprecedented precision experiment, suspends fused silica test masses with fused silica fibers [86]. Q factors of up to 2×10^8 have been measured [87]. Compared to tungsten, with Q ranging from 2000 with no preparation to 7000 after annealing, one would naively expect potential improvements in statistical noise ranging from a factor of 169 to 316. It has been found empirically, however, that the loss in fused silica changes with the diameter of the fiber due to surface loss and also with the frequency of the resonant mode; there is a term in the loss proportional to 1/d (the diameter) [88] or V/S (volume to surface area) [89], and the frequency dependence of loss in bulk empirically scales as $f^{0.77}$.

It turns out that the loss in the fibers described in the proceeding sections is in relatively good agreement with results presented in Reference [88]. Other groups have reported less loss in a similar diameter fiber, so there are likely methods like laser polishing, annealing, and use of the highest purity rod stock that could significantly impact performance. For example, Bilenko *et al.* [90] measured effective machanical loss angles in the pendulum modes of 20 μm fibers that would suggest a Q in excess of 500,000. This suggests that significantly better Q factors are attainable despite the surface loss. Those Q factors would amount to $>$ 14x improvement in Q-related statistical noise over tungsten. However, as will be pointed out in the description of work on the rotating apparatus in Chapter 5, we are already close to being limited by Pressure and readout noise, so utilizing such fibers would require further upgrades to our apparatus or even a complete redesign.

Fused silica is an excellent avenue for attempting to improve our results. There are some drawbacks, however. The one that stopped us from using fused silica in the past was the idea that it would be better to have a conducting fiber to mitigate the potential for charging noise.

As demonstrated in this dissertation, this is not an issue for EP tests where no electrostatic surfaces are close to the pendulum. Unfortunately, for short-range gravity tests, surface patch potentials and relative motion of these surfaces due to seismic disturbance are dominant noise sources. Hence, fused-silica fibers would likely increase statistical noise.

Another primary consideration that makes fused silica challenging to work with is that despite the suitable tensile strength of a newly pulled fiber, the fibers are easy to break. We found that a fiber grazed by any material is rendered useless since it will break under load. We hope to find a surface material that fused silica fibers can touch, as it will significantly simplify the process of getting fibers into an instrument described in Chapter 5. Research into slippery, soft materials with low water absorption may achieve the desired result. Another related property is that exposure to humidity slowly deteriorates the strength of the fibers [91]. So, eventually, we needed to design a storage case in order to keep the fibers in pristine condition. Making the fibers in batches was essential to give more chances to succeed at installation since it is easy to fail repeatedly.

3.2 Manufacturing Process

To manufacture fused silica fibers, we co-opted a model KER52100-E400 HSE KERN CO2 laser cutter at the Center for Experimental Nuclear Physics and Astrophysics (CENPA). Figure 3.1 shows a sketch of the original setup that utilized the integrated rotary stage of the laser cutter. Research into fiber pulling started on the rotary stage puller and produced the fiber used in our dark matter search [92]. Figure 3.1 also shows an upgrade to a precision linear stage, which provides excellent reproducibility and uniformity, producing a much thinner fiber for our rotating apparatus that will allow us to improve sensitivity over our 2012 result [8]. We developed dedicated software for this stage that receives a trigger from the laser control to precisely determine when the laser turns on.

The basic idea is to use a defocused CO2 laser beam spot encompassing the 1 mm rod stock we purchased from National Quartz. The quality of material available from this supplier was sufficient for all the results presented in this dissertation. When we move to higher-purity fibers to achieve better Q factors in the future, results with this rod stock will help tune the parameters to avoid going through as much high-purity material. To achieve a large enough beam spot, we used a laser nozzle with a wide opening of 3 mm and positioned the tip several cm above the rod stock (one recorded height was 2.8 cm). Once the beam was large enough, we did not find significant qualitative differences in the settings needed. When we lost the height adjustment and the nozzle was sitting higher than before, the power would need to be increased slightly, for instance. Because of this weak dependence, we often ignored height as an input to the laser parameters.

Standard metal pin vises are adequate to hold 1 mm thick rod stock as surface fractures of this thicker material did not impact the portion of the rod stock used to pull the fiber. It was common, however, to break material when tightening the pin vises. One side of the holder is stationary, and the other is attached to a linear stage. We used about 10-15% of the total 400 W laser power, P, to melt a portion of the rod stock, and right at the moment a melt is achieved (usually a couple of seconds after laser heating starts) the linear stage accelerates at a_s to some constant velocity v_s, usually on the order of 0.1 m/s^2. In addition, the nozzle moves along the rod stock to melt more and more material until the linear stage stops pulling. How long the process runs only changes the length of the fiber produced. Another input to the process is the distance d_n the nozzle moves. For fixed d_n a change in velocity v_n controls how long the process takes. Then the distance should be adjusted so that $d_n v_s / v_n$ roughly equals the desired fiber length l. Another parameter the new stage allowed access to was the acceleration of the stage a_s, which is important for controlling the pulling process directly after the fused silica melts. See Table 3.1 for examples of tuning fiber pulling parameters. To change the rotary speed, we changed the programmed circumference of the rotary mount in

the software. Putting in the actual circumference value ensures the rotary speed is the same as the nozzle's speed, as expected for engraving. The ratio between the actual and programmed circumference scaled up or down the rotary speed.

The general ideas relating to tuning the parameters that served us well were as follows. The delay should ensure that movement of the fiber puller happens right after melting occurs. The power determines the quantity of material melted throughout the pull, i.e., it should be related to the volume of the resultant fiber. Speed should be adjusted slower if there is evidence that the fiber is tapering or faster if it appears to be getting thicker. With the methods for characterizing fibers in the next section and these concepts, it is relatively easy to iterate on the parameters to achieve a desirable fiber.

A complication we found empirically is that fibers produced as described above are limited in thickness. The thinnest fibers produced were just under 100 μm thick, while the goal was to make fibers ranging from 10-40 μm thick. Thinner fibers would result from using thinner rod stock, but we already had a supply of 1 mm rod stock, and handling thinner stock would be more challenging. So, the solution was to repeat this process twice; first, pull a portion of stock that was much thicker than needed (about a factor 10 thicker than the desired thickness) and then repeat the process of melting that thinner portion of rod stock and pulling a much thinner fiber. In the second stage of pulling, we used 5-15% of the laser power and produced the melt in under a second. We used faster speeds to pull the final fiber.

Another practical part of the manufacturing process that was relatively easy was alignment. The procedure was to find positions where the laser just touched either end of the rod stock and then move the laser to the center of the rod based on that. We often needed further refinement after pulling the first stage of the fiber with the same procedure. Once things were aligned, these parameters could stay fixed permanently. Since the laser cutter is for general use, people sometimes want the fiber puller removed for their work. General use of the laser cutter was a minor inconvenience, and we could resolve that by building a dedicated laser

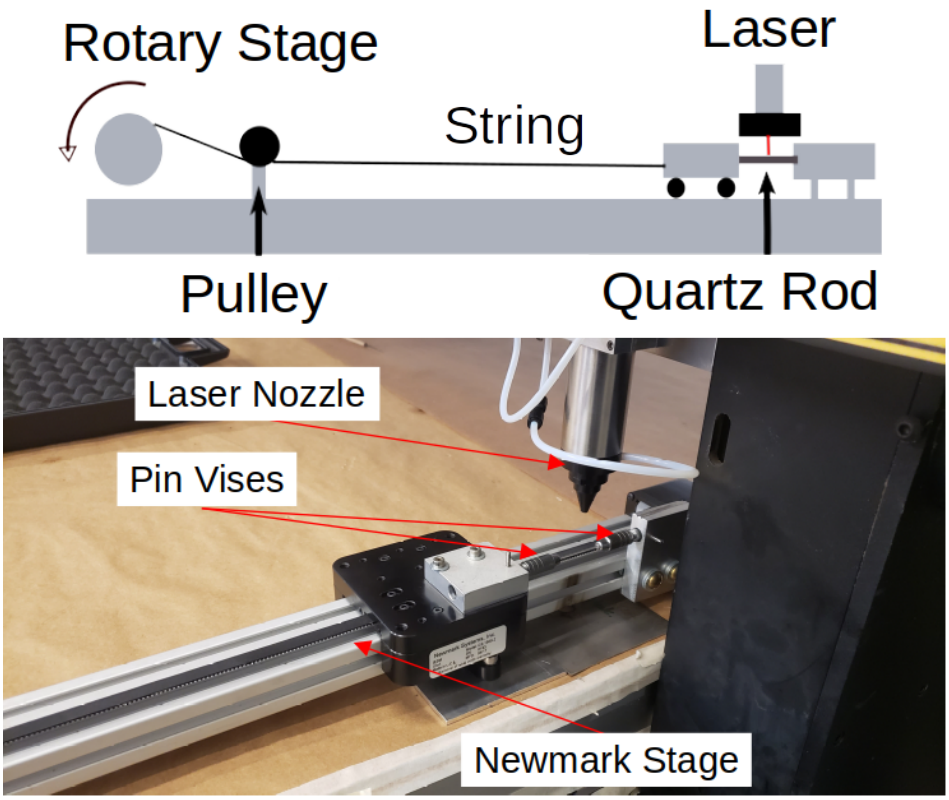

Figure 3.1: Top: drawing of original design of the fiber puller that used the rotary stage that came with the laser cutter. Bottom: image of improved Newmark linear stage.

system for this particular application.

Once we achieve optimal fiber pulling settings, we must attach fibers to fiber screws to install them in an instrument, as shown in Figure 3.2. We attach a set length of rod stock via torr-seal into fiber screws before pulling and adjusting the pin vises to hold them. At first, we tried pulling fibers and attaching fiber screws afterward. However, it was exceedingly challenging to do without breaking the fiber. If the length of the rod stock needs changing after pulling the fiber, attempting to cut the rod shatters the fiber. In any case, ensuring the fiber was ready to be installed directly after pulling is optimal; according to Reference [91], the time to fracture under strain in air can be within a day when an equivalent fiber under the same stress in vacuum can last years.

After much experience with both of the stages used, we have found that the quality of

the stage is essential. With an adequate pulling stage, there is less debugging, less waste of material, and less laser time needed to achieve a usable fiber. We progressed with the rotary stage by stabilizing the moving part with a counterweight to keep the cord going to the rotary stage taut. However, we would not recommend trying to reproduce the results for the fiber in our dark matter test [92] we achieved with the rotary stage. The rotary stage did not reproducibly spool the string it pulled, the track did not fully constrain motion lateral to the pulling direction, and the string itself may have stretched in response to rough parts of the track. These problems may have been possible to address with a redesign. However, we eventually decided that a better use of our time was investigating ready-made solutions. The Newmark CS Series enabled a stage with 1.5 meters of travel to achieve top speeds of 1 m/s with very accurate positioning (3.5 μm resolution), which enabled us to pull a thinner fiber for our rotating equivalence principle test.

Figure 3.2: Fiber screw with broken fiber attached. The rod stock is 1 mm thick and pulled to 250 μm after the first stage of pulling.

pull	P (%)	t_d (s)	d_n (mm)	v_n (mm/s)	v_s (mm/s)
1,1	12	3	6.35	6.35	50
2,1	14	⋯	⋯	⋯	⋯
3,1	⋯	⋯	⋯	5.08	40
4,1	⋯	⋯	⋯	7.62	60
5,1	13	⋯	⋯	⋯	⋯
6,1	12	⋯	⋯	⋯	⋯
7,1	⋯	⋯	⋯	8.38	65
8,1	⋯	⋯	⋯	7.62	60
9,1	⋯	2.7	⋯	⋯	⋯
10,1	⋯	2.6	⋯	⋯	⋯
11,1	⋯	2.5	⋯	⋯	⋯
12,1	⋯	2.4	⋯	⋯	⋯
13,1	⋯	3	⋯	⋯	⋯
14,1	⋯	2.8	⋯	⋯	⋯
15,1	⋯	2.75	⋯	⋯	⋯
16,2	12	0.5	⋯	6.35	1950
17,2	⋯	⋯	⋯	2.54	740
18,2	⋯	⋯	7.62	3.81	⋯
19,2	⋯	⋯	⋯	2.54	660
20,2	⋯	⋯	⋯	⋯	618
21,2	⋯	⋯	8.13	⋯	⋯
22,2	⋯	⋯	10.16	3.302	⋯
23,2	⋯	⋯	⋯	2.54	494

Table 3.1: The pull numbers in the first column are the number and stage of the fiber pull. These are logbook entries when we first adjusted to using the NewMark linear stage. The settings started with work on the first stage of pulling, then moved to the second, and finally produced a fiber with $\kappa = 1.6$ nJ/rad that held well over 100 g. Ellipses indicate settings not changed since last attempt. Usually it was better to tune one parameter at a time. The linear stage acceleration was set to go from rest to v_s in 200 ms for all these.

3.3 Methods of Characterization

3.3.1 Quick Tests to Iterate on the parameters

We developed some tests to quickly characterize fibers and iterate on the parameters used when pulling fibers. It is easy to qualitatively judge the brightness of light scattered from the fused silica with laser protection goggles. The constancy of that light throughout the

pulling process should have some loose relationship to the fiber's thickness; if the light is diminishing during the pulling process, the fiber is tapering off. Ideally, the fused silica reaches peak brightness right before pulling starts. Once pulling begins, it quickly decreases as the diameter tapers off, and it finally reaches a lower constant brightness as the bulk of the fiber is pulling. This ideal was challenging to attain by modifying the pulling parameters by eye. The most challenging part is timing and controlling the start of the pulling process; what happens after the initial melt is hard to control, but within a second, pulling becomes steady. In the second stage of pulling, changing the laser nozzle's height would be appropriate in order to scale down the beam spot to a proportional amount.

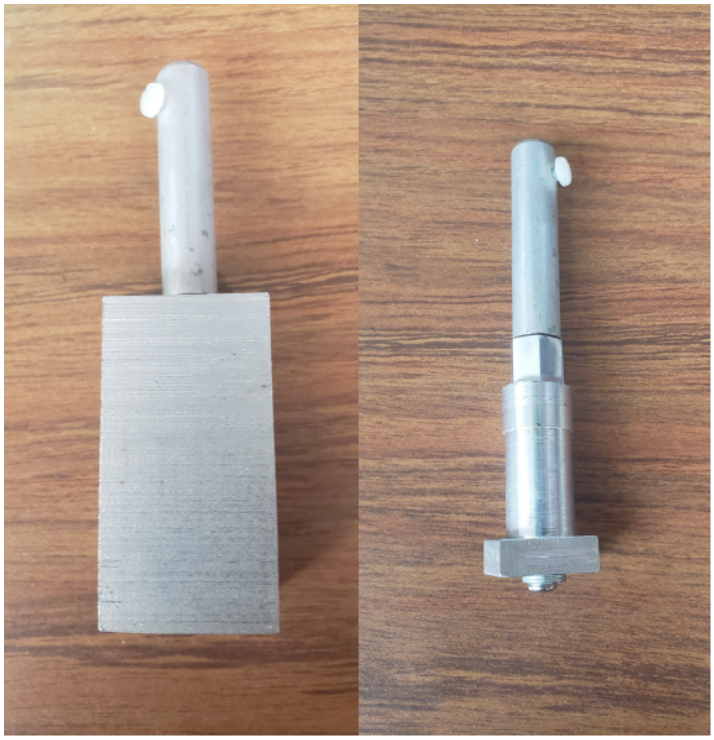

Figure 3.3: Left: fiber attachment to ensure adequate breaking strength. Right: κ testing pendulum. The top cylindrical part clamps on rod stock hanging from the fiber with a set screw.

Once we make a fiber, we must remove it from the fiber puller for testing. To do that, we loosen one pin vise and hold one end of the fiber up and to the side of the stage. Then we

loosen the other pin vise. Once we loosen the other pin vise, we move that fiber carefully away from the fiber puller and then reposition the fiber so that one end is hanging to the side of the laser cutter table. We transport it to testing equipment carefully, watching for any obstructions that might graze the fiber and holding it as far away from our bodies as possible. Once at our testing equipment, we put the fiber in a pin vise held by a jig mounted on the side of a table. Here we can hang the test equipment shown in Figure 3.3 from the fiber.

We first test that it can hold a load suitable for our experiments, so an attachment that weighs 90 g is suspended from the fiber and left for 10-15 minutes. Testing a 90 g load ensures that the EP pendulum is less than 80% of the load the fiber can handle. Once we do that, we use another attachment with a known moment of inertia to assess the κ. After attaching it, we wind the fiber up to a significant amplitude. We use a stopwatch to time the period of oscillations for several periods to get a mean value and uncertainty on the torsion constant. If the result of this test is a very low kappa < 2.4 nJ/rad, then a more detailed fiber profile is made. If not, we are interested in the breaking strength of these fibers and might choose to hang an attachment with a bottle to pipette water into until the fiber breaks. Estimates of the breaking strength are available, so this test is done less frequently now (mainly because shattered fused silica fibers are a slight health hazard). With quick fiber profiling techniques, it makes more sense to gauge the fiber properties before testing to ensure the breaking strength and κ are as expected.

3.3.2 Fiber profiling

Once we obtain settings that produce a quality fiber, we generally move to assess the fiber's diameter profile and the fiber's reproducibility. Then try to improve on the uniformity in more detail. At first, we used an OGP Smartscope Zip Lite video measurement system, which was time-consuming. Eventually, this motivated the development of a fast diffraction method to characterize fibers based conceptually on the Eriometer [93]. Now a fiber can be taken from

the laser cutter to be profiled in a matter of minutes with high precision. Figure 3.4 shows sample data from both methods.

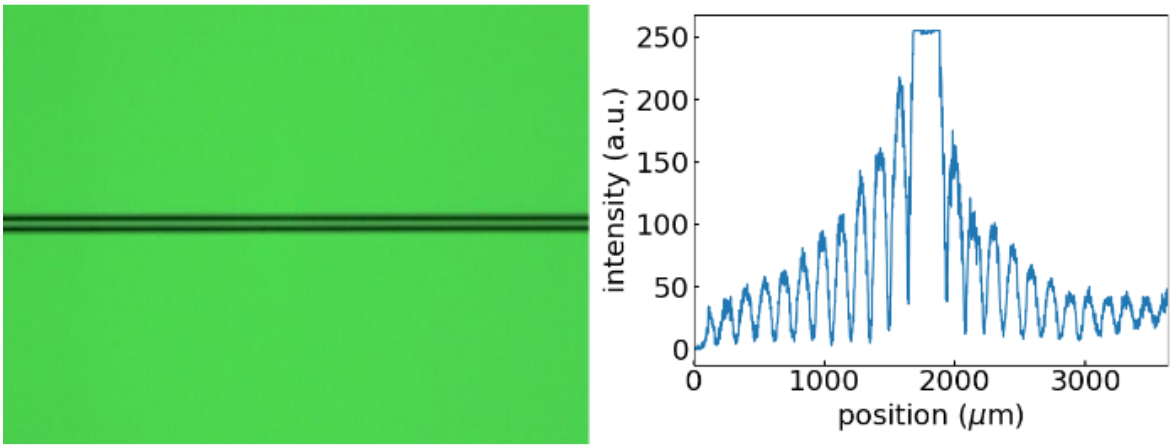

Figure 3.4: Left: Backlit picture of a fused silica fiber on the OGP Smartscope. Right: plot of the intensity of red light due to light diffracted from a fused silica fiber in the Eriometer set up.

To utilize the Smartscope for profiles, we made a stage to hold a fiber mounted beneath the optics. The fiber was backlit with a green light from the Smartscope for the images. The fastest way to use this was to mark positions to slide the mounted stage 250 mm apart (the range of motion of the Smartscope). In each position, we needed to find the positioning for two ends of the fiber and manually program the Smartscope to move between those two ends taking pictures at each 1 mm step. Then we slide the mounted stage and repeat the process until completion. A complete profile took the better part of an hour for each fiber, and repositioning the slide in different positions was challenging to repeat within 1 mm.

Then the images needed to be processed to get a profile. We calibrated the profile for both techniques with tungsten fibers of known diameters from California Fine Wire Company. For each image, we converted the RGB pixels to greyscale. Then we used the darkest pixel to define 0, and the average grayscale value away from the shadow of the fiber was used to normalize the image between 0 and 1 to be processed by the python library `skimage`. It found contours along an arbitrary threshold between shadow and light. These contours were

then fit to lines. The outermost contour lines found were interpreted as the diameter of the fiber using the slopes and intercepts of the lines. From that, we defined a line perpendicular to the average of the two contours crossing the center of the image. Then we found the intercepts with the two contour lines of interest, and the distance between the intercepts gave an estimate of the average diameter for that position.

The Eriometer method used a collimated red (wavelength $\lambda = 660$ nm) laser positioned above the fiber. A Picamera v3 mounted below the fiber with an M10 lens with focal length $f = 9.5$ mm (used for Figure 3.4) turns the diffraction angle into a position measurement on the CCD. The spacing, s, calculated by analysis of background-subtracted data, between the peaks or the troughs is related to the diameter via $d = f\lambda/s$. From the analysis, the central peak seen in Figure 3.4 is unscattered light being focused to a point by the lens. We excluded this peak from the data analysis. For near real-time analysis, we used an FFT method. We took the power spectrum of the two sides. Then a peak finding algorithm found the peak associated with the diffraction pattern and fit the Lorentzian peak to obtain a value for the spatial frequency $1/s$.

To evaluate the performance of each setup, we found it essential to repeat the profiles of fibers. We first tried repeating profiles because we did not believe the fast variations in the diameter our fibers pulled with the rotary stage were real. They were, which motivated the development of an interface to a precision linear stage. Both methods were precise to within 1 μm as is shown in Figure 3.5. The precision was more challenging to assess with the Smartscope because repositioning shifted the profile around. In a segment around 100-200 mm though, the two profiles in Figure 3.5 agree to within 1 μm. Automating the backlit profile would be another possible way to get a quick profile of fibers that performs about as well as the Eriometer method. However, the OGP Smarscope software does not lend itself well to interfacing with a custom translation stage. Perhaps other products like the Smartscope would be adequate for this purpose.

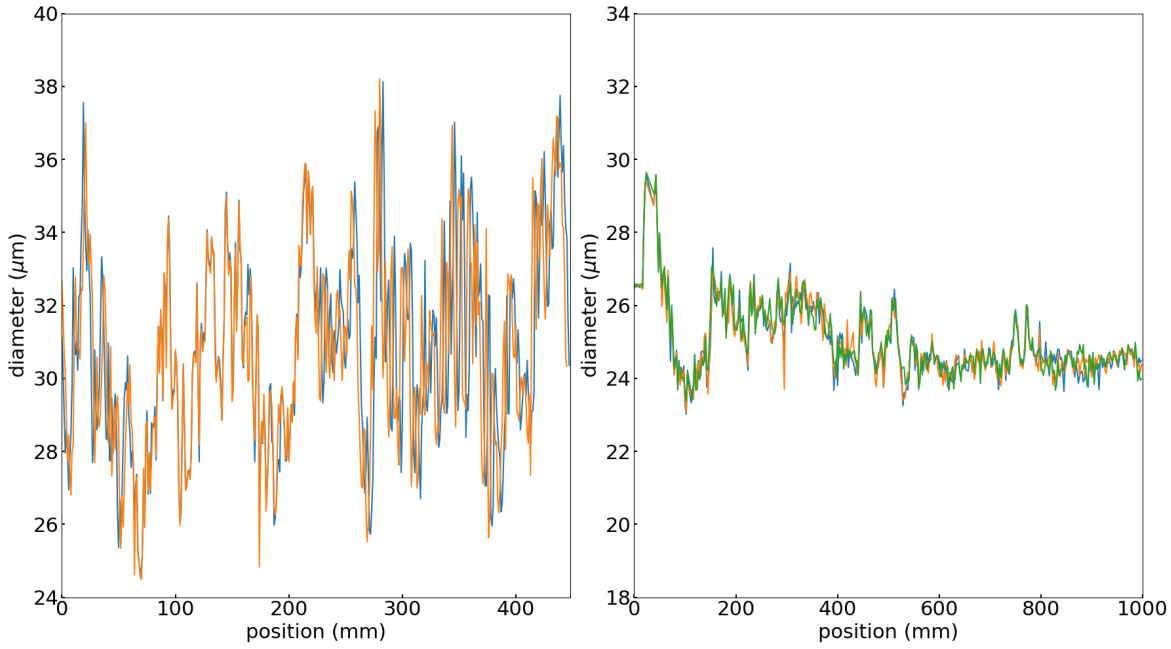

Figure 3.5: Left: repeated Smartscope profiles of the same fiber pulled with the rotary stage. Right: repeated Eriometer profiles of the same fiber pulled with the NewMark stage.

3.3.3 Q Measurements

The fibers are installed in the vacuum chamber of our instrument and attached to a pendulum to measure Q factors. The energy loss per cycle due to the intrinsic Q should be much larger than the energy of other disturbances for this measurement. The energy lost is proportional to the energy stored in the oscillator, i.e., proportional to the amplitude squared. Hence, measuring the change in amplitude over time at as large an amplitude as possible is ideal. No matter how large the amplitude, there will likely be significant disturbances caused by: spikes in the pressure in the vacuum chamber, loss of temperature control, and human activity in the lab. There will always be a scatter in the value of Q, given that energy loss can not be arbitrarily large compared to other disturbances. Addressing this issue requires breaking a given Q measurement into multiple Q measurements and looking at the scatter to find a mean value and uncertainty for the measurement.

To accurately measure the Q of fused silica, the amplitudes necessary are much larger

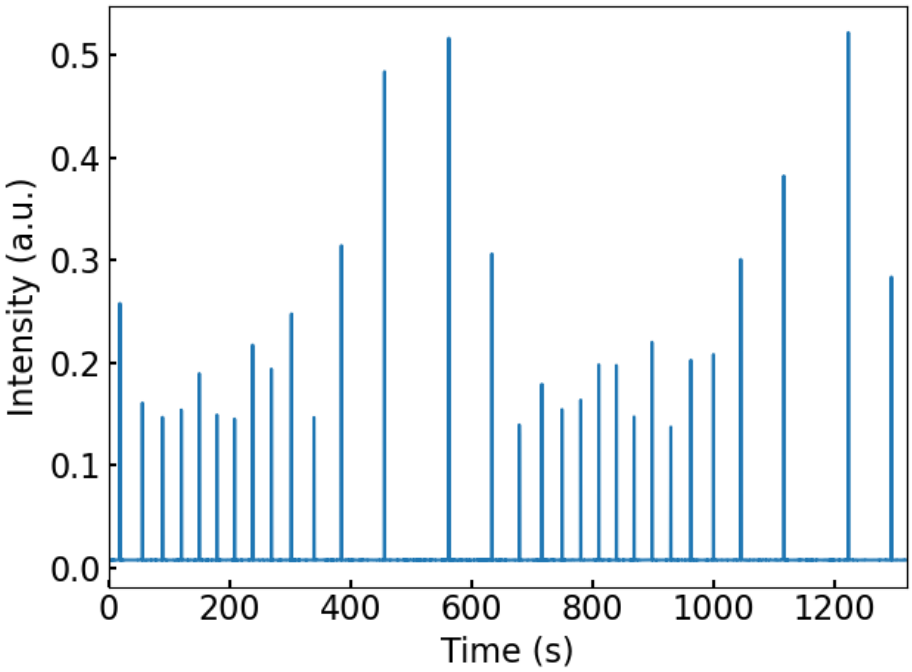

Figure 3.6: Time series of the intensity of light incident on our readout for one resonant period of the pendulum. The pendulum has four mirrors and each time the intensity goes above 0.1 V is one of them passing. This data suggests an amplitude just under two revolutions of the pendulum.

then the dynamic range of the angular readout. For tungsten, an amplitude that stayed on the detector was sufficient, and the ring down could be fit with Equation 2.2. For fused silica, however, data analysis determines when a mirror passes the detector, causes a spike in the intensity of light hitting the CCD, and keeps track of which of the four mirrors of the testing pendulum is crossing and in which direction. Knowing how many mirrors are on the pendulum and their relative positions, we changed the time series of spikes in intensity (shown in Figure 3.6) corresponding to different mirrors reflecting light onto the CCD into data about the times the pendulum was at specific amplitudes. Fitting a trigonometric function to this unevenly spaced time and position data over a period gives a measure of the amplitude. Monitoring this amplitude over long periods, one can produce a figure like Figure 3.7. Fitting an exponential decay $Ae^{-t/\tau}$ to different segments of this amplitude data gives a measure of

Q over time.

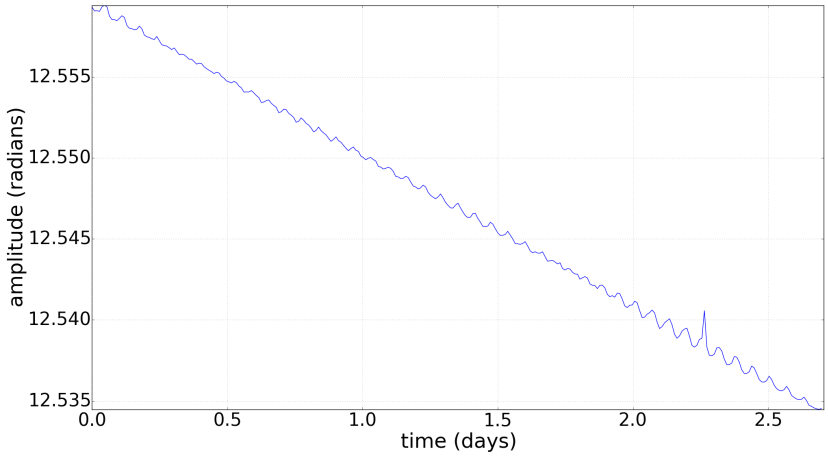

Figure 3.7: The change of amplitude accounts for less than a 0.1 percent change over the course of several days. The prominent oscillations in the amplitude are likely caused by the uncertainty in determining the time at which the pendulum passed the detector. During this run there was a loss of the room temperature control, which caused the spurious spike in amplitude between 2 and 2.5 days.

To get the Q results shown, we found several steps were critical to ensuring that the measured Q is the intrinsic Q of the fiber. When we first measured Q in the apparatus used for the dark matter search, however, the Q was equivalent to that of a tungsten fiber. There were some limiting factors found and solved: we eliminated eddy current damping with improved μ-metal shielding, replaced a low Q seismic-isolation fiber by a torsionally stiff threaded rod to eliminate coupled torsional loss, and pressure loss at the operating pressure of 10^{-7} torr was determined not to be limiting. Considering all of this, our current estimate on the Q of the first fiber in an instrument was $460,000 \pm 10,000$.

3.4 Results

Here we present the fibers we have used for the results of this dissertation and observations about their performance. Figure 3.8 shows profiles of the fibers installed in two of our

instruments. The first shorter and thicker fiber was made with the rotary stage and profiled on the Smartscope. It was measured to have a $\kappa = 5.58$ nJ/rad and Q of 460,000 demonstrated in the last section, which should theoretically improve statistical noise by a factor of 5.4. We used it to constrain ultra-light dark matter in a stationary apparatus [92]. We installed the second fiber in our rotating apparatus.

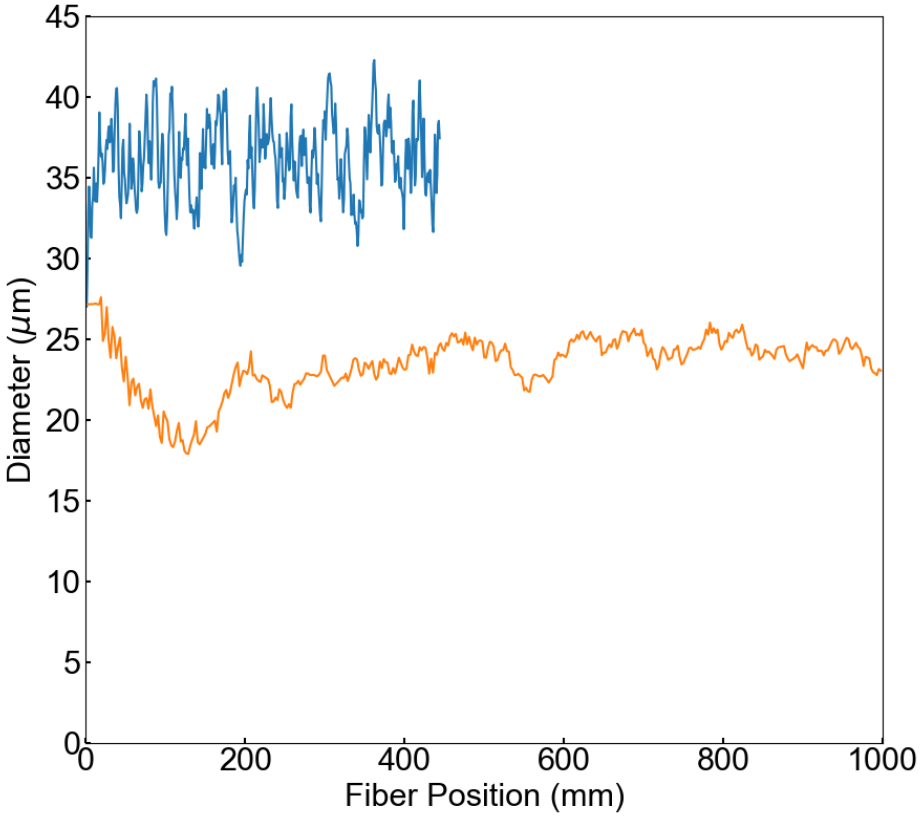

Figure 3.8: **Blue:** Profile of center portion of fiber pulled with the same settings used in our published results [92]. Excludes portion of fiber close to where it tapers down from the 1 mm rod stock used to pull these fibers. **Orange:** Profile of a fiber pulled with the same settings as the one installed in our rotating apparatus. Includes some of the features near the taper. The uniformity of this fiber, pulled with an improved translation stage, is the best we have achieved; in the bulk of the fiber the diameter is constant to within a couple microns.

The first result of note when we started to use fused-silica fibers was a noticeable improvement in the drift of the pendulum shown in Figure 3.9. This low drift was the first indication of a large Q. Often, drifts in fibers are more than expected from thermal noise as

strains within the fiber relax, and due to properties like the thermal expansion coefficient as temperature changes can impact drift. With a thermal expansion coefficient of $\approx 0.6 \times 10^{-6}$/K compared to tungsten of $\approx 4.4 \times 10^{-6}$/K, fused silica is clearly an improvement in thermal properties. We also suspect that the crimping process for tungsten fibers introduces strain that contributes to drift. Producing fused-silica fibers, as described above, does not introduce mechanical strain on the fiber. However, strains are inherent to the pulling process, which motivates the investigation of methods like annealing. These lower drifts may enable the use of more sensitive angular readouts. Many ways to improve sensitivity diminish the dynamic range of a readout, like introducing multiple bounces off the pendulum's mirrors. A more stable fiber makes such methods more practical to implement.

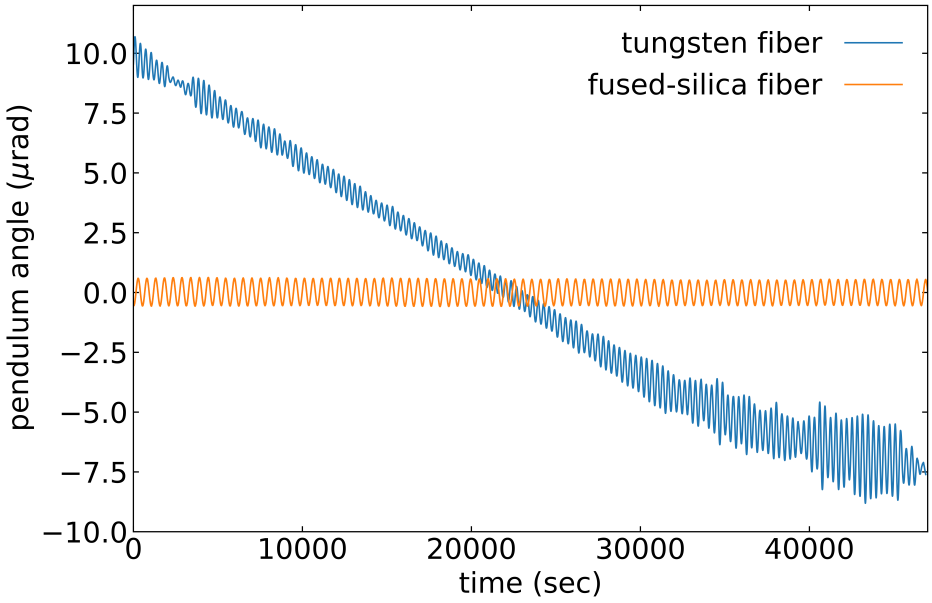

Figure 3.9: Comparison of fused-silica (orange) and tungsten (blue) fibers. The lower drifts in fused silica (< 1 μrad/day) are much smaller than tungsten (> 10 μrad/day). The rapid oscillations are the resonant free oscillations of the torsion oscillator; these are driven by thermal effects and environmental vibrations. The higher Q of fused silica is obvious.

Figure 3.10 shows we can approach the thermal noise limit with both fibers. To produce this plot, we must know many parameters. With a measurement of Q and a nonlinear fit of the resonant frequency f_0 we can predict what the noise floor should look like on a pendulum

with a known moment of inertia via $\kappa = \omega_0^2 I$ and plugging κ and Q into 2.4. This dissertation used the 8-test-body pendulum in the Be-Al configuration with $I = 378$ g cm^2 [78]. We measured the resonant frequencies of the fibers: 1.93 mHz in our dark matter instrument and 0.76 mHz in our rotating equivalence principle instrument. One must also be confident in the calibration of the angular readout. Chapter 4 discusses the angular readout for our dark matter instrument, which nominally has a 14 μrad/pixel conversion from the position on the CCD to angular displacement. We substantiated this nominal value by calibrating the rotation stage of the instrument and measuring a known equilibrium angle shift. In our rotating apparatus, we make a calibrated speed change and analyze the pendulum's amplitude before and after to confirm the nominal readout calibration. Once we determine all the relevant parameters, we produce the thermal noise estimates and convert calibrated angle data to torque with the conversion $|\Lambda(\omega)|/\kappa$ using Equation 2.3.

The noise performance on both fibers shown in Figure 3.10 has been stable for years during nights and weekends, when our experiments get optimal noise. We did the first tests with a turbomolecular pump and were worried about moving to an ion pump that could produce a worse charging environment. However, we observed no noticeable difference. Hence, fused-silica fibers have no drawbacks that can not be overcome and will likely lead to improved results for years to come.

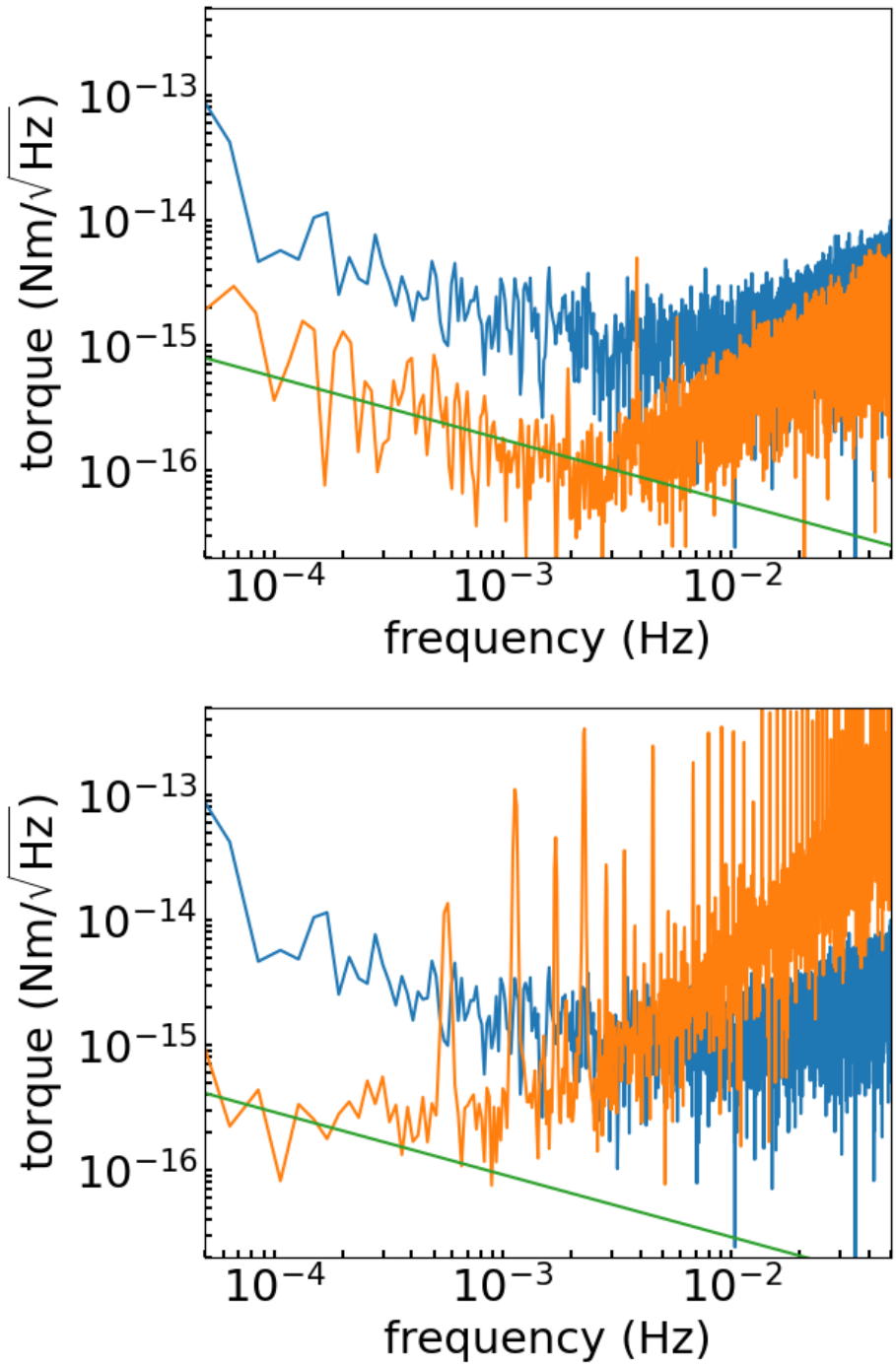

Figure 3.10: Top: Comparison of typical tungsten performance with shorter thicker fiber in stationary apparatus. Bottom: Comparison with tungsten of fiber installed in rotating apparatus. The elevated high frequency noise suggests the performance of this readout has degraded after a decade of use. In both blue is the torque ASD on the same tungsten fiber, orange are the fused-silica fibers, and green is the thermal noise limit. Notice that the bottom orange trace has elevated noise at high frequencies.

Chapter 4

Angular Readout

This chapter covers the development of a multi-slit autocollimator to make it a more functional readout in our torsion-balance experiments. The main challenge was mitigating the nonlinearities of the detector. The prominent pixel-level nonlinearities were more challenging to correct than our traditional autocollimator's detector scale nonlinearities. This concern led to extensive investigation of the analysis technique to develop a cross-correlation method, redesign the slit pattern of the autocollimator, and develop an FFT-accelerated algorithm that enabled further improvements.

4.0.1 Introduction to the Multi-Slit Autocollimator

The multi-slit autocollimator (MSA) described in Reference [79] has been in development for some time but has found limited use as of yet, namely for the results presented in Chapter 7 and beam-rotation sensors installed at the LIGO Hanford and Livingston observatories [94]. This design improves the simple optical lever introduced in Chapter 2. The design shown in Figure 4.1 results in a displacement, ΔX, of the image on the CCD due to an angular deflection of the mirror $\Delta\theta$ of

$$\Delta X \approx 2f\Delta\theta, \tag{4.1}$$

where f is the focal length of the collimating lens. We were inspired to design this by the results of Cowsik *et al.* [95]. They were able to achieve 0.3 nrad/$\sqrt{\text{Hz}}$ noise performance, promising a factor ten improvement on our basic autocollimator design described in many publications as in Reference [78]. For the MSA used in this dissertation, the collimating lens had $f = 500$ mm, hence a mm to mrad calibration between the angle and position of the pattern on the CCD. The camera used was the Mightex TCN-1209-U. The sensor in this camera is a 28.6 mm long Toshiba 1209DG 12-bit linear CCD with 2048 14 μm square pixels. It operated at a rate of 3300 frames/second.

The array of slits consisted of 38 slits that were each 145 μm wide, and the spacing between slits was 145 μm as well; however, what would have been the central 39th peak was left out leaving a gap 435 μm wide. The software first developed to analyze data from the CCD used a Gaussian peak-fitting algorithm with weighted fits to find the position of each peak. Then an average of all the positions was the resultant position of the slit pattern. Doing this for the reference and main patterns and then taking the difference between the two improved results by removing common-mode noise.

When we installed the autocollimator used for this dissertation, we found that the pixel-level nonlinearities were sizeable and more prominent than those seen in Reference [79], ≈ 200 nrad peak to peak. Nonlinearities distort the pure sinusoidal oscillation expected from Equation 2.1. The inconsistency was unclear at the time, but it motivated fruitful investigation into how to mitigate this with the existing hardware. Eventually, after exploring the analysis techniques described below we were able to tune the Gaussian peak-fitting algorithm's parameters to perform in better agreement with Reference [79]. To assess mitigation efforts, we looked at residuals of fits of the resonant peak or at the power spectral density to see the prominence of harmonics of the resonant peak.

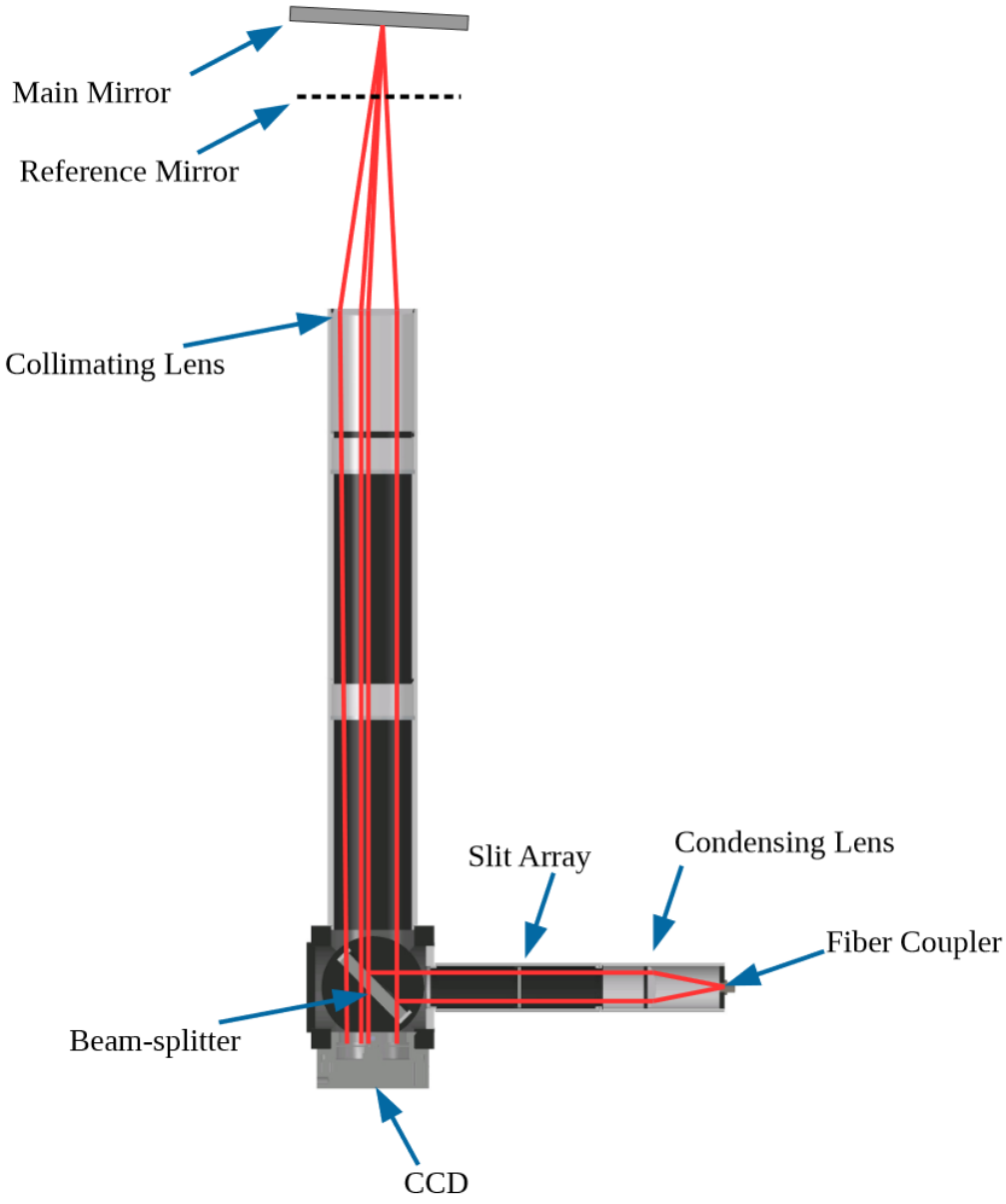

Figure 4.1: Schematic of a MSA. The LED light enters through the fiber coupler, is collimated by the condensing lens, and passes through the slit array creating an image. This image is partially reflected by a beam-splitter, focused onto the main mirror by the collimating lens, and returns through the collimating lens to be imaged on the CCD. A second pattern is made by the partial reflection on the reference mirror and is also imaged on the CCD. Credit: Michael Ross [94].

4.0.2 Cross-Correlation Method

The first idea that produced results was using the cross-correlation between a reference frame and a recently acquired frame to assess the position shift between the two as detailed in Ross [94]. The cross-correlation of two discrete datasets of length N is given by

$$(f \star g)[n] = \sum_{m=0}^{N-1} f[m-n]g[m], \tag{4.2}$$

which, as a function, peaks for the value of n where there is maximal overlap between the two datasets. The analysis calculated the cross-correlation between a window containing one of the peak arrays of the reference frame and a window of another frame at 15 different positions centered on the peak. We fit a quadratic function $f(x) = ax^2 + bx + c$ to the natural logarithm of the cross-correlation values. The resultant fit parameters then estimated the position of the cross-correlation peak ($-b/(2a)$) to find the angular displacement of the pendulum pattern. This is effectively a gaussian fit without the need for a nonlinear least squares fit.

A benefit of this approach is that it was a lot faster than fitting a Gaussian to each peak; a python test code calculated the cross correlation 9.2 times faster. This speedup was particularly important for our beam-rotation sensors to be installed at LIGO [94]. Additionally, it should be better at averaging out a lot of the pixel structure that leads to sizeable nonlinearities. Further refinement led to using two quadratic fits shifted by one pixel to apply a linear correction to reduce the nonlinearity further. As seen in Figure 4.2, this afforded some improvement. At the high amplitudes at which we took this data, spectral leakage from high-frequency harmonics of the resonance causes a slight difference in the apparent noise level of the amplitude spectral density. It is also apparent that the cross-correlation attenuated many high-frequency peaks. Both these observations point to improved nonlinearities.

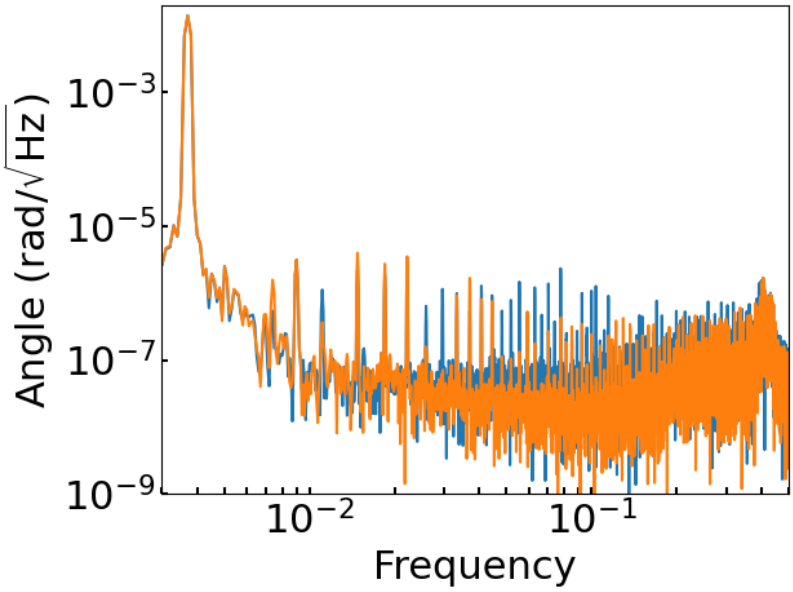

Figure 4.2: Comparison of analyses of a MSA dataset with peak-to-peak amplitude of 35.7 pixels (blue trace Gaussian and orange trace cross-correlation). The cross-correlation technique slightly improves on nonlinearities as evidenced by less power in a number of harmonics of the resonance. The most prominent peak at 3.7 mHz is the resonance.

4.0.3 Uniform Grating and FFT-Accelerated Method

An improvement to the original design and frame analysis software was still necessary for the MSA to find wider use. Chapter 5 describes a gravitational damping scheme that mitigated the effect of nonlinearities with the cross-correlation method. Deploying such a damping scheme would be impractical for general use. Moreover, each time it damped the pendulum, it caused a significant loss of duty cycle as it introduced sizeable shifts in equilibrium angle that ruined daily fits, amounting to loss of a significant number of days of analysis. Undoubtedly, a better way of mitigating these nonlinearities would have been beneficial. Moving forward, we found it essential to continue work to resolve this issue further to improve the functionality of the MSA.

The original slit pattern was unevenly spaced, with minor inconsistencies in the spacing on either side symmetric about the central gap. We redesigned this to have uniform spacing

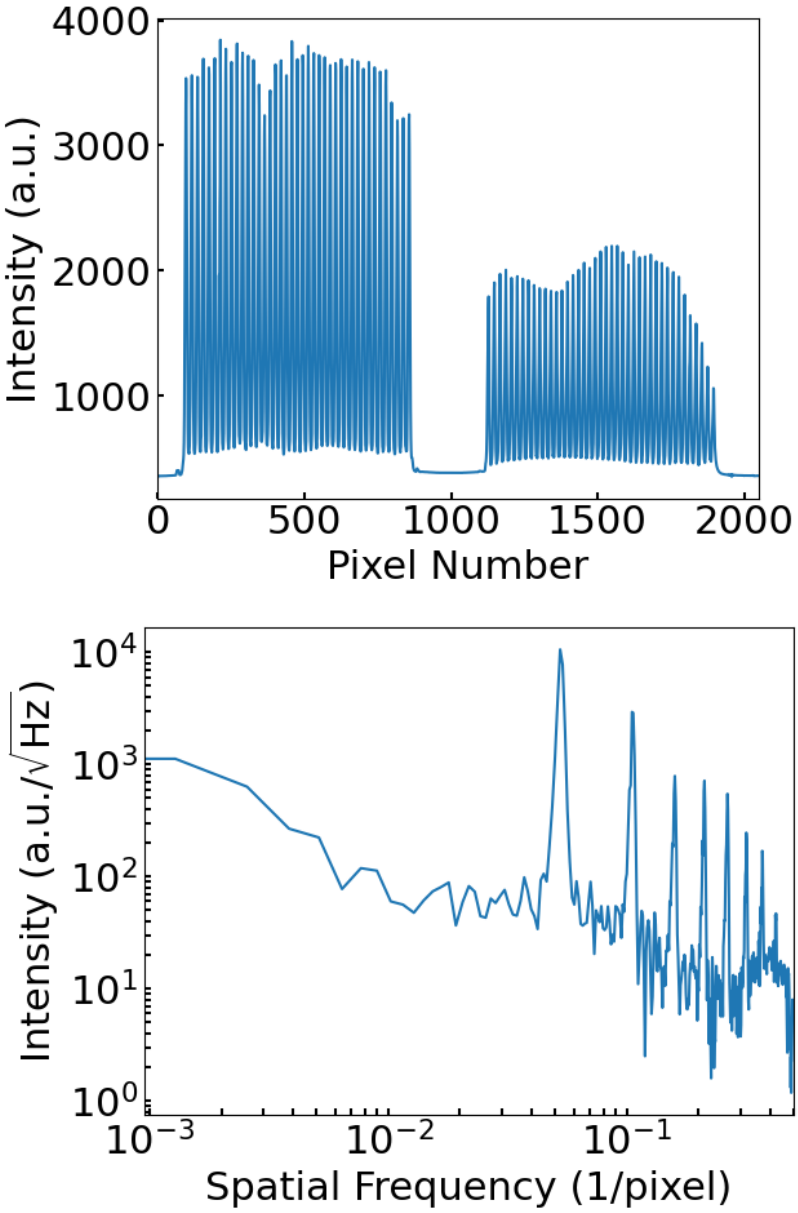

Figure 4.3: Top: example raw frame from the CCD with new slit array. Bottom: amplitude spectral density of main pattern (on the right) with a window of 780 pixels.

across the entire slit array with three additional slits as shown in the CCD frame Figure 4.3. This design enabled the development of an FFT method in addition to the Gaussian and cross-correlation methods. The method involves choosing a fixed window close to an integer number of peaks in width so that one of the bins of an FFT would correspond to the spatial

frequency of the slit pattern. We took that bin's FFT value and calculated the phase, ϕ, of this bin. We then converted this to a shift in position from the start of the window via $-\Delta x\phi/(2\pi)$, where $\Delta x \approx 19$ pixels is the peak spacing. This simple approach ended up being the fastest and least distorted by pixel-level intensity variations. Thus, it allows for faster sampling rates that would improve sensitivity and more manageable nonlinearities.

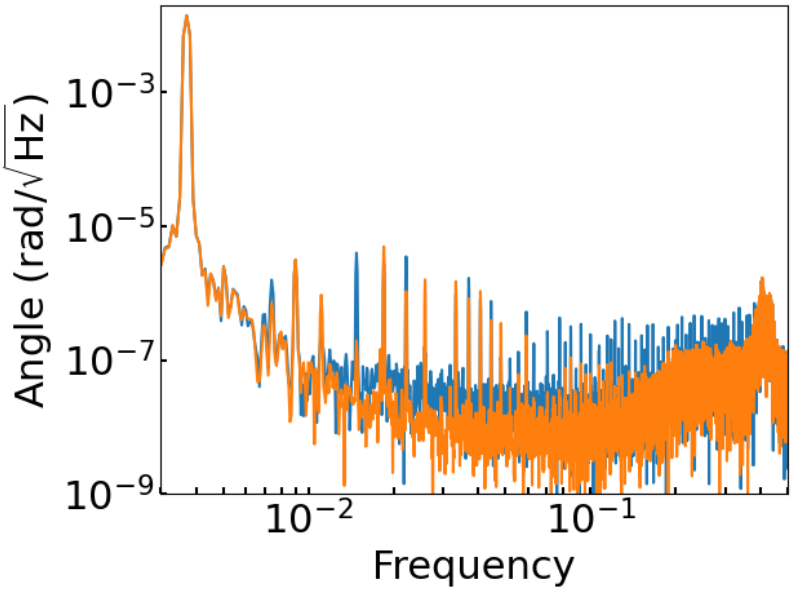

Figure 4.4: Comparison of analyses of a MSA dataset with peak-to-peak amplitude of 35.7 pixels (blue trace cross-correlation and orange trace FFT). The FFT technique minimizes nonlinearities even further as evidenced by fewer harmonics of the resonance. The most prominent peak at 3.7 mHz is the resonance.

Figure 4.4 shows that both analysis methods' resonant peak and low-frequency behavior were consistent. However, there was a marked difference in the high-frequency behavior of the two methods. We believe the improvement is because this method is insensitive to distortion of the peaks in the pattern, as that would primarily change the amplitude of higher spatial frequency harmonics and is less likely to change the phase of any harmonics. Finding the position of either a Gaussian or cross-correlation peak is inherently biased by the pixel-level intensity variations. We attempted to mitigate this for both Gaussian and

cross-correlation methods but were unsuccessful. Reducing the noise in the test apparatus is necessary to fully characterize to what extent the FFT method gets rid of pixel-level nonlinearities. However, there seems to be good evidence that the primary nonlinearity that remains in this method is an apparent change in the peak spacing as the pattern moves across the CCD. These slower changes at a much larger scale than the 14 μm pixels are much easier to correct and this loosens constraints on the amplitude at which the method will require a correction.

Chapter 5

Apparatus

This chapter introduces the two apparatus used in this work. One a stationary i.e. non-rotating apparatus used to search for ultra-light dark matter (ULDM) and the other our flagship equivalence principle (EP) test consisting of an instrument installed on a turntable. We present the novelties relating to the operation of each apparatus and the ongoing development that has taken place on the instruments to obtain results and improve performance.

5.1 Dark Matter Instrument

We searched for the frequency-dependent signatures of B-L and B coupled ULDM using a stationary torsion balance with a pendulum consisting of a Be-Al composition dipole for which $\Delta_{B-L} = 0.0359$ and $\Delta_B = 0.002$. Figure 5.1 shows an overview of this apparatus. We used this apparatus initially as the LISA Test Apparatus (LTA) [96] to investigate noise sources for the proposed LISA gravitational wave detector. Then it was renovated to test fused silica fibers and finally modified to search for ULDM. One feature was an integrated stage that allowed for the easy installation of fused-silica fibers. For the dark matter test, we suspended the pendulum by the shorter, thicker fused-silica fiber shown in Figure 3.8. The pendulum is housed within a vacuum chamber

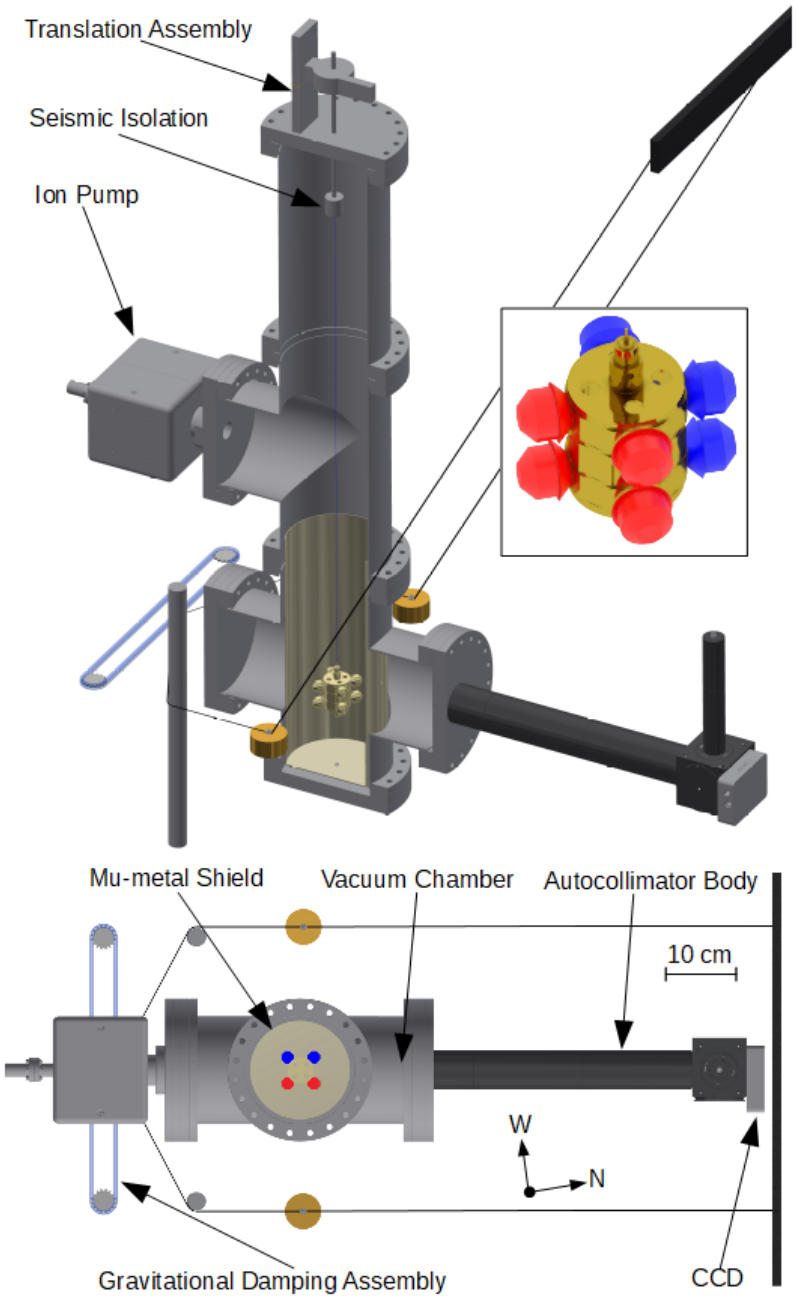

Figure 5.1: Perspective and top views of our apparatus. The insert shows the 8 test-mass pendulum [8] (red and blue indicate the composition dipole of four Be and four Al test masses). A motor-driven roller chain is on the left side. A cord attached to the roller chain moves the two 486 g brass cylinders in opposite directions. On the right is the autocollimator. The N and W vectors indicate the orientation of the instrument and define the lab coordinate system: $\hat{\boldsymbol{x}}$ points North, $\hat{\boldsymbol{y}}$ points West, and $\hat{\boldsymbol{z}}$ is local vertical. Reprinted from Reference [92].

surrounded by a mu-metal shield to achieve the measured $Q = 460,000$. We measured the pendulum angle, θ, using a multi-slit autocollimator [79].

The autocollimator data was analyzed using the cross-correlation method described in Chapter 4. The grating that enabled an FFT approach was not available at the time. As a result, we found it challenging to mitigate the pixel-level nonlinearities. The solution was to keep the angle amplitude within the autocollimator's linear range using a novel gravitational damper consisting of an adjustable mass quadrupole that applied a controlled torque on the pendulum. The performance of the damper is displayed in Figure 5.2. At first, we tested out 1 kg masses to produce the quadrupole field and found that each motor step introduced a 100 nrad shift in the equilibrium angle of the pendulum. We desired a better resolution and moved to 486 g masses. Empirically it was found to change the equilibrium angle 50 nrad per step in agreement with the 1 kg tests. The smaller masses provided ample dynamic range, and improved damping.

The feedback loop acted every second to oppose the average angular velocity, introducing a velocity-damping term to the pendulum dynamics, $D = 5 \times 10^9$ steps/(rad/s). Consider damping with a proportional term instead; to damp down from a 14 μrad amplitude would require 280 steps. It would also shift the equilibrium angle 14 μrad. Using only a D term ideally does not shift the equilibrium angle keeping the stage within its dynamic range longer. However, the D term causes a lot more motion. At a 14 μrad amplitude, the top angular speed is 1.67×10^{-7} rad/s, resulting in 835 steps. We continually monitored the mean angle and amplitude to initiate damping as soon as disturbances drove the amplitude out of the range of control of the D term. We damped the pendulum each time its amplitude exceeded 350 nrad, a peak-to-peak amplitude of 5% of a pixel. This threshold ensured that the maximal number of steps moved each second, ≈ 20 steps, was within the range ± 50 steps that the stage allowed and also kept the effect of pixel-level nonlinearities from impacting the results.

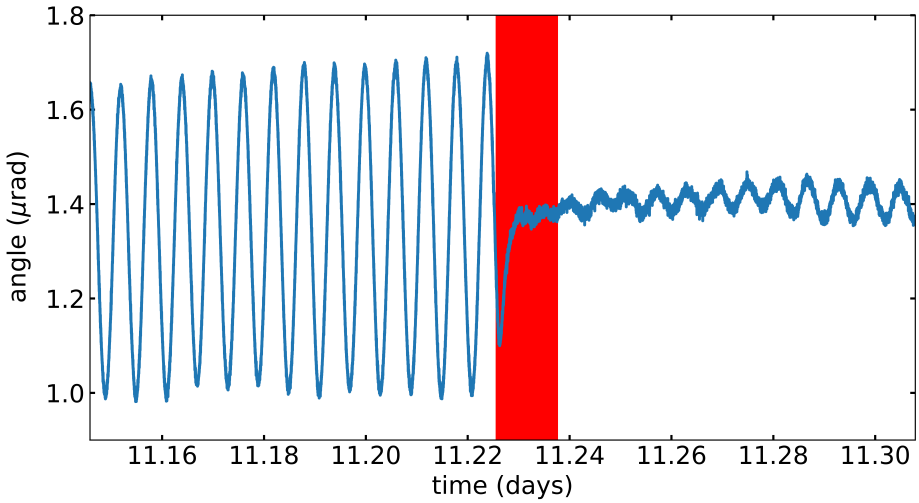

Figure 5.2: Example of gravitational damper performance. The red region is when it is active. Reprinted from Reference [92].

Another complication the multi-slit autocollimator introduced, was that the CCD did not readily accept an external precision clock trigger. Initial testing suggested that lower frame rates would result in a significant loss in sensitivity. Timing is essential to constrain an astrophysical signal. Clocks in most electronics are inadequate for the task. We decided to use a GPS module wired with a long cable to an antenna positioned far outside our laboratory. This GPS-based time measurement allowed for correcting potential drifts in the clock and errors in the assumed sampling rate. Data was taken with this module several months prior, during, and after the science campaign to ensure a long baseline to constrain an average sampling rate to adequate precision. The sampling interval was $\Delta = 1.00212$ s throughout the measurement.

5.2 Rotating Equivalence Principle test

5.2.1 Overview of the instrument

Figure 5.3 shows the main components of our flagship EP test described in more detail in Reference [78]. The main driving component is the precision air-bearing turntable (Professional Instruments Block-Head Model 10BR-AL) that the vacuum chamber is suspended from. This modulates the signal of a potential EP-violating signal interacting with the pendulum while maintaining adequate stability to achieve the thermal noise limit of the torsion balance. Several rotating and fixed thermal and magnetic shields are internal and external to the apparatus to achieve the intrinsic noise limits discussed in Chapter 2. Auxillary sensors measure temperature, tilt, pressure, and positioning. Upgrades and replacements to these sensors are ongoing. We actively control the tilt by a feedback system that uses peltier modules to thermally expand the feet of the turntable. The autocollimator is our traditional design with a laser-diode collimated by a pinhole and a lens that reflects off one of the four pendulum mirrors and is focused on to a lateral position-sensitive detector to measure pendulum twist. Large compensator masses positioned around the instrument reduce laboratory gravity gradients. The entire structure extends about 7 m from the floor.

5.2.2 Modernizing the data acquisition system

A while ago, a crucial component for the apparatus, the DSP (Spectrum Signal Processing AM/D16SA Burr-Brown ADC/DAC), was damaged and it was already a discontinued product at the time. This loss prompted a long process to find an adequate replacement and redesign the entire data acquisition software to accommodate this change. For the most part, this was done temporarily by using a National Instruments DAQ to record data, control motors, and handle the slow (updated every 3 seconds) tilt feedback to keep the instrument

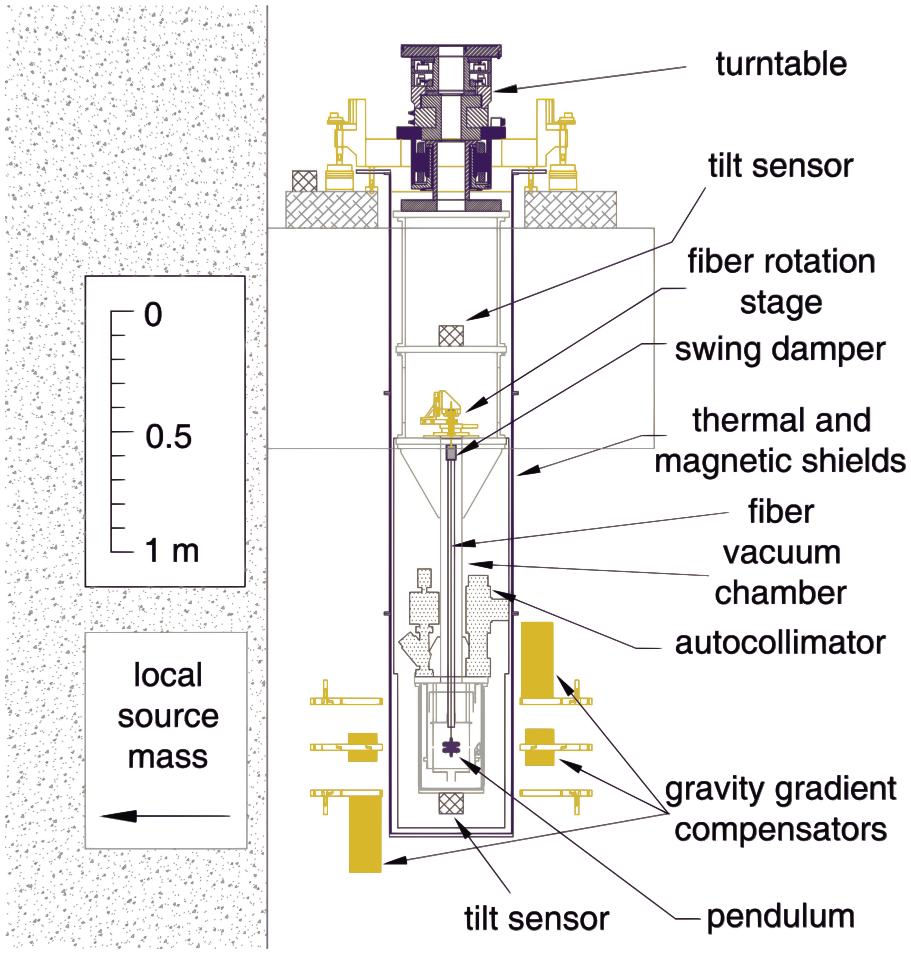

Figure 5.3: Schematic diagram of the rotating apparatus. Regenerated from CAD developed for Reference [78].

level. This new DAQ system prompted a code migration to C#, started by Eric Swanson and continually developed over the years.

Particularly hard to replace was the feedback that drove the turntable. At first, in addition to the DAQ software, we ordered an NI PCIe FPGA module to try. Unfortunately, the calculations needed for the feedback required floating point precision to obtain adequate feedback, and the module did not support that at the time. This deficiency motivated finding another option compatible with the existing NI hardware. We found an inexpensive improvement by developing code for a ChipKit WiFire, a microcontroller with an FPU with an ADC and DAC shield of adequate sensitivity. However, components of this setup became

discontinued, and the performance could have been better when interfacing with the DAQ software over a serial connection. During the pandemic, issues arose with the NI DAQ preventing the system from running stably for the months needed for a science campaign.

After researching available options, we moved to NI's cRIO-9040 controller to handle data acquisition and turntable control. This option was closest to the original design with a DSP. This DAQ system is operational and significantly improves the instrument's performance. Figure 5.4 shows a simple flow diagram. Some key components are still handled in the same EP Test Hardware with C# code adapted to communicate with the new controller. Everything that runs during a science measurement, including the tilt control, can and should be handled by the controller. Hence, we will eventually adapt the tilt feedback to run on the controller.

Figure 5.4: A flow diagram highlighting the main components of the torsion balance's DAQ system. Credit: Conner Gettings.

Notable, this setup has dramatically improved the precision of the turntable control. The state of the turntable in Reference [78] was similar to sample data used in Figure 5.5. This higher precision readout allows a better understanding of the turntable's performance during a science campaign and more robust angle control. To what extent this improved performance is unknown, as this turntable error would have been noticeable as a limiting noise source in the old science data. There was no evidence that it was, which suggests the response of the eddy current motor to this measurement uncertainty allows for better performance than one would naively expect; the response to a turntable error in the pendulum is $1 - \kappa\Lambda(\omega)$ where Λ is the response introduced in Chapter 2, hence at high frequencies you would have expected

to see $\approx \mu\text{rad}/\sqrt{\text{Hz}}$ noise instead of the observed $\approx \text{nrad}/\sqrt{\text{Hz}}$.

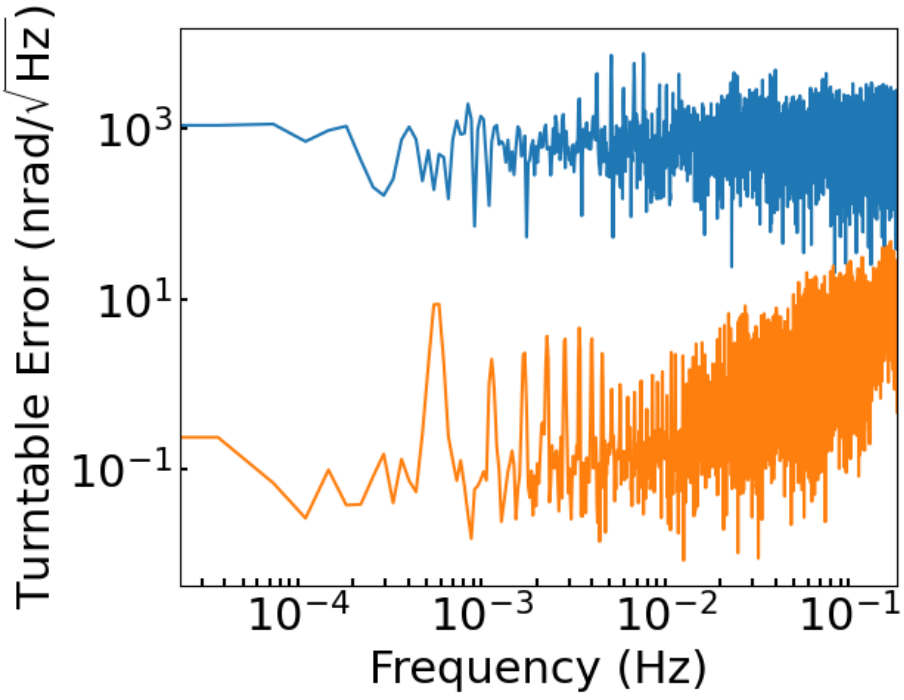

Figure 5.5: Amplitude noise density for the turntable control loop error signal. Blue is data recorded for our 2012 results [8] and orange shows the performance enabled by the cRIO-9040.

Another apparent issue before the upgrade was that the analog hardware lockins for reading out the autocollimator data were malfunctioning. The cRIO-9040 allowed for the implementation of a digital lockin. These old hardware lockins took up a significant portion of the space in our electronics rack. With the extra space, it is much easier to work on existing electronics.

5.2.3 Installing a fused silica fiber

As noted in Chapter 3, fused silica fibers must not touch any surfaces during installation in an apparatus. Unlike the dark matter apparatus, there was no easy method to achieve this. A significant part of the challenge was the fiber shroud, a 2 cm diameter copper tube that extends from below the swing damper to just above where the pendulum sits. The purpose

of this shroud was to heat treat a tungsten fiber to reduce extraneous drifts. It is no longer helpful, but to remove it would have required a new redesign. So, at that time, we proceeded with the need to keep the apparatus aligned to much better than 1 degree of the fiber axis as it translates 1 m up or down to install the fiber. Figure 5.6 shows some parts used to enable the first successful installation of a fused silica fiber in the apparatus.

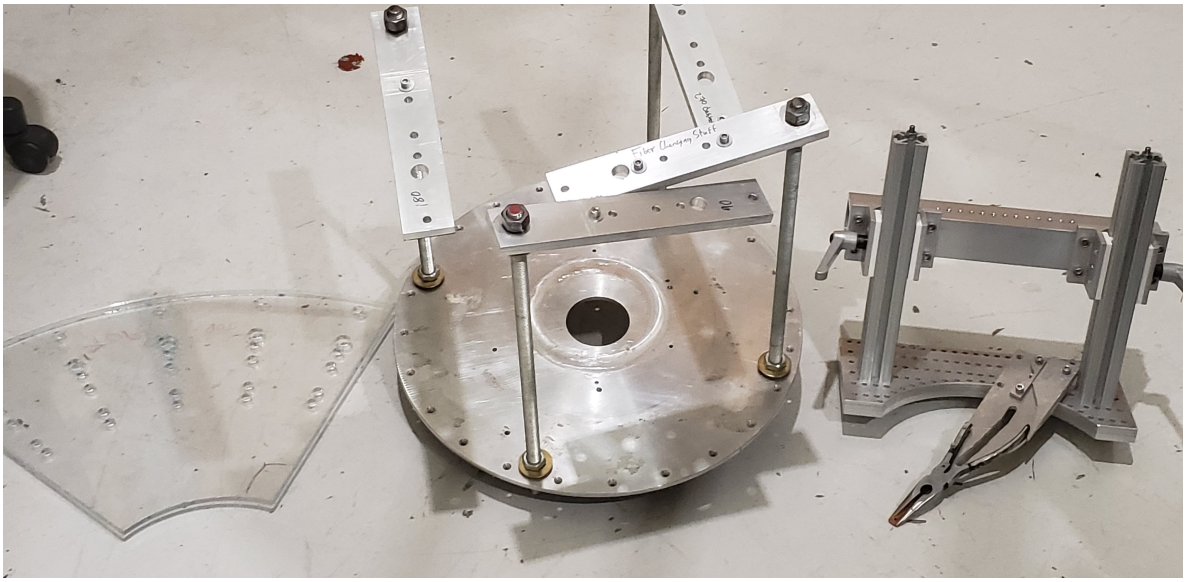

Figure 5.6: Left: CO2 laser cut alignment jigs that mount to the compensator platform to keep apparatus aligned as it is lowered and raised. Middle: platform that extends below the compensators allows for enough travel to install a fiber. Right: jig that mounts to the apparatus to keep fiber aligned with shroud while installing a pendulum.

The procedure was to install the alignment jigs and the platform with a motorcycle jack on top to lower the apparatus the additional amount needed; the compensators can not move a full meter plus the amount required to clear the swing damper, so we needed the jack to allow for extra travel. Once we lowered the jack and compensator, we screwed the fiber into the swing damper. Then we raised everything back up with the compensator, extended the jack, and the top of the apparatus was closed off. We then removed everything obstructing the bottom of the instrument, opened the bottom, and removed the mu-metal shields surrounding the pendulum. We repositioned the compensators for easier access to the bottom of the fiber.

We installed the jig with a fiber screw holder to hold the fiber screw while we installed the pendulum. After installation, we let the pendulum hang freely. If the fiber did not break after 10-15 minutes under load, we had successfully installed a fiber. After that, we could proceed with metrology to ensure the fiber alignment with the rotation axis and the positioning of compensators. Finally, we reinstalled the mu-metal shielding, closed the bottom, and achieved adequate vacuum.

This procedure was laborious and time-consuming, requiring going through several batches of fibers (storage holds up to 6 fibers) to succeed. Nevertheless, since then, the fused silica fiber has not needed to be replaced, so it was well worth the effort. Fused silica fibers stay in pristine condition in an evacuated vacuum chamber for years.

5.2.4 Upgrades to Constrain Systematics

To achieve improved results, particularly towards the Earth, it is also essential to study systematic effects. These can impact noise, hindering the instrument from reaching the thermal noise limit and causing long-term drifts in the turntable signal unrelated to science, as discussed in Chapter 2. We have continually done measurements to assess several systematics and improved the auxiliary sensors on the apparatus, particularly the temperature sensor array (credit Yifei Bai). We have also needed to replace tilt sensors and have worked on the tilt feedback to achieve optimal performance. The one systematic that is particularly challenging to improve on, however, is gravity gradients. Recently, we have made significant progress towards an in-situ gravity gradient measurement scheme (credit Joey Turnbull).

We have made a concerted effort to devise a better gravity gradient measurement scheme for over a decade. One idea was to assess the sensitivity of tilt sensors to gravity gradients. We arranged them outside the apparatus at an equal distance above and below the EP pendulum. These sensors needed to be more sensitive and were plagued by systematics much more significant than any gravitational signal. Matt Turner [81] designed a pendulum

with a remotely actuated motor that moved masses to change the gravity gradient coupling. Designing such a mechanism with one configuration where the pendulum is insensitive to gravity gradients for an EP test would be overly complicated, and further investigation was needed to achieve adequate sensitivity to gravity gradients. We also attempted to develop a scheme using existing translation and rotation stages for our pendulum to mount and unmount a frame with a sizeable inner multipole moment q_{21} that couples to the dominant contribution to the gravity gradient field, the outer multipole moment Q_{21} (see Appendix B about the multipole formalism). This design was roughly similar to the one shown in Figure 5.7 (credit Kassandra Weber). Using the pendulum to lift and rotate a q_{21} frame off static hooks proved complicated logistically. Furthermore, it would have required more travel in existing translation stages. Ultimately, we have settled on installing a linear stage next to the EP pendulum to quickly place the q_{21} frame on the pendulum and remove it.

5.2.5 Achieving optimal noise

A continuing challenge is consistently demonstrating the noise improvements expected from the results in Figure 3.10. One breakthrough we made recently was the realization that with this thinner fiber and a worse vacuum (9×10^{-7} mbar instead of 10^{-7} mbar) than in the dark matter instrument, the statistical noise was being pressure limited. We have identified issues with custom high-voltage electrical connections that caused pressure transients. These transients impacted performance and were easily removed once identified by replacing unnecessary custom high-voltage connections with standard components. We further improved the pressure by adjusting the voltage of the ion pump controller and thoroughly baking the vacuum chamber. The baseline pressure measured at the ion pump can reach 3×10^{-7} mbar after baking (down from 9×10^{-7} mbar). These changes improved the measured quality factor, Q, from around 1.0×10^5 when the fiber was first installed to 2.7×10^5, which decreased the thermal noise by a factor of 1.6.

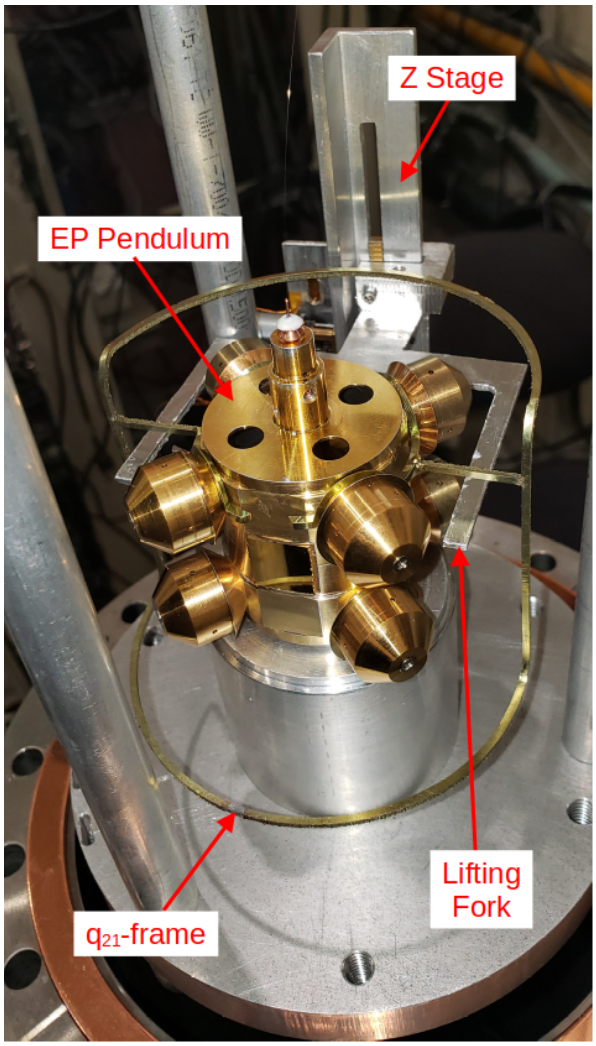

Figure 5.7: Photograph of our test setup to mount a q_{21} frame showing a proof-of-concept for an in-situ measurement of the Q_{21} field.

Large pressure spikes of unknown origin still lead to elevated pressure levels for several hours once or twice daily. We saw this in the previous iteration of the experiment, but now they have more of an impact on the duty cycle of the experiment. Moreover, they likely contribute to the pressure slowly creeping back up to 9×10^{-7} mbar over several months after a bake. This vacuum issue will be pivotal to mitigate for an extensive science campaign. However, we can likely get valuable results within several months once we address other effects that cause instability in the one omega signal.

Chapter 6

Analysis Techniques

This chapter outlines critical analysis procedures that went into the results presented in Chapter 7. We wrote novel code to analyze data from a stationary apparatus to constrain ultra-light dark matter (ULDM) and developed code to constrain ULDM in a rotating apparatus. For the rotating apparatus, there is the possibility of analyzing daily signals towards the Sun and the galaxy's center.

6.1 Stationary Ultra-Light Dark Matter Analysis

6.1.1 Data Quality Measures

The science campaign of the stationary ULDM search consisted of 91.4 days of angle measurements over $S = 114$ days. The data sampling interval, as determined by the GPS module, was $\Delta = 1.00212$ s. The frequency resolution was $1/S = 101.6$ nHz, and we searched in the frequency band from 0.1 mHz to 50 mHz. The conversion from frequency to a dark matter mass from Equation 1.8 is h/c^2, hence we searched for 491,019 different ULDM masses, m_{DM}, between 0.4×10^{-18} and 206.8×10^{-18} eV/c^2 in steps of 4×10^{-22} eV/c^2. For

each assumed frequency, f, we estimated the torque from angle $\theta(t)$, Equation 2.1, as

$$\tau(t) \approx I\ddot{\theta}(t) + \frac{\kappa}{2\pi f Q}\dot{\theta}(t) + \kappa\theta(t). \tag{6.1}$$

We devised the first derivative term to give the exact response for a single-frequency signal. To convert the j^{th} discrete angle sample, θ_j, to a torque sample, τ_j, we used fourth-order numerical derivatives described in Reference [97]. Hence, we estimated the torque as

$$\begin{aligned}\tau_j =& \frac{I}{\Delta^2}\left(-\frac{\theta_{j-2}}{12} + \frac{4\theta_{j-1}}{3} - \frac{5\theta_j}{2} + \frac{4\theta_{j+1}}{3} - \frac{\theta_{j+2}}{12}\right) \\ &+ \frac{\kappa}{2\pi f_{DM} Q\Delta}\left(\frac{\theta_{j-2}}{12} - \frac{2\theta_{j-1}}{3} + \frac{2\theta_{j+1}}{3} - \frac{\theta_{j+2}}{12}\right) \\ &+ \kappa\theta_j.\end{aligned} \tag{6.2}$$

To reduce computation time, we calculated the second-derivative and proportional terms once. The frequency-dependent first derivative term was calculated separately and added in before fitting for a specific frequency. Once the conversion from angle to torque was complete, we found additional preprocessing measures necessary before fitting for signals.

First, we applied a lowpass finite impulse response (FIR) filter [98]. Without a lowpass filter, spectral leakage from high-frequency noise sources significantly impacted fits throughout the analysis band. The prominent high-frequency noise was autocollimator torque noise, as described by Equation 2.7. Microseismic noise is also impacted around 0.1 Hz as well. Hence, we chose the lowpass cutoff frequency to be 80 mHz, and the filter length was 100. The filter was applied forward and backward through the data to null phase shifts and to sharpen the filter response. This procedure ensured a sharp filter that would not bias the results.

Then we divided the torque data into sidereal-day length cuts and removed data points when the gravitational damper was active or during noticeable glitches in the data as shown in

Figure 6.1. We did this glitch removal manually once, as it was exceedingly time-consuming and challenging to program a figure of merit that would exclude all disturbances. A trained artificial intelligence algorithm could potentially be developed that would be adequate.

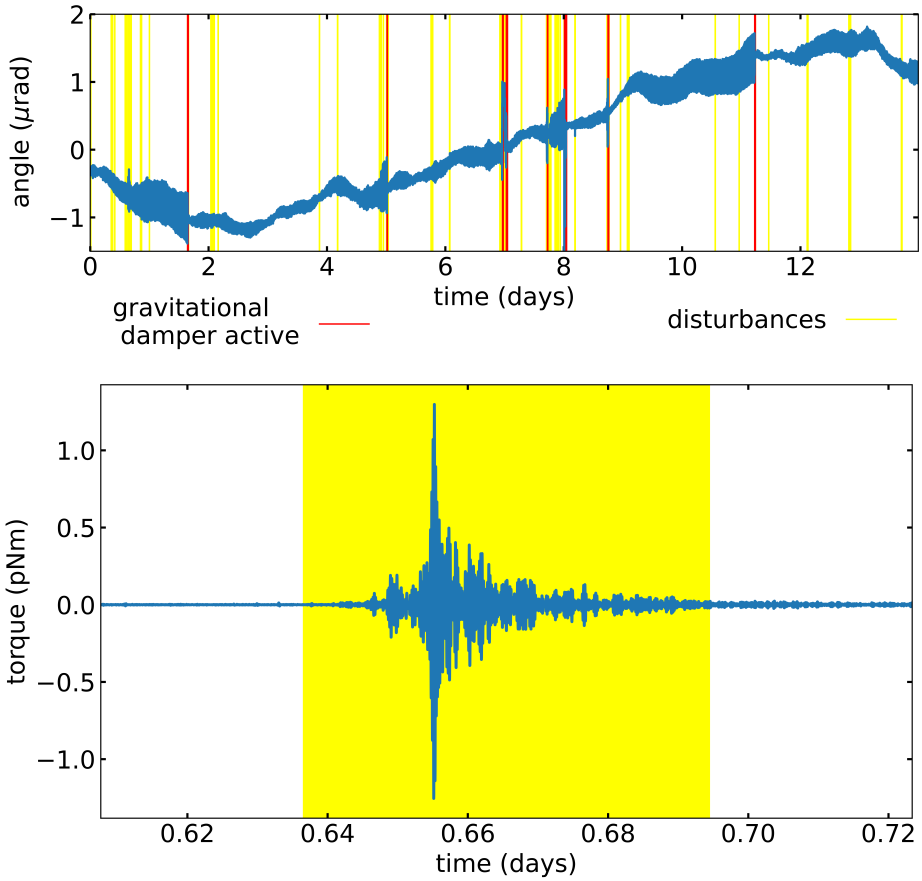

Figure 6.1: **Top:** Two weeks of data. Red bars indicate that the gravitational damper was active, while yellow bars are other disturbances. **Bottom:** Example of an earthquake (on day 1 where there is a noticeable spike in the angle timeseries). Reprinted from Reference [92]

Once we excluded disturbances this way, we determined which cuts to use in the analysis. We adjusted the starting time of each daily cut so that the cuts included more than 90% of the ≈85,982 data points in a day. Damping events introduced shifts in the equilibrium angle we investigated fitting for, but the fitting results were inadequate, motivating exclusion from cuts. These data quality measures, which gave us 40 cuts, ensured good covariance between the basis functions, as evidenced by Figure 6.3. From here, the fitting procedure was similar

to that introduced in our spin-coupled ULDM analysis [68] and summarized below.

6.1.2 Signal Fitting

In our lab, the dark matter torque on our dipole is the analog to the torque on an electric dipole in an electric field. As a reminder, the torque on an electric dipole takes the form $\boldsymbol{\tau} = q\boldsymbol{d} \times \boldsymbol{E}$ where $q\boldsymbol{d}$ is the dipole moment with q or $\Delta q/2$ the magnitude of the charge on either end of the dipole and d the distance between the negative and positive charge distributions. In the ULDM case, the force takes the form of Equation 1.10, and we take $q \to \tilde{q}\tilde{g}_{\mathrm{B-L}}(\hbar c)^{-1/2}$. Hence, for B-L it takes the form $\boldsymbol{\tau}_{\mathrm{DM}} = \Delta q_{tot} g_{\mathrm{B-L}}(\hbar c)^{-1/2}(\boldsymbol{d} \times \tilde{\boldsymbol{E}}_{lab})/2$ where Δq_{tot} is the charge difference on the dipole and $\boldsymbol{d} = 3.77\,(\cos\gamma_d\,\hat{\boldsymbol{x}} - \sin\gamma_d\,\hat{\boldsymbol{y}})$ cm is the vector from one element of the composition dipole to the other. The azimuthal angle $\gamma_d = -80.7 \pm 5$ was determined by measurements of the orientation of the apparatus relative to lab landmarks of known orientation and the orientation of the dipole within the apparatus. Since our instrument is only sensitive to the vertical component of this torque, the torque experienced by the dipole is $\boldsymbol{\tau}_{\mathrm{DM}} \cdot \hat{\boldsymbol{z}}$, which we write as

$$\tau_{\mathrm{DM}} = \frac{m_d g_{\mathrm{B-L}} \Delta_{B-L}}{2u\sqrt{\hbar c}} \boldsymbol{p} \cdot \tilde{\boldsymbol{E}}_{lab}\ . \tag{6.3}$$

Here $m_d = 19.4$ g is the mass of four of our test bodies and $\boldsymbol{p} = \hat{\boldsymbol{z}} \times \boldsymbol{d}$.

We constrained ULDM waves polarized along arbitrary directions in geocentric celestial coordinates $\hat{\boldsymbol{X}}$, $\hat{\boldsymbol{Y}}$, $\hat{\boldsymbol{Z}}$. The definition of this coordinate system is that the origin is the center of the Earth, $\hat{\boldsymbol{X}}$ points towards the sun at the vernal equinox, $\hat{\boldsymbol{Z}}$ points North and passes through the center of the Earth, and $\hat{\boldsymbol{Y}} = \hat{\boldsymbol{Z}} \times \hat{\boldsymbol{X}}$. Slight variations on this come about with the choice of vernal equinox that the definition is based on. The anticipated signals are coherent for $\approx 10^6$ oscillations (see equation (1.8)), which for the highest fitted frequency of 50 mHz corresponds to 231 days, about two times longer than the span of our data.

Following the procedure introduced in Reference [68] we generated 6 science basis functions that evaluated $\hat{\boldsymbol{p}} \cdot \tilde{\boldsymbol{E}}_{\text{lab}}$ for unit-strength fields along the $\hat{\boldsymbol{X}}$, $\hat{\boldsymbol{Y}}$, and $\hat{\boldsymbol{Z}}$ directions. Similar to our previous analysis, we call these daily varying basis functions K_{Xp}, K_{Yp}, and K_{Zp}, which represent transformations from celestial coordinates into lab coordinates. The Compton modulation multiplies each with a cosine and sine phase. Hence, we fit our torque data with

$$\begin{aligned}\tau_j =& K_{\text{Xp}}(t_j)[a_{\text{Xcos}} \cos(\omega_{\text{DM}} t_j) + a_{\text{Xsin}} \sin(\omega_{\text{DM}} t_j)] \\ &+ (\text{similar terms for Y and Z}) \\ &+ (\text{instrumental parameters})\end{aligned} \tag{6.4}$$

where $\omega_{\text{DM}} = m_{\text{DM}} c^2/\hbar$. Note that this expression is perfectly general, as any phase, ϕ, can be determined by this linear combination of sine and cosine amplitudes with, say, $\phi_{\text{X}} = \arctan(a_{\text{Xsin}}/a_{\text{Xcos}})$. We computed the components of $\hat{\boldsymbol{X}}$, $\hat{\boldsymbol{Y}}$, and $\hat{\boldsymbol{Z}}$ parallel to $\hat{\boldsymbol{p}}$ using the `AstroPy` library [99] to find the altitude and azimuth (α and γ) of these unit vectors in the lab frame. For example, the projection of $\hat{\boldsymbol{X}}$ onto $\hat{\boldsymbol{p}}$ is

$$K_{\text{Xp}}(t_j) = -\cos\alpha_{\text{X}}^j \sin\left(\gamma_{\text{X}}^j - \gamma_{\text{d}}\right) . \tag{6.5}$$

Here α_{X}^j and γ_{X}^j are the altitude and azimuth of $\hat{X}$ for the j^{th} measurement. We included six additional instrumental parameters to account for the behavior of the equilibrium angle: 2 for offset and linear drift (a_0 and a_1) and 4 for daily variations with 24 and 12-hour periods (a_{cos24}, a_{sin24}, a_{cos12}, and a_{sin12}). These allowed for daily temperature and tilt variations. The analysis shown in Figure 6.3 shows that for Compton frequencies of interest (greater than ten times the sidereal frequency), there is negligible covariance between the science and instrumental basis functions.

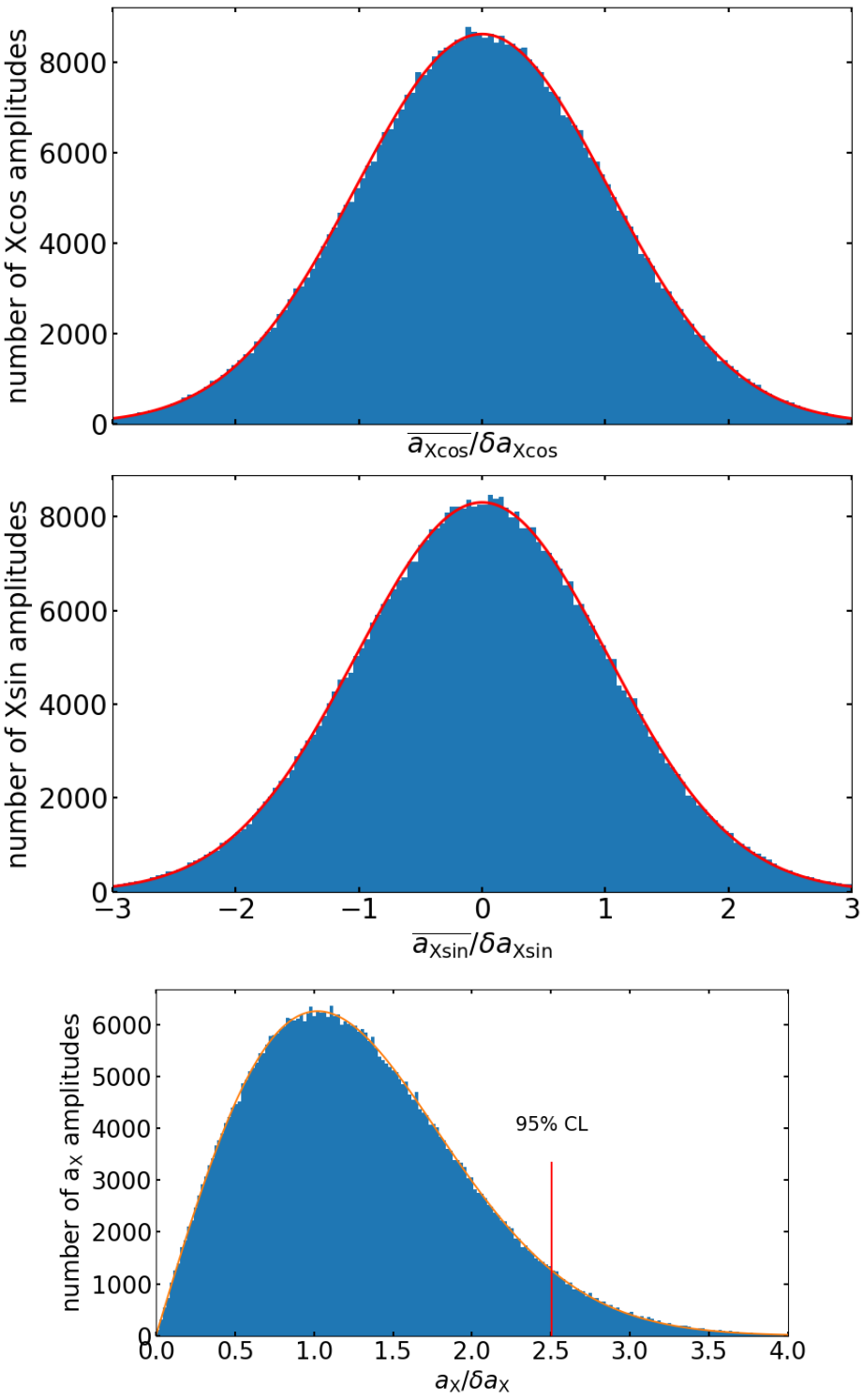

Figure 6.2: **Upper 2 panels**: histograms of $\overline{a_{\mathrm{Xcos}}}/\delta a_{\mathrm{Xcos}}$ and $\overline{a_{\mathrm{Xsin}}}/\delta a_{\mathrm{Xsin}}$ for all assumed masses. Results match zero-mean Gaussians with $\sigma = 1.025(1)$ and $1.022(1)$ (red curves). **Lower panel**: histogram of $a_{\mathrm{X}}/\delta a_{\mathrm{X}}$ values. These match a Rayleigh distribution with scale parameter $\sigma = 1.023(1)$ (shown by red curve). Reprinted from Reference [92]

For every assumed mass, we extracted the science parameters from linear least-squares fits of the 40 cuts. For each parameter, we used the average and standard deviation of the 40 values to constrain the amplitude and uncertainty. This lead to constraints on the fit parameters $a_{\mathrm{Xcos}} = \overline{a_{\mathrm{Xcos}}} \pm \delta a_{\mathrm{Xcos}}$, $a_{\mathrm{Xsin}} = \overline{a_{\mathrm{Xsin}}} \pm \delta a_{\mathrm{Xsin}}$, and equivalent expressions for Y and Z, where the first term is the mean and the second is the standard $\sigma/\sqrt{N}$ uncertainty on the mean. Figure 6.2 shows results for X that are consistent with zero-mean Gaussians with identical widths. The results for Y and Z were very similar. We then marginalized over the uninteresting phases of the $\tilde{\boldsymbol{E}}$ fields. This was done first by combining the quadrature amplitudes to obtain total amplitudes such as $a_{\mathrm{X}} = \sqrt{|\overline{a_{\mathrm{Xcos}}}|^2 + |\overline{a_{\mathrm{Xsin}}}|^2}$ for X. Then we defined total uncertainties to be the average of the quadrature uncertainties $\delta a_{\mathrm{X}} = (\delta a_{\mathrm{Xcos}} + \delta a_{\mathrm{Xsin}})/2$. Equivalent expressions for Y and Z were trivial to obtain. As expected, this marginalization produces results consistent with a Rayleigh distribution. Similarly, Y and Z had scale parameters $1.023(1)$ and $1.021(1)$, respectively.

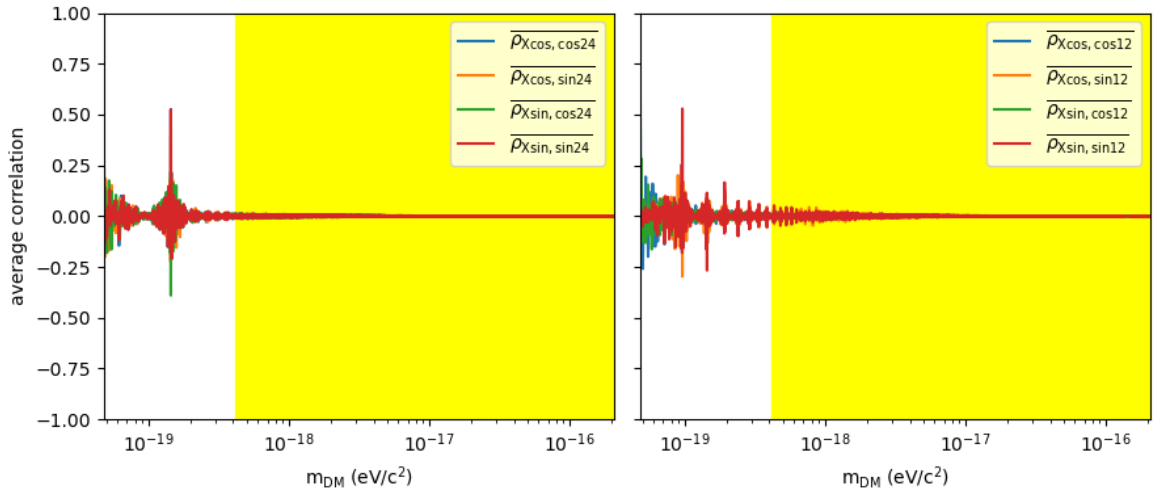

Figure 6.3: Pearson correlation coefficients $\rho_{i,j} = cov(i,j)/(\sigma(i)\sigma(j))$ for the X quadrature basis functions and the 12 hour (Left) and 24 hour (Right) instrumental basis functions summed over all 3,334,034 data points at each mass. The yellow region is the analysis band. The correlation is small enough to get accurate fits (at worse $\pm 5\%$) as evidenced by injection tests (Figure 6.4 and 6.5). Reprinted from Reference [92]

6.1.3 Analysis Systematics

We did various tests to verify our analysis to ensure none of the data quality measures or instrumental parameters introduced biases to the analysis. First, we predicted the angle, θ, in response to a torque signal along $\hat{\boldsymbol{X}}$ and added it to the angle data. Predicting the angle signal was not as simple as using the response function as the signals of interest contain power in the central Compton peak as well as the sidebands from sidereal modulation, hence the amplitude and phase of these components as seen in angle data are slightly different, which motivated calculating the response to each separately with Equation 2.3. The amplitude is scaled up by $|\Lambda(\omega)|/\kappa$ and the phase shift is related to $\arg(\Lambda(\omega))$. This correction to the phase is minimal except for near the resonance. Once the amplitude and phase of each sideband are determined, we combined them to produce the total angle signal. After adding the angle signal to the raw data, we ran the full analysis chain to obtain a resulting fit amplitude. As shown in Figure 6.4, this produced results consistent with the injected torque amplitude across the entire analysis band. The structure of the fits is related to the uncertainty rising at low frequencies due to thermal noise and at high frequencies due to readout noise. The scatter is symmetric about the expected value.

Another test was to look more closely at the response near the resonant frequency of the balance where the frequency-dependent correction outlined in Equation 6.2 is largest. Figure 6.5 shows the response to X, Y, and Z signals. Although X, Y, and Z signals produced peaks in all three amplitudes, the most prominent was always associated with the injected signal. These were consistent with the injected signals of amplitude $g_{\mathrm{B-L}}(\hbar c)^{-1/2} = 10^{-24}$ and demonstrated that the direction of a ULDM signal can be determined. The less prominent peaks are believed to occur because of covariance between sidebands and other sidebands or central peaks, for example, between $K_{\mathrm{Xp}}(t)e^{i\omega_{\mathrm{DM}}t}$ and $K_{\mathrm{Yp}}(t)e^{i(\omega_{\mathrm{DM}}\pm 2\omega_{\oplus})t}$ and $K_{\mathrm{Zp}}(t)e^{i(\omega_{\mathrm{DM}}\pm\omega_{\oplus})t}$ where $\omega_{\oplus} = 7.3\times10^{-5}$ rad/s is the sidereal frequency. Since $K_{\mathrm{Zp}}(t)$ is

approximately constant, the less prominant peak spacing is $\omega_{\oplus}$. Ideally there would be no covariance between signals at different frequencies to make results easier to interpret. We believe that previous results with a rotating torsion balance [68] mitigated this by taking data with multiple orientations of the dipole. Perhaps it is a property of this specific analysis or the data quality measures. In any case, we will investigate this for future stationary experiments.

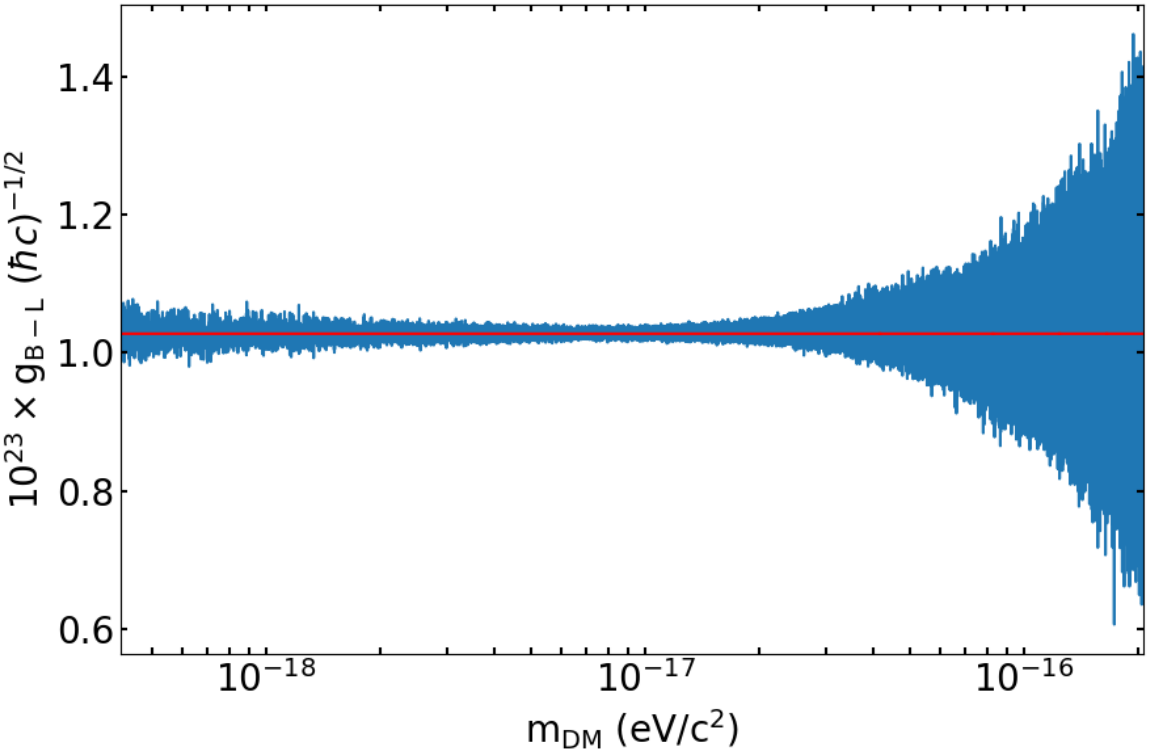

Figure 6.4: X fit amplitudes (blue) resulting from an injected X signal with $g_{\mathrm{B-L}}(\hbar c)^{-1/2} = 10^{-23}$ (red line). Reprinted from Reference [92]

The above tests showed that the analysis did not significantly bias the results for each assumed mass. We then investigated at what point instrumental parameters would affect the quality of science fits. Figure 6.3 shows that the covariance between X quadrature amplitudes and the daily instrumental basis functions is negligible in the analysis band. Results for Y quadrature amplitudes are essentially the same. Z has no sidereal modulation, thus no correlation. We were quite close to this introducing significant errors; large correlations of

25-50% were only about a factor two lower in frequency. Mitigation efforts will be necessary for future measurements if there is the potential to set interesting limits at lower masses.

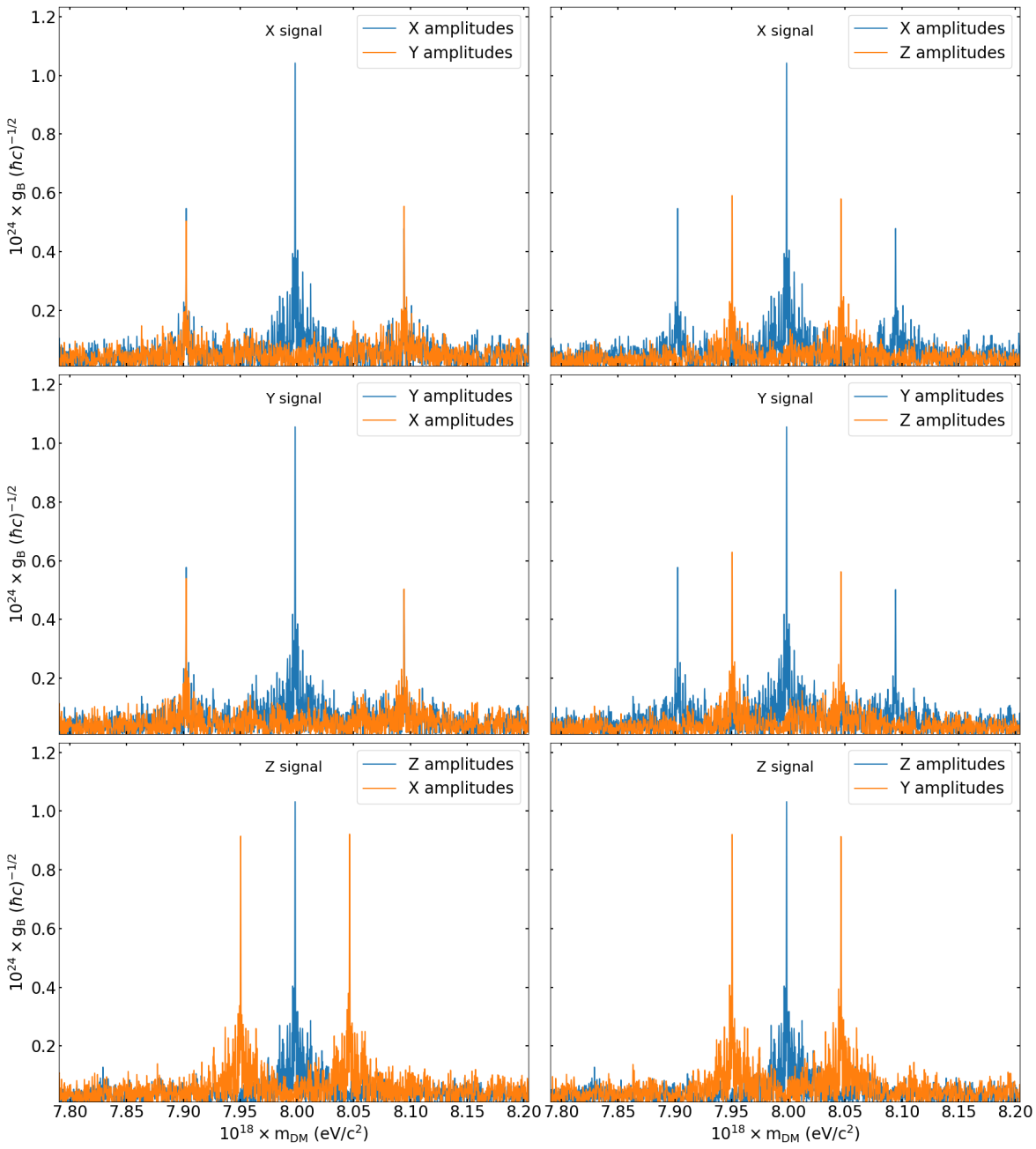

Figure 6.5: a_X, a_Y, and a_Z amplitudes resulting from injected X, Y, and Z signals with $g_{B-L}(\hbar c)^{-1/2} = 10^{-24}$ and mass 8×10^{-18} eV/c^2 (f_{DM} near the resonant frequency 1.934 mHz), where the frequency-dependent correction of Equation 6.2 is largest. Reprinted from Reference [92]

6.2 Rotating Analysis

We developed tools using Python rather than the Fortran code used in Reference [68] to constrain spin-coupled ULDM. Modifications were needed to constrain B-L coupled ULDM, so we moved to a more accessible coding language, Python. Here we summarize the key differences between analyzing a stationary and a rotating balance and the form of fits for B-L coupled ULDM and towards an astrophysical source. The main distinction is that the turntable adds another modulation to the signal of interest in Equation 6.3, so a key part of preprocessing raw angle data before science fits is to develop turntable fits. These are done to obtain quadrature amplitudes, β_{N}^{i} and β_{W}^{i} for the i^{th} cut, of the signal at the turntable frequency ω_{TT}. These quadrature amplitudes correspond to the torque from any potential science signal in two orthogonal directions, N and W. This results in a much smaller data set with samples about every hour instead of every second and a scatter that ideally is limited only by the sensitivity of the torsion balance thermal noise at ω_{TT}. This sensitivity should extend to all frequencies below the Nyquist frequency of the turntable sampling rate as long as there are no long-term shifts in systematic backgrounds.

In the past, prior to turntable fits, our analysis method used what is known as a two-point filter to null the effect of the resonant frequency on turntable fits by allowing the removal of a sinusoid of period T. This filter determines the j^{th} measurement as the average of the datapoints $\theta_{j-T/4}$ and $\theta_{j+T/4}$ as $T/2$ is the time the pendulum takes to go from its minimal to maximal angular displacement. This average leads to the following transfer function that is equal to zero at $\omega = \omega_0$:

$$\Lambda_{2\mathrm{pt}}(\omega) = \cos\left(\frac{\pi\omega}{2\omega_0}\right). \tag{6.6}$$

This method motivated running the turntable where this response is maximal, usually $\omega = 2\omega_0/3$ where $\Lambda_{2\mathrm{pt}}(2\omega_0/3) = 1/2$. We also found a more sophisticated four-point filter with the additional property of nulling the effect of drift. This filter was more useful with tungsten

fibers, where mitigating the effect of drift became important for data quality. After fitting the turntable signal in two-point filtered data, we corrected the results by a factor of two. Then, we used the transfer function of the pendulum to attain the corresponding torque amplitudes.

With the Python analysis, we opted to use the numerical derivatives to calculate the torque introduced in the previous section. The torque data also necessitated the use of a lowpass filter, as in the previous section. There are several advantages to this approach. First, an adequate lowpass filter was generally shorter than $T/2$, so any covariance between neighboring cuts had less impact on results. Additionally, this method has no optimal frequencies to run the turntable at. This property enables the possibility of running the turntable where the torque noise is minimal instead of being limited to running at multiples of $2\omega_0/3$. However, we would still avoid harmonics of the turntable close to the resonant frequency of the balance to avoid driving the resonance. For now, we have kept the turntable running at $2\omega_0/3$, a frequency of ≈ 0.505 mHz, because it was close to the optimal frequency and allowed for comparison of multiple analyses.

The turntable fits included many harmonics of the turntable frequency as imperfections in the turntable readout introduce a forest of lines at harmonics of the turntable frequency. The lowpass cutoff was at 5 mHz, so we only included eight harmonics of the turntable. Each cut length was two rotations of the turntable, 3960 s, so they included three pendulum oscillations. Cuts were not included in a fit if a sizeable pressure transient or the tilt feedback was disturbed by a large seismic event. Figure 6.6 shows the turntable fits from a silica-fiber-test campaign included in the results in Chapter 7. This campaign was before recent modifications to the instrument that have improved data quality and the thermal noise limit of the instrument.

Once we obtained all this information, fits of the form outlined in Reference [68] were done. The Python library `Astropy` was used to generate the transformations from celestial to laboratory coordinates: K^i_{Xp}, K^i_{Xp}, and ones for Y and Z. The geocentric celestial coordinates

of `Astropy` agree with our routines that define equatorial coordinates. Moving to `Astropy` has the benefit of using a standard that other research groups can replicate easily. Another difference is we did not use the correction coefficients $\eta^i = \sin(\omega s^i/2)/(\omega s^i/2)$ where ω is the fit frequency and s^i is the duration of the i^{th} cut. Instead, we used `Astropy` to generate the signal at every recorded time and then put the signal through the same turntable fitting routine, which automatically accounts for any attenuation to the science signal due to the turntable fitting routine. The only other difference in the analyses was the conversion from torque amplitudes to the quantity of interest. With B-L coupled ULDM, there is a direct conversion from torque into the dimensionless values of $g_{\text{B}-\text{L}}(\hbar c)^{-1/2}$ instead of C_e/F_a. This was straightforward to deduce using Equation 6.1, namely the constant $2u/(m_d d\Delta_{\text{B}-\text{L}})/\sqrt{\rho_{\text{DM}}\hbar c}$ resulting in a conversion of $10^{-7} g_{\text{B}-\text{L}}(\hbar c)^{-1/2}$ $(\text{Nm})^{-1}$.

Another benefit of using `Astropy` is that the library has a catalog of astrophysical sources, making it easy to modify this analysis to look for a signal towards, say, the Sun. The transformation of interest is $K^i_{\odot\text{p}}$, which transforms a Sun signal from celestial to laboratory coordinates. And we could correct with $\eta^i = \sin(\omega_\oplus \tau^i/2)/(\omega_\oplus \tau^i/2)$ where $\omega_\oplus$ is the sidereal frequency and τ^i is the duration of the i^{th} cut. For our cut length, the attenuation of a sidereal signal is minute, about 0.3%. But again, instead of accounting for the attenuation this way, we opted to generate the signal from the Sun for every data point and run it through the same turntable fitting routine.

Once β^i_N and β^i_W and all the relevant basis functions were generated, a joint fit of all the North and West amplitudes was done. The simplest to explain is the Sun fit where $K^j_{\odot\text{p}}$ is fit to produce values for $K^i_{\odot\text{N}}$ and $K^i_{\odot\text{W}}$. The basis function is then a concatenation of these two components of the Sun signal, and similarly, β^i_N and β^i_W are concatenated and fit to the joint Sun signal. This ensures that if there is some daily signal, it appears as it should in both channels. The ULDM signal is the same and only has five more joint basis functions. These rotating analyses are preliminary and are mainly to assess the performance. Hence,

rather than a sophisticated estimate of uncertainty, we used the least-squares approximation of the uncertainty. For a fit parameter $\mathrm{var}(\beta_j) \approx \sigma^2 C_{jj}$, where C is the covariance matrix and $\sigma^2 \approx S/(n-m)$ where S is the residual sum of squares and $n-m$ is the length of the data minus the number of fit parameters.

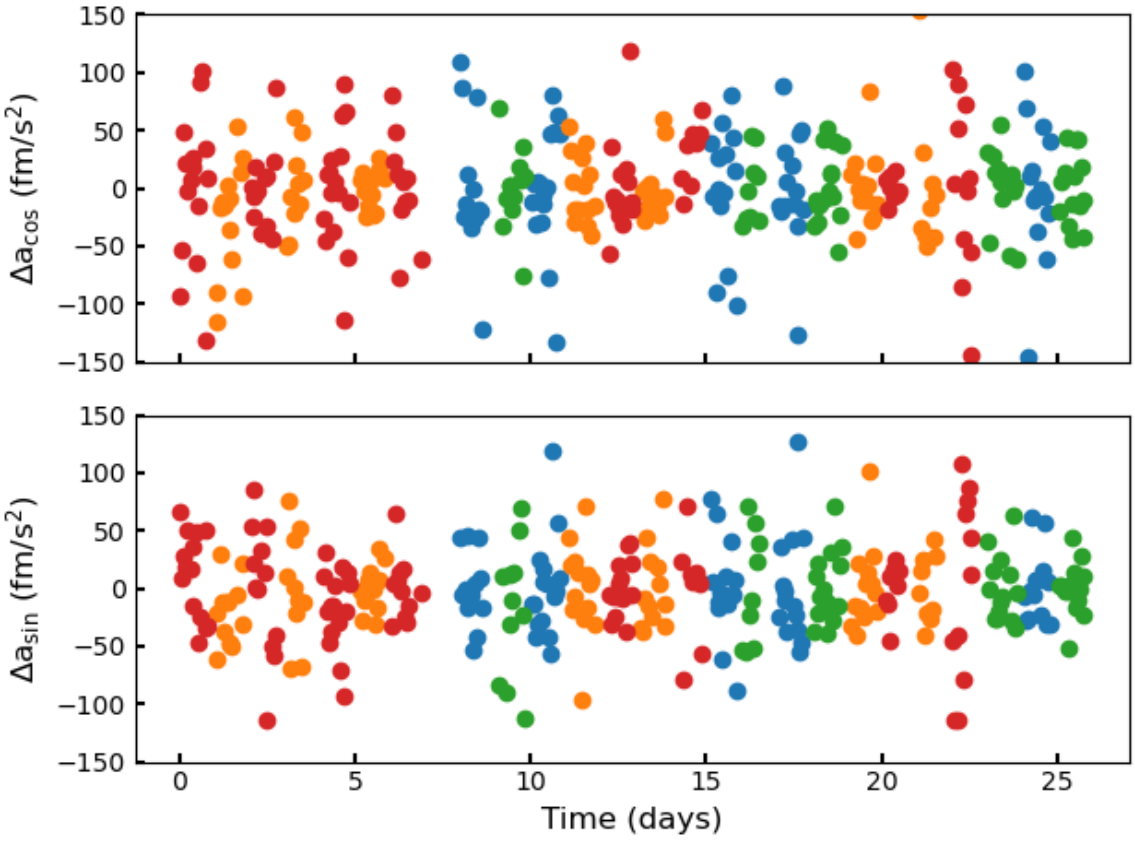

Figure 6.6: Our first rotating apparatus silica-fiber-test campaign. The different colors represent data on different mirrors of the pendulum: blue 0°, orange 90°, green 180°, and red 270°.

Chapter 7

Results

This chapter presents and discusses the results of our ultra-light dark matter (ULDM) constraints. Also, it includes a preliminary assessment of what our rotating apparatus was capable of prior to recent upgrades regarding constraints on ULDM and a signal towards the Sun.

7.1 Ultra-Light Dark Matter Constraints

Figure 7.1 and 7.2 shows our confidence limits on B-L and B coupled ULDM waves propagating along $\hat{X}$, $\hat{Y}$, and $\hat{Z}$ separately. We could also present results for L-coupled ULDM waves. However, since $\Delta_{\mathrm{B}} \ll \Delta_{\mathrm{B-L}}$, our constraints on ULDM coupled to L are practically identical to those shown in Figure 7.1.

The calculation used the Rice distribution [100], which is given by

$$f(x|\nu,\sigma) = \frac{x}{\sigma^2}\exp\left(\frac{-(x^2+\nu^2)}{2\sigma^2}\right) I_0\left(\frac{x\nu}{\sigma^2}\right), \tag{7.1}$$

where σ is the standard deviation, ν is the mean amplitude, and $I_0(z)$ is the modified Bessel function of the first kind with order 0. This distribution describes the amplitudes

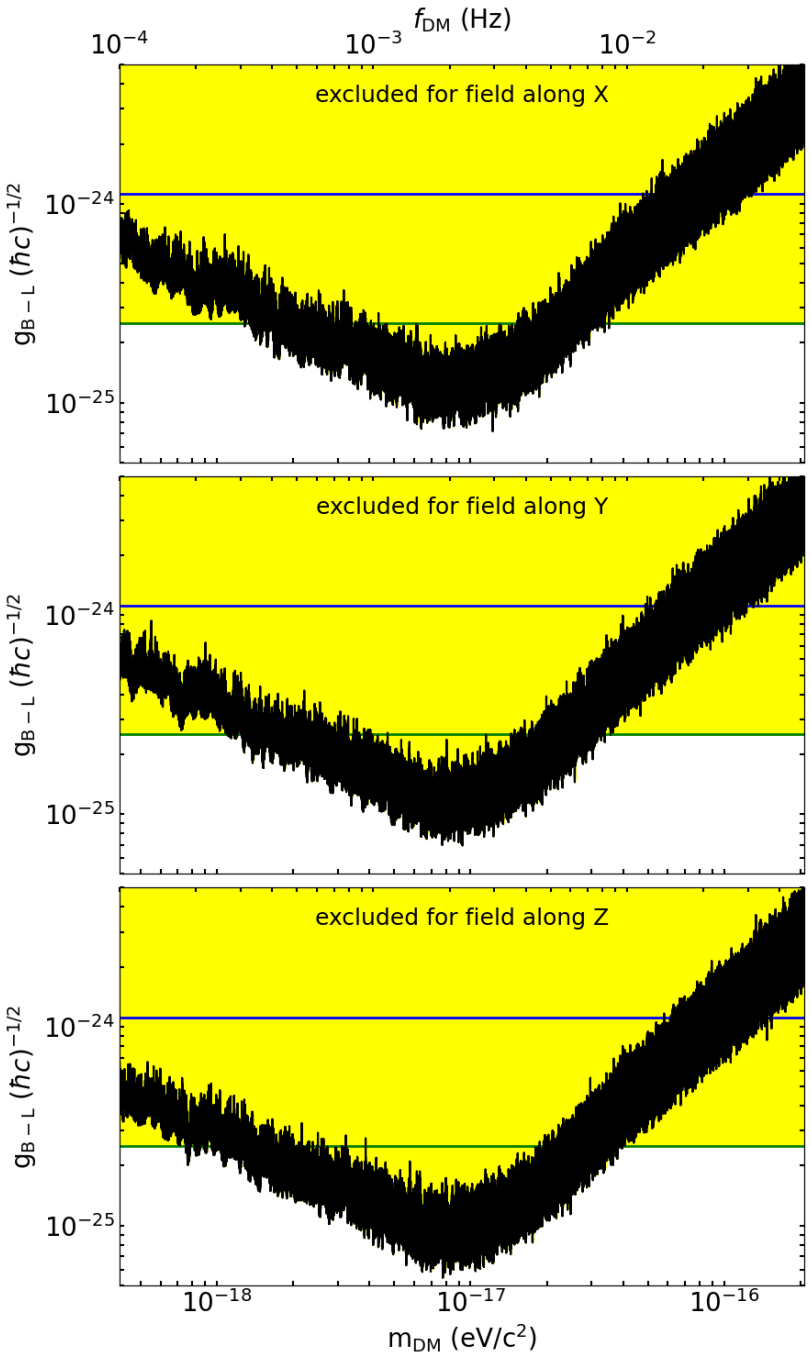

Figure 7.1: 95% confidence upper limits on B-L coupled ULDM. The exclusion regions are indicated in yellow. The black lines, which consist of 491,019 95% confidence upper limits evenly spaced in frequency, show the limits on the amplitudes of fields along X, Y, and Z. The horizontal blue lines are the upper limit from the Eöt-Wash EP test Reference [8]. The green lines are the upper limits from the initial MICROSCOPE result [30, 101]. Reprinted from Reference [92]

of a signal whose quadrature amplitudes in the x-y plane are Gaussian distributed with equal variance. Hence, using this distribution to derive constraints is the generalization of the conventional mean+2σ 95% C.L. upper limit on normally distributed results to Rayleigh distributed total amplitudes appropriate for our signal search. The Rayleigh distribution is retrieved from the Rice distribution when $\nu = 0$. As with other distributions, we can derive what is known as the quantile or percent-point function that for a given value $P \in [0,1]$ as input returns the value x of the random variable for which P is the probability that the random variable is less than x. For the Rice distribution, there is no analytic solution. Hence, we used `SciPy` [102] to evaluate the percent-point function of the Rice distribution for $P = 0.95$.

One thing to note about the results is that below the free resonance of the torsion oscillator, the limits scale as $1/\sqrt{f}$ (behavior characterized, but not limited to internal damping). Above the resonance where the oscillator angle response drops as $1/f^2$, the limits generated from fits of torque scale as f. This scaling is uncharacteristic for white autocollimator noise, which should rise more sharply as f^2. In our analysis band, this is evidence that the autocollimator noise is proportional to $1/f$. Results could improve by addressing this sort of autocollimator noise further. As noted in Chapter 2 this could be done by developing an autocollimator body with more thermal mass, improving thermal shielding, or introducing active temperature feedback on temperature-sensitive components of the autocollimator.

Since the span of our results $S < t_c$, they do not necessarily reflect the long-term average strengths of $\tilde{\boldsymbol{E}}$ because of the stochastic properties of the signal. We would need data with spans longer than the coherence time $S > t_c$ to ensure that we were not taking data during a minimal value of the local field strength. This constraint would require running for a couple of centuries for the lowest assumed mass. There are corrections for this effect for scalar bosons [103, 104, 105] and axions [106]. However, corrections for $\tilde{\boldsymbol{E}}$ of a vector boson are unavailable. Chaotic light is the closest analog, but photons have only two polarization states, while vector ULDM has three. Furthermore, Reference [103] and many

other analyses assume an unrealistic isotropic, isothermal, fully-virialized halo model. This model is oversimplified since recent analyses of Gaia-2 data [107, 108, 109] suggest that 10%-50% of the dark matter in our galaxy is in unequilibrated debris streams from recent mergers with satellite galaxies. So, predicting the actual sensitivity is impossible, which motivates presenting simple experimental results that are easily corrected later.

A viable dark matter candidate cannot consist of ULDM with masses and couplings already excluded by conventional EP tests. These tests provide strong constraints on the couplings of bosons that would mediate long-range forces $m_{\mathrm{DM}} < \hbar c/R_{\oplus} = 3.1 \times 10^{-14}$ eV/c^2 where $R_{\oplus}$ is the radius of the Earth. If the dark matter predominantly consists of B-L coupled ULDM, the constraints set by this dissertation improved on MICROSCOPE's initial EP limits [30, 101] in the mass range between 2×10^{-18} eV/c^2 and 20×10^{-18} eV/c^2 as well as Eöt-Wash EP limits [8] in a slightly wider band. MICROSCOPE has released their final results [31], so the published constraints shown in Figure 7.1 are now outdated. Chapter 8 provides updated plots with an outlook for the future. Conventional EP tests provide strong constraints on the existence of these bosons regardless of whether or not they account for dark matter, so the physics reach of improved EP tests is much more attractive. However, as pointed out by Graham [110], the signal in EP tests is $\propto g^2_{\mathrm{B-L}}$, whereas, in this search, the signal is linear in g_{B-L}. Hence, an N-fold improvement in the sensitivity would require an N^2 improvement in conventional EP results for an equal improvement in constraints. This relationship leads to the observation that once a conventional EP test can be analyzed to produce interesting constraints on a direct ULDM signal, from that time forward, it will always be beneficial to analyze for such a signal.

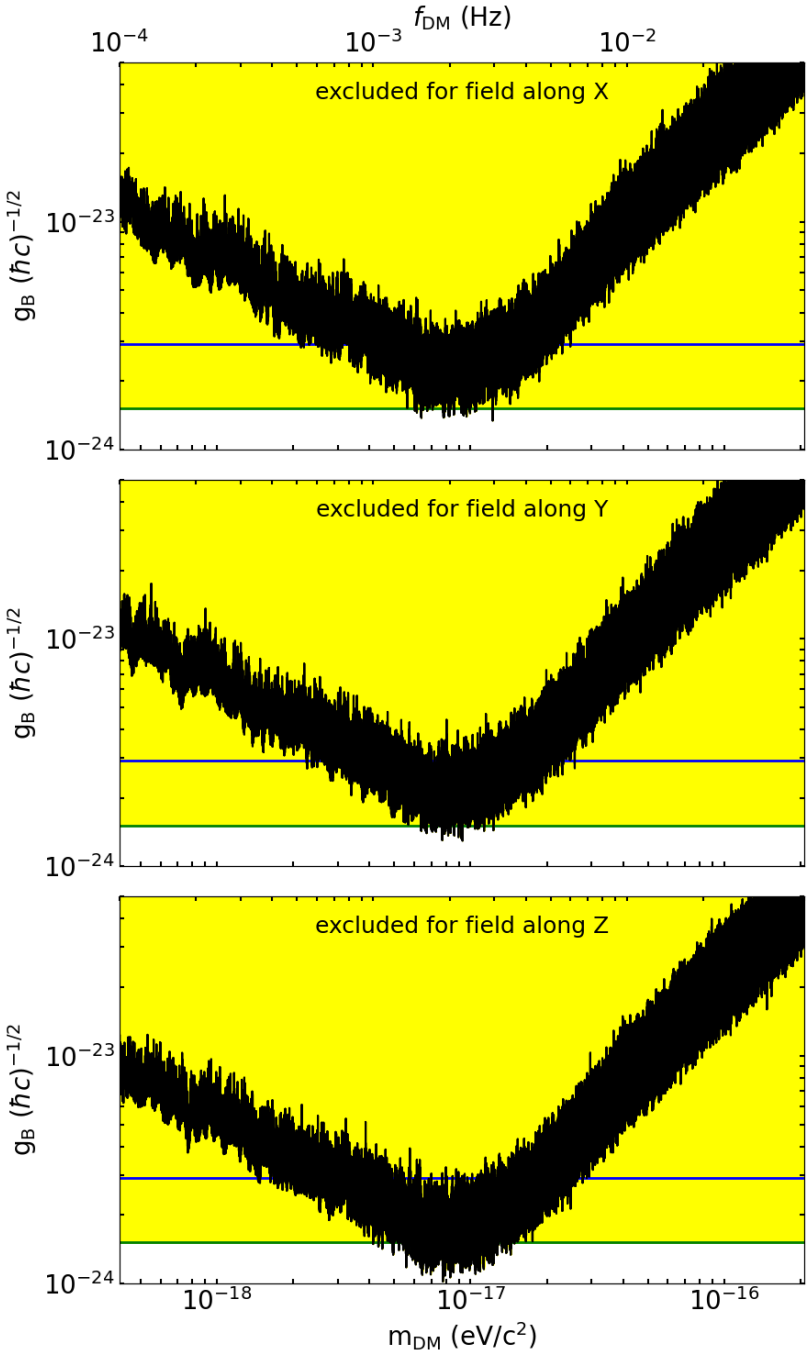

Figure 7.2: Plot equivalent to Figure 7.1 for B coupled ULDM. Reprinted from Reference [92]

7.2 Status of Rotating Apparatus Performance

Figure 7.3 shows the preliminary analysis results outlined in Chapter 6 using the same Rice distribution introduced in the previous section. Notably, it is an improvement on our previous EP results. It was surprising, however, that this initial test did not provide a similar improvement to the stationary results presented in the previous section. This discrepancy may result from the differences between the two analysis techniques. The uncertainty estimate may be overly conservative, for instance. Significant improvements may also be gained with a weighted least squares fit as was discussed in Reference [68]. Some runs in the campaign, particularly over the weekend, had less scatter in β_N^i and β_W^i and there is evidence of the same systematic effect near the sidereal frequency that may be more pronounced with fused silica; the excess noise during the day is likely much higher relative to the thermal noise limit of the fiber.

The performance of fits towards the Sun was evaluated and is simpler at illustrating to what extent we realized the benefit of fused silica. A joint fit of β_N^i and β_W^i yielded $\Delta a_\odot = -0.1 \pm 3.5 \times 10^{-15}$ m/s^2. A similar constraint to what was achieved with Be-Ti and Be-Al dipoles in the past [8] only in under a month. This result is somewhat worse than expected, as a several-month campaign would only slightly improve on results with tungsten fibers. Weighting the least squares fit may significantly improve results, as in the ULDM analysis. With recent modifications to the apparatus, we may start to see more substantive improvements from fused silica and not just from preselected spectra from finite segments of recorded data but from a more extensive analysis of a similar run over a month.

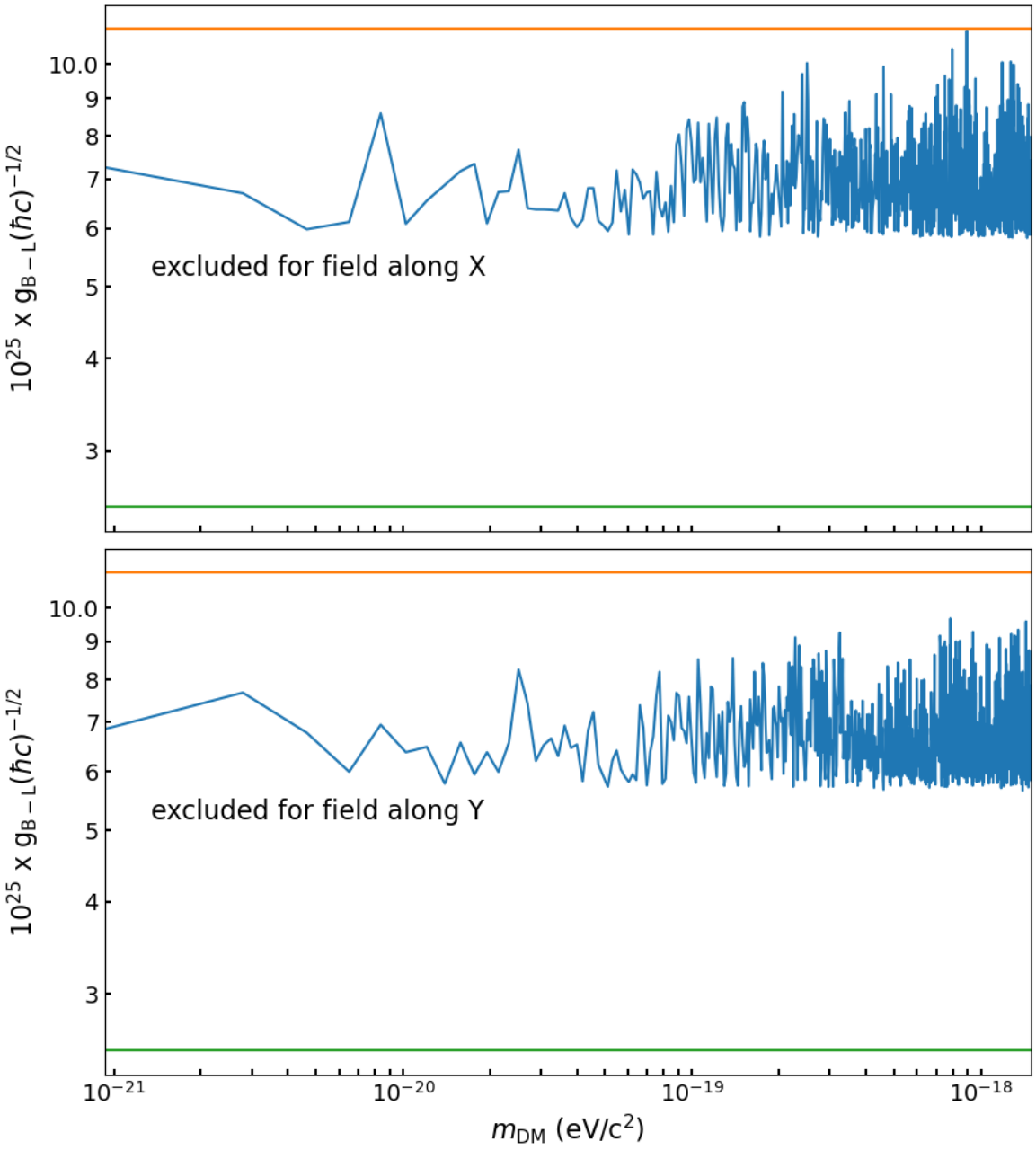

Figure 7.3: Blue trace is the 95% confidence upper limits on B-L coupled ULDM from our fused-silica-test campaign. Orange trace is our EP test [8]. Green trace is MICROSCOPE's initial results [30, 101].

Chapter 8

Recommended Next Steps

This dissertation introduced the theoretical motivation for the continued development of non-rotating and rotating torsion-balance experiments constraining the equivalence principle and ultra-light dark mater (ULDM), the main limiting statistical and systematic noise sources, and breakthroughs in the use of fused silica fibers and the results this has enabled. Going forward, we have several science campaigns in mind that the increased sensitivity of fused silica motivates: a rotating EP test with a hydrogen-bearing pendulum, an improved stationary B-L coupled ULDM search, and a stationary measurement with a spin pendulum constraining spin-coupled ULDM.

8.1 Rotating Equivalence Principle Test

In the short term, the goal is to assess the rotating instrument's sensitivity to astrophysical sources and dark matter. Improvements to the performance are likely possible without a significant redesign. However, we will eventually reach a decision point and decide to move forward with other plans to improve our sensitivity to new physics significantly. One avenue for this is a redesign of the pendulum to increase sensitivity to the B-L. Table 8.1 shows some potential charge dipoles that we can investigate using. The element that provides the

most significant contrast in B-L charge is hydrogen, the only element lacking in neutrons. Polyethylene is the material most readily used in a torsion balance experiment with high hydrogen content as its solid (unlike methane CH_4 for example) and is usable in vacuum after thorough out-gassing [111]. We believe that polyethylene test masses encased in a thick gold coating are adequate to reach the thermal noise limits of our fibers.

Dipole	$\Delta_{B\text{-}L}$	Δ_B	Δ_L
Be-Al	0.036	-0.00204	-0.038
Be-Ti	0.013	-0.00242	-0.016
Ti-$(C_2\ H_4)_n$	0.113	0.00219	-0.111
Cu-$(C_2\ H_4)_n$	0.116	0.00223	-0.114
Yb-$(C_2\ H_4)_n$	0.167	0.00146	-0.166

Table 8.1: Examples of charge dipoles of interest. The first two are existing options. Hydrogen-bearing dipoles that utilize polyethylene $(C_2\ H_4)_n$ are in development. The use of Ytterbium is hypothetically possible and significantly improves the B-L coupling.

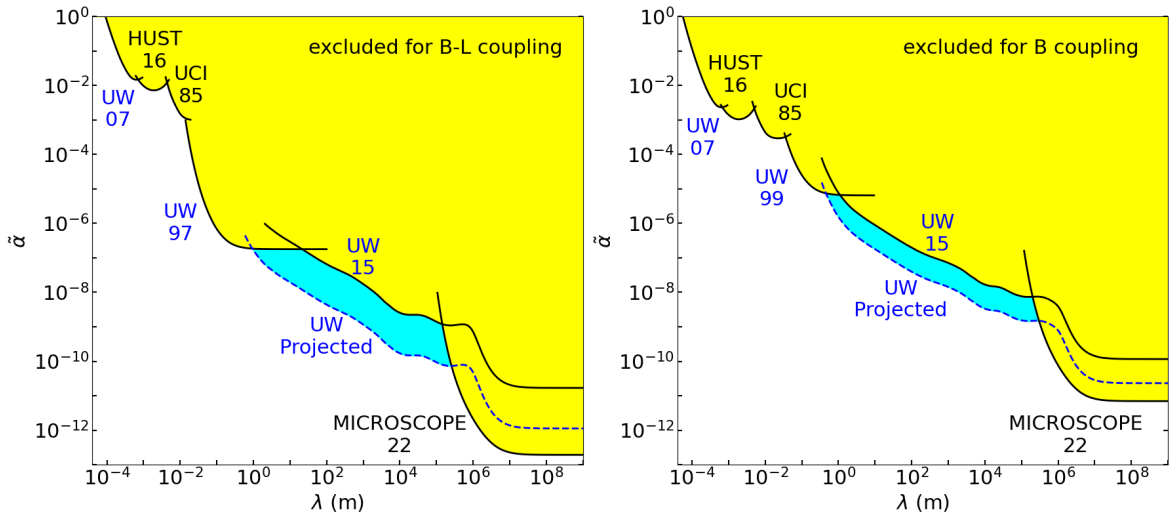

Figure 8.1: Expected 95%-confidence limits shown in blue along with our most sensitive previous limits and results from HUST [112], UCI [113], and MICROSCOPE [31]. Our other constraints on the plot are from a short-range test of gravity, UW 07 [11], and a short-range test of the equivalence principle using 3 tons of depleted uranium as the source [5].

Once we have better ways to constrain systematics for results towards the Earth, the improvements shown in Figure 8.1 enabled by fused silica and a hydrogen-bearing pendulum

will be readily achievable. Minor improvements to our angular readout could allow us to achieve the thermal noise limit at a turntable rotation rate similar to our previous results to improve further on these searches. In the long term, we can go beyond the sensitivity of MICROSCOPE with further research into fused silica fibers, using an interferometric readout, and achieving thermal noise at a much higher rotation rate.

8.2 Improved B-L Coupled ULDM Searches

To improve our stationary limits, we have begun retrofitting another instrument we initially used to constrain axionic ULDM [114]. This instrument is desirable because it enables the use of a longer fused silica fiber and has more space for optics to enable a more sensitive readout in the future. In addition to these improvements, a new hydrogen-bearing pendulum was built (Figure 8.2) with better sensitivity to B-L coupled ULDM. We plan to test this at first with a traditional autocollimator or multi-fringe autocollimator, then move to an interferometric readout that could vastly expand the science reach.

The final results from MICROSCOPE [31] are comparable to our previous test, but there is unlikely to be a next-generation space-based EP test in the near future. Hence, the parameter space where our instruments are most sensitive is unlikely to be explored by other experiments. What is more, standard EP tests are indirect measurements of the Yukawa force mediated by such particles. The signal from dark matter in such experiments is proportional to $\tilde{g}^2$ compared to a direct search where the signal is linear in $\tilde{g}$. So, drastically improving our results by a factor 10 over an extensive mass range with our plan shown in Figure 8.3 will require a factor 100 improvement in the sensitivity of space-based EP tests.

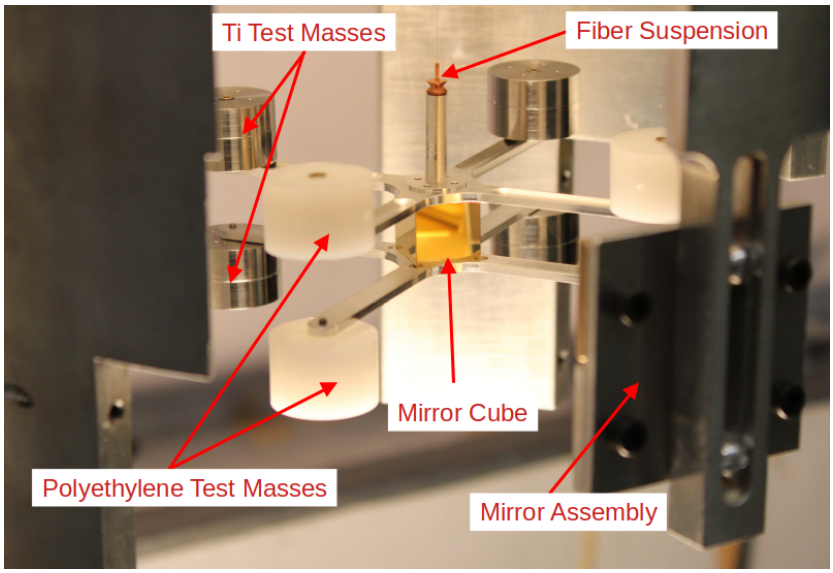

Figure 8.2: Picture of new pendulum design that is meant to maximize the charge differences Δ_{B-L} and Δ_B as well as the lever arm R, while not appreciably increasing the moment of inertia I. This pendulum will receive a thick gold-coating.

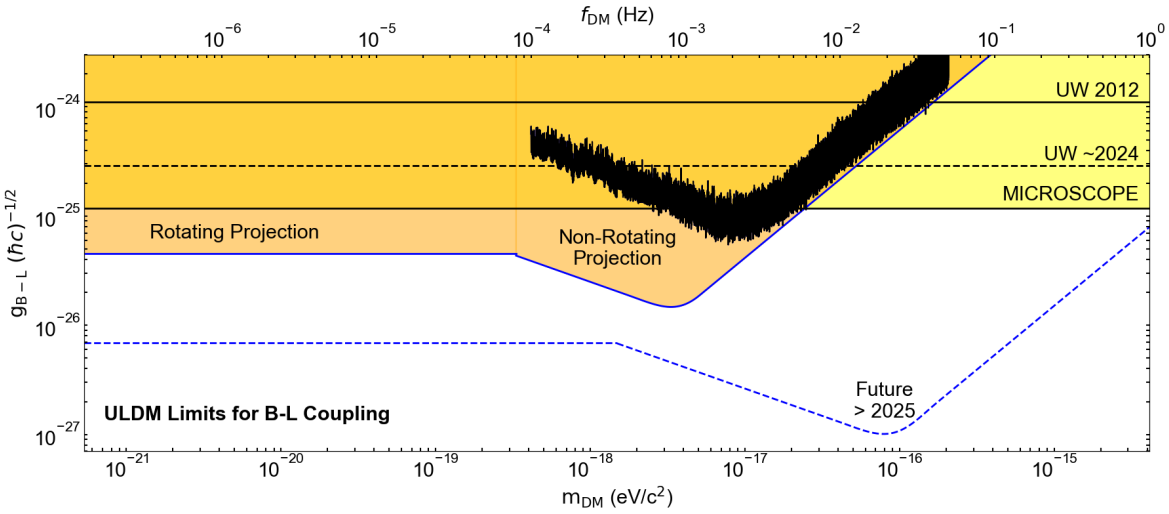

Figure 8.3: Summary of 95% C.L. limits on couplings constants $g_{\mathrm{B-L}}$. Results published with our non-rotating instrument are shown in black [92]. The orange regions are the proposed sensitivity/limits with hydrogen-rich test masses in our experiments. The dotted blue line is the vision of the projected sensitivity beyond the time frame of this dissertation. Also shown in yellow, is the region where equivalence principle tests set limits on (B-L)-coupled interactions. These limits are from our lab [8], from MICROSCOPE [31] and expected sensitivity/limits after an upgrade of our equivalence principle test in 2024.

8.3 Stationary Spin-Coupled ULDM Search

To improve searches for spin-coupled ULDM, a large polarized spin-dipole is necessary. We have previously developed pendulums with such a dipole for an EP test, ULDM search, and a short-range spin-spin interaction test [15, 16, 17, 68]. We will install a spin-dipole pendulum in a non-rotating instrument suspended from a fused-silica fiber. The sensitivity enabled by fused silica could theoretically improve our C_e/F_a (Equation 1.12) limits by a factor of ten with a much shorter (few months) science campaign. This non-rotating instrument will set limits complimentary to Reference [68] by searching at higher frequencies than a rotating experiment allows (see Figure 8.4).

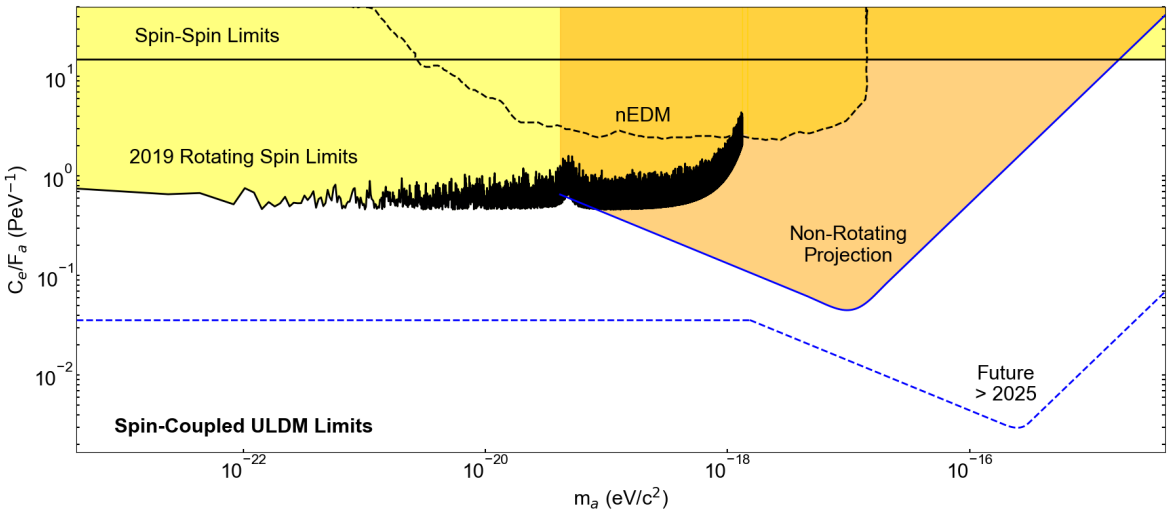

Figure 8.4: Estimated 95% exclusion-sensitivity for a non-rotating spin-coupled ULDM search. The orange region is the proposed sensitivity on a 36 μm fused silica fiber. The blue dashed horizontal line is what we could achieve with improved rotating and non-rotating experiments beyond the time frame of this proposal. The yellow region marks the parameter space constrained by our rotating and spin-spin limits [15, 16, 17, 68] and a neutron EDM limit [115].

The spin-pendulum's magnetic moment from the aligned spins may need retuning after being stored for years. Even after tuning, there will be a sizeable residual magnetic moment that may introduce extra loss and environmental coupling into the system. In

theory, operating with a fused silica fiber will improve sensitivity to torque by a factor >50, but this may be challenging to achieve in practice and may even motivate the use of the superconducting magnetic shield in our cryogenic apparatus. However, research into enabling this experiment will pave the way for an improved round of both non-rotating (with improved fiber, interferometric readout, and an extensive data campaign) and rotating (with improved fiber) spin-coupled ULDM searches that could provide much more stringent constraints over the entire parameter space shown in Figure 8.4 as well as better constrain preferred-frame interactions in a rotating apparatus.

8.4 Concluding Remarks

Fused silica opens up many valuable opportunities to expand on previous work testing the EP and searching for ULDM. There are challenges to fully realizing its potential posed by understanding and controlling systematic noise sources and readout noise, but ongoing research is expected to address these concerns. The content of this dissertation and continued work with fused silica will open up many opportunities for graduate and undergraduate work in the future and has the potential to find evidence for a plethora of hypothetical phenomena of interest to the broader physics community.

Bibliography

[1] A. royale des sciences Paris, *Histoire de l'Academie royale des sciences*. De l'imprimerie royale, 1791.

[2] H. Cavendish, "XXI. Experiments to determine the density of the earth," *Philosophical Transactions of the Royal Society of London*, vol. 88, pp. 469–526, 1798.

[3] Y. Su, B. R. Heckel, E. G. Adelberger, J. H. Gundlach, M. Harris, G. L. Smith, and H. E. Swanson, "New tests of the universality of free fall," *Phys. Rev. D*, vol. 50, pp. 3614–3636, Sep 1994.

[4] S. Baeßler, B. R. Heckel, E. G. Adelberger, J. H. Gundlach, U. Schmidt, and H. E. Swanson, "Improved Test of the Equivalence Principle for Gravitational Self-Energy," *Phys. Rev. Lett.*, vol. 83, pp. 3585–3588, Nov 1999.

[5] J. H. Gundlach, G. L. Smith, E. G. Adelberger, B. R. Heckel, and H. E. Swanson, "Short-Range Test of the Equivalence Principle," *Phys. Rev. Lett.*, vol. 78, pp. 2523–2526, Mar 1997.

[6] S. Schlamminger, K.-Y. Choi, T. A. Wagner, J. H. Gundlach, and E. G. Adelberger, "Test of the Equivalence Principle Using a Rotating Torsion Balance," *Phys. Rev. Lett.*, vol. 100, p. 041101, Jan 2008.

[7] E. Adelberger, J. Gundlach, B. Heckel, S. Hoedl, and S. Schlamminger, "Torsion

balance experiments: A low-energy frontier of particle physics," *Progress in Particle and Nuclear Physics*, vol. 62, no. 1, pp. 102–134, 2009.

[8] T. A. Wagner, S. Schlamminger, J. H. Gundlach, and E. G. Adelberger, "Torsion-balance tests of the weak equivalence principle," *Classical and Quantum Gravity*, vol. 29, p. 184002, aug 2012.

[9] C. D. Hoyle, U. Schmidt, B. R. Heckel, E. G. Adelberger, J. H. Gundlach, D. J. Kapner, and H. E. Swanson, "Submillimeter Test of the Gravitational Inverse-Square Law: A Search for "Large" Extra Dimensions," *Phys. Rev. Lett.*, vol. 86, pp. 1418–1421, Feb 2001.

[10] C. D. Hoyle, D. J. Kapner, B. R. Heckel, E. G. Adelberger, J. H. Gundlach, U. Schmidt, and H. E. Swanson, "Submillimeter tests of the gravitational inverse-square law," *Phys. Rev. D*, vol. 70, p. 042004, Aug 2004.

[11] D. J. Kapner, T. S. Cook, E. G. Adelberger, J. H. Gundlach, B. R. Heckel, C. D. Hoyle, and H. E. Swanson, "Tests of the Gravitational Inverse-Square Law below the Dark-Energy Length Scale," *Phys. Rev. Lett.*, vol. 98, p. 021101, Jan 2007.

[12] E. G. Adelberger, B. R. Heckel, S. Hoedl, C. D. Hoyle, D. J. Kapner, and A. Upadhye, "Particle-Physics Implications of a Recent Test of the Gravitational Inverse-Square Law," *Phys. Rev. Lett.*, vol. 98, p. 131104, Mar 2007.

[13] T. S. Cook, *A test of the gravitational inverse-square law at short distance*. PhD thesis, University of Washington, 2013.

[14] J. G. Lee, E. G. Adelberger, T. S. Cook, S. M. Fleischer, and B. R. Heckel, "New Test of the Gravitational $1/r^2$ Law at Separations down to 52 μm," *Phys. Rev. Lett.*, vol. 124, p. 101101, Mar 2020.

[15] B. R. Heckel, E. G. Adelberger, C. E. Cramer, T. S. Cook, S. Schlamminger, and U. Schmidt, "Preferred-frame and *CP*-violation tests with polarized electrons," *Phys. Rev. D*, vol. 78, p. 092006, Nov 2008.

[16] W. A. Terrano, B. R. Heckel, and E. G. Adelberger, "Search for a proposed signature of Lorentz-invariant spacetime granularity," *Classical and Quantum Gravity*, vol. 28, p. 145011, jun 2011.

[17] B. R. Heckel, W. A. Terrano, and E. G. Adelberger, "Limits on Exotic Long-Range Spin-Spin Interactions of Electrons," *Phys. Rev. Lett.*, vol. 111, p. 151802, Oct 2013.

[18] W. A. Terrano, E. G. Adelberger, J. G. Lee, and B. R. Heckel, "Short-Range, Spin-Dependent Interactions of Electrons: A Probe for Exotic Pseudo-Goldstone Bosons," *Phys. Rev. Lett.*, vol. 115, p. 201801, Nov 2015.

[19] J. H. Gundlach and S. M. Merkowitz, "Measurement of Newton's Constant Using a Torsion Balance with Angular Acceleration Feedback," *Phys. Rev. Lett.*, vol. 85, pp. 2869–2872, Oct 2000.

[20] A. Press, *On the Heavens*. Aris & Phillips, 1995.

[21] Bessel, "Versuche über die Kraft, mit welcher die Erde Körper von verschiedener Beschaffenheit anzieht," *Annalen der Physik*, vol. 101, no. 7, pp. 401–417, 1832.

[22] H. H. Potter and O. W. Richardson, "Some experiments on the proportionality of mass and weight," *Proceedings of the Royal Society of London. Series A, Containing Papers of a Mathematical and Physical Character*, vol. 104, no. 728, pp. 588–610, 1923.

[23] S. Weinberg and W. Steven, *Gravitation and Cosmology: Principles and Applications of the General Theory of Relativity*. Wiley, 1972.

[24] R. von Eötvös, *Mathematische und naturwissenschaftliche Berichte aus Ungarn*. R. Friedländer & Sohn, 1883.

[25] R. v. Eötvös, D. Pekár, and E. Fekete, "Beiträge zum Gesetze der Proportionalität von Trägheit und Gravität," *Annalen der Physik*, vol. 373, no. 9, pp. 11–66, 1922.

[26] P. Roll, R. Krotkov, and R. Dicke, "The equivalence of inertial and passive gravitational mass," *Annals of Physics*, vol. 26, no. 3, pp. 442–517, 1964.

[27] V. B. Braginsky and V. I. Panov, "The equivalence of inertial and passive gravitational mass," *General Relativity and Gravitation*, vol. 3, pp. 403–404, 1972.

[28] E. Fischbach, D. Sudarsky, A. Szafer, C. Talmadge, and S. H. Aronson, "Reanalysis of the Eötvös experiment," *Phys. Rev. Lett.*, vol. 56, pp. 3–6, Jan 1986.

[29] C. W. Stubbs, E. G. Adelberger, F. J. Raab, J. H. Gundlach, B. R. Heckel, K. D. McMurry, H. E. Swanson, and R. Watanabe, "Search for an intermediate-range interaction," *Phys. Rev. Lett.*, vol. 58, pp. 1070–1073, Mar 1987.

[30] P. Touboul, G. Métris, M. Rodrigues, Y. André, Q. Baghi, J. Bergé, *et al.*, "MICROSCOPE Mission: First Results of a Space Test of the Equivalence Principle," *Phys. Rev. Lett.*, vol. 119, p. 231101, Dec 2017.

[31] P. Touboul, G. Métris, M. Rodrigues, J. Bergé, A. Robert, Q. Baghi, *et al.*, "MICROSCOPE Mission: Final Results of the Test of the Equivalence Principle," *Phys. Rev. Lett.*, vol. 129, p. 121102, Sep 2022.

[32] T. Li, F. Wang, and J. M. Yang, "The $SU(3)_C \times SU(4)_W \times U(1)_{B-L}$ models with left–right unification," *Nuclear Physics B*, vol. 820, no. 1, pp. 534–564, 2009.

[33] F. Buccella, G. Mangano, A. Masiero, and L. Rosa, "Baryogenesis via B-L violation in SO(10) unified models," *Physics Letters B*, vol. 320, no. 3, pp. 313–319, 1994.

[34] D. B. Kaplan and M. B. Wise, "Couplings of a light dilaton and violations of the equivalence principle," *Journal of High Energy Physics*, vol. 2000, pp. 037–037, aug 2000.

[35] K. Nordtvedt, "Lunar laser ranging and laboratory Eötvös-type experiments," *Phys. Rev. D*, vol. 37, pp. 1070–1071, Feb 1988.

[36] C. W. Stubbs, "Experimental limits on any long range nongravitational interaction between dark matter and ordinary matter," *Phys. Rev. Lett.*, vol. 70, pp. 119–122, Jan 1993.

[37] P. Scampoli and J. Storey, "The AEgIS experiment at CERN for the measurement of antihydrogen gravity acceleration," *Modern Physics Letters A*, vol. 29, no. 17, p. 1430017, 2014.

[38] D. S. M. Alves, M. Jankowiak, and P. Saraswat, "Experimental constraints on the free fall acceleration of antimatter," 2009.

[39] D. Colladay and V. A. Kostelecký, "CPT violation and the standard model," *Phys. Rev. D*, vol. 55, pp. 6760–6774, Jun 1997.

[40] R. Bluhm and V. A. Kostelecký, "Lorentz and *CPT* Tests with Spin-Polarized Solids," *Phys. Rev. Lett.*, vol. 84, pp. 1381–1384, Feb 2000.

[41] Y. V. Stadnik, "New bounds on macroscopic scalar-field topological defects from nontransient signatures due to environmental dependence and spatial variations of the fundamental constants," *Phys. Rev. D*, vol. 102, p. 115016, Dec 2020.

[42] Y. V. Stadnik, "Robust laboratory limits on a cosmological spatial gradient in the electromagnetic fine-structure constant from accelerometer experiments," *Phys. Rev. A*, vol. 103, p. 062807, Jun 2021.

[43] W. Thomson and B. Kelvin, *Baltimore Lectures on Molecular Dynamics and the Wave Theory of Light.* Cambridge University Press, 1904.

[44] F. Zwicky, "Die Rotverschiebung von extragalaktischen Nebeln," *Helvetica Physica Acta*, vol. 6, no. II, p. 110, 1933.

[45] V. C. Rubin, J. Ford, W. K., and N. Thonnard, "Rotational properties of 21 SC galaxies with a large range of luminosities and radii, from NGC 4605 (R=4kpc) to UGC 2885 (R=122kpc).," ApJ, vol. 238, pp. 471–487, June 1980.

[46] P. Collaboration, P. A. R. Ade, N. Aghanim, M. Arnaud, M. Ashdown, J. Aumont, *et al.*, "Planck 2015 results. XIII. Cosmological parameters," A&A, vol. 594, p. A13, Sept. 2016.

[47] D. Clowe, A. Gonzalez, and M. Markevitch, "Weak-Lensing Mass Reconstruction of the Interacting Cluster 1E 0657–558: Direct Evidence for the Existence of Dark Matter," *The Astrophysical Journal*, vol. 604, p. 596, apr 2004.

[48] G. Jungman, M. Kamionkowski, and K. Griest, "Supersymmetric dark matter," *Physics Reports*, vol. 267, no. 5, pp. 195–373, 1996.

[49] L. Roszkowski, E. M. Sessolo, and S. Trojanowski, "WIMP dark matter candidates and searches—current status and future prospects," *Reports on Progress in Physics*, vol. 81, p. 066201, may 2018.

[50] J. Billard, E. Figueroa-Feliciano, and L. Strigari, "Implication of neutrino backgrounds on the reach of next generation dark matter direct detection experiments," *Phys. Rev. D*, vol. 89, p. 023524, Jan 2014.

[51] W. J. G. de Blok, "The core-cusp problem," *Advances in Astronomy*, vol. 2010, pp. 1–14, 2010.

[52] H. Deng, M. P. Hertzberg, M. H. Namjoo, and A. Masoumi, “Can light dark matter solve the core-cusp problem?,” *Physical Review D*, vol. 98, jul 2018.

[53] H.-Y. Schive, T. Chiueh, and T. Broadhurst, “Cosmic structure as the quantum interference of a coherent dark wave,” *Nature Physics*, vol. 10, pp. 496–499, Jul 2014.

[54] A. Del Popolo and M. Le Delliou, “Review of Solutions to the Cusp-Core Problem of the ΛCDM Model,” *Galaxies*, vol. 9, no. 4, 2021.

[55] A. Amruth, T. Broadhurst, J. Lim, M. Oguri, G. F. Smoot, J. M. Diego, E. Leung, R. Emami, J. Li, T. Chiueh, H.-Y. Schive, M. C. H. Yeung, and S. K. Li, “Einstein rings modulated by wavelike dark matter from anomalies in gravitationally lensed images,” *Nature Astronomy*, Apr 2023.

[56] L. Hui, “Wave Dark Matter,” *Annual Review of Astronomy and Astrophysics*, vol. 59, no. 1, pp. 247–289, 2021.

[57] J. Bovy *et al.*, “The Milky Way’s circular velocity curve between 4 and 14 kpc from APOGEE data,” *The Astrophysical Journal*, vol. 759, p. 131, oct 2012.

[58] L. de Broglie, *Research on Quantum Theory*. PhD thesis, University of Paris, 1924.

[59] R. D. Peccei, “The Strong CP Problem and Axions,” *Axions*, p. 3–17, 2008.

[60] P. Sikivie, “Experimental Tests of the "Invisible" Axion,” *Phys. Rev. Lett.*, vol. 51, pp. 1415–1417, Oct 1983.

[61] K. M. Backes, D. A. Palken, S. A. Kenany, B. M. Brubaker, S. B. Cahn, A. Droster, *et al.*, “A quantum enhanced search for dark matter axions,” *Nature*, vol. 590, pp. 238–242, Feb 2021.

[62] O. Kwon, D. Lee, W. Chung, D. Ahn, H. Byun, F. Caspers, *et al.*, "First Results from an Axion Haloscope at CAPP around 10.7 μeV," *Phys. Rev. Lett.*, vol. 126, p. 191802, May 2021.

[63] A. Collaboration, C. Bartram, T. Braine, E. Burns, R. Cervantes, N. Crisosto, *et al.*, "Search for "Invisible" Axion Dark Matter in the 3.3-4.2 μeV Mass Range," 2021.

[64] C. J. Kennedy, E. Oelker, J. M. Robinson, T. Bothwell, D. Kedar, W. R. Milner, G. E. Marti, A. Derevianko, and J. Ye, "Precision Metrology Meets Cosmology: Improved Constraints on Ultralight Dark Matter from Atom-Cavity Frequency Comparisons," *Phys. Rev. Lett.*, vol. 125, p. 201302, Nov 2020.

[65] A. Arvanitaki, J. Huang, and K. Van Tilburg, "Searching for dilaton dark matter with atomic clocks," *Physical Review D*, vol. 91, p. 015015, Jan 2015.

[66] S. M. Vermeulen, P. Relton, H. Grote, V. Raymond, C. Affeldt, F. Bergamin, *et al.*, "Direct limits for scalar field dark matter from a gravitational-wave detector," *Nature*, vol. 600, pp. 424–428, Dec 2021.

[67] C. Abel, N. J. Ayres, G. Ban, G. Bison, K. Bodek, V. Bondar, *et al.*, "Search for Axionlike Dark Matter through Nuclear Spin Precession in Electric and Magnetic Fields," *Phys. Rev. X*, vol. 7, p. 041034, Nov 2017.

[68] W. A. Terrano, E. G. Adelberger, C. A. Hagedorn, and B. R. Heckel, "Constraints on Axionlike Dark Matter with Masses Down to 10^{-23} eV$/c^2$," *Phys. Rev. Lett.*, vol. 122, p. 231301, Jun 2019.

[69] C. Smorra, Y. V. Stadnik, P. E. Blessing, M. Bohman, M. J. Borchert, J. A. Devlin, *et al.*, "Direct limits on the interaction of antiprotons with axion-like dark matter," *Nature*, vol. 575, pp. 310–314, Nov 2019.

[70] A. Wagner, G. Rybka, M. Hotz, L. J. Rosenberg, S. J. Asztalos, G. Carosi, *et al.*, "Search for Hidden Sector Photons with the ADMX Detector," *Phys. Rev. Lett.*, vol. 105, p. 171801, Oct 2010.

[71] A. V. Dixit, S. Chakram, K. He, A. Agrawal, R. K. Naik, D. I. Schuster, and A. Chou, "Searching for Dark Matter with a Superconducting Qubit," *Phys. Rev. Lett.*, vol. 126, p. 141302, Apr 2021.

[72] P. W. Graham, D. E. Kaplan, J. Mardon, S. Rajendran, and W. A. Terrano, "Dark matter direct detection with accelerometers," *Phys. Rev. D*, vol. 93, p. 075029, Apr 2016.

[73] A. E. Nelson and J. Scholtz, "Dark light, dark matter, and the misalignment mechanism," *Phys. Rev. D*, vol. 84, p. 103501, Nov 2011.

[74] P. R. Saulson, "Thermal noise in mechanical experiments," *Phys. Rev. D*, vol. 42, pp. 2437–2445, Oct 1990. The thermal noise limit was derived using equations (5) and (14), substituting the torsion constant κ in place of the spring constant.

[75] S. M. Fleischer, E. Adelberger, M. Bassan, and B. Heckel, "A cryogenic torsion balance for tests of the equivalence principle," 02 2010.

[76] S. M. Fleischer, M. P. Ross, K. Venkateswara, C. A. Hagedorn, E. A. Shaw, E. Swanson, B. R. Heckel, and J. H. Gundlach, "A cryogenic torsion balance using a liquid-cryogen free, ultra-low vibration cryostat," *Review of Scientific Instruments*, vol. 93, no. 6, p. 064505, 2022.

[77] C. J. de Matos, "Physical Vacuum in Superconductors," *Journal of Superconductivity and Novel Magnetism*, vol. 23, pp. 1443–1453, Dec 2010.

[78] T. A. Wagner, *Rotating torsion balance tests of the weak equivalence principle*. PhD thesis, University of Washington, 2014.

[79] T. B. Arp, C. A. Hagedorn, S. Schlamminger, and J. H. Gundlach, "A reference-beam autocollimator with nanoradian sensitivity from mHz to kHz and dynamic range of 10^7," *Review of Scientific Instruments*, vol. 84, no. 9, p. 095007, 2013.

[80] M. P. Ross, K. Venkateswara, C. A. Hagedorn, C. J. Leupold, P. W. F. Forsyth, J. D. Wegner, E. A. Shaw, J. G. Lee, and J. H. Gundlach, "A low-frequency torsion pendulum with interferometric readout," *Review of Scientific Instruments*, vol. 92, no. 5, p. 054502, 2021.

[81] M. D. Turner, *Development of new technologies for precision torsion-balance experiments*. PhD thesis, University of Washington, 2017.

[82] S. J. Cooper, C. J. Collins, A. C. Green, D. Hoyland, C. C. Speake, A. Freise, and C. M. Mow-Lowry, "A compact, large-range interferometer for precision measurement and inertial sensing," *Classical and Quantum Gravity*, vol. 35, p. 095007, mar 2018.

[83] J. Harms, L. Naticchioni, E. Calloni, R. De Rosa, F. Ricci, and D. D'Urso, "A lower limit for Newtonian-noise models of the Einstein Telescope," *The European Physical Journal Plus*, vol. 137, p. 687, Jun 2022.

[84] G. T. Gillies and R. C. Ritter, "Torsion balances, torsion pendulums, and related devices," *Review of Scientific Instruments*, vol. 64, no. 2, pp. 283–309, 1993.

[85] K. Numata, J. Horowitz, and J. Camp, "Coated fused silica fibers for enhanced sensitivity torsion pendulum for LISA," *Physics Letters A*, vol. 370, no. 2, pp. 91–98, 2007.

[86] T. L. S. Collaboration, J. Aasi, B. P. Abbott, R. Abbott, T. Abbott, M. R. Abernathy, K. Ackley, *et al.*, "Advanced LIGO," *Classical and Quantum Gravity*, vol. 32, p. 074001, mar 2015.

[87] A. Ageev, B. C. Palmer, A. D. Felice, S. D. Penn, and P. R. Saulson, "Very high quality factor measured in annealed fused silica," *Classical and Quantum Gravity*, vol. 21, p. 3887, jul 2004.

[88] K. Numata, J. Horowitz, and J. Camp, "Coated fused silica fibers for enhanced sensitivity torsion pendulum for LISA," *Physics Letters A*, vol. 370, no. 2, pp. 91–98, 2007.

[89] S. D. Penn, A. Ageev, D. Busby, G. M. Harry, A. M. Gretarsson, K. Numata, and P. Willems, "Frequency and surface dependence of the mechanical loss in fused silica," *Physics Letters A*, vol. 352, no. 1, pp. 3–6, 2006.

[90] I. A. Bilenko, V. B. Braginsky, and S. L. Lourie, "Mechanical losses in thin fused silica fibres," *Classical and Quantum Gravity*, vol. 21, p. S1231, feb 2004.

[91] B. A. Proctor, I. Whitney, J. W. Johnson, and A. H. Cottrell, "The strength of fused silica," *Proceedings of the Royal Society of London. Series A. Mathematical and Physical Sciences*, vol. 297, no. 1451, pp. 534–557, 1967.

[92] E. A. Shaw, M. P. Ross, C. A. Hagedorn, E. G. Adelberger, and J. H. Gundlach, "Torsion-balance search for ultralow-mass bosonic dark matter," *Phys. Rev. D*, vol. 105, p. 042007, Feb 2022.

[93] H. J. McNicholas and H. J. Curtis, "Measurement of fiber diameters by the diffraction method," *Review of Scientific Instruments*, vol. 2, no. 5, pp. 263–286, 1931.

[94] M. P. Ross, *Precision Mechanical Rotation Sensors for Terrestrial Gravitational Wave Observatories*. PhD thesis, University of Washington, 2020.

[95] R. Cowsik, R. Srinivasan, S. Kasturirengan, A. S. Kumar, and K. Wagoner, "Design

and performance of a sub-nanoradian resolution autocollimating optical lever," *Review of Scientific Instruments*, vol. 78, 03 2007. 035105.

[96] S. Schlamminger, C. A. Hagedorn, and J. H. Gundlach, "Indirect evidence for Lévy walks in squeeze film damping," *Phys. Rev. D*, vol. 81, p. 123008, Jun 2010.

[97] B. Fornberg, "Generation of Finite Difference Formulas on Arbitrarily Spaced Grids," *Mathematics of Computation*, vol. 51, no. 184, pp. 699–706, 1988.

[98] R. W. Hamming, *Digital Filters (3rd Ed.)*. GBR: Prentice Hall International (UK) Ltd., 1989. We applied a Type II FIR lowpass filter with 80 mHz cutoff frequency. It is a 100 point Sinc filter similar to the example low pass filter in section 6.2A only with a Hamming window applied.

[99] A. M. Price-Whelan, B. M. Sipőcz, H. M. Günther, P. L. Lim, S. M. Crawford, S. Conseil, D. L. Shupe, M. W. Craig, N. Dencheva, *et al.*, "The Astropy Project: Building an Open-science Project and Status of the v2.0 Core Package," *The Astronomical Journal*, vol. 156, p. 123, Aug 2018.

[100] S. O. Rice, "Mathematical Analysis of Random Noise," *Bell System Technical Journal*, vol. 23, pp. 282–332, Jan. 1944.

[101] P. Fayet, "MICROSCOPE limits for new long-range forces and implications for unified theories," *Phys. Rev. D*, vol. 97, p. 055039, Mar 2018.

[102] P. Virtanen, R. Gommers, T. E. Oliphant, M. Haberland, T. Reddy, D. Cournapeau, *et al.*, "SciPy 1.0: Fundamental Algorithms for Scientific Computing in Python," *Nature Methods*, vol. 17, pp. 261–272, 2020.

[103] G. P. Centers, J. W. Blanchard, J. Conrad, N. L. Figueroa, A. Garcon, A. V. Gramolin, *et al.*, "Stochastic fluctuations of bosonic dark matter," 2020.

[104] M. Lisanti, M. Moschella, and W. Terrano, "Stochastic properties of ultralight scalar field gradients," *Phys. Rev. D*, vol. 104, p. 055037, Sep 2021.

[105] A. Derevianko, "Detecting dark-matter waves with a network of precision-measurement tools," *Phys. Rev. A*, vol. 97, p. 042506, Apr 2018.

[106] J. W. Foster, N. L. Rodd, and B. R. Safdi, "Revealing the dark matter halo with axion direct detection," *Phys. Rev. D*, vol. 97, p. 123006, Jun 2018.

[107] C. A. J. O'Hare, C. McCabe, N. W. Evans, G. Myeong, and V. Belokurov, "Dark matter hurricane: Measuring the S1 stream with dark matter detectors," *Phys. Rev. D*, vol. 98, p. 103006, Nov 2018.

[108] A. Fattahi, V. Belokurov, A. J. Deason, C. S. Frenk, F. A. Gómez, R. J. J. Grand, F. Marinacci, R. Pakmor, and V. Springel, "The origin of galactic metal-rich stellar halo components with highly eccentric orbits," *Monthly Notices of the Royal Astronomical Society*, vol. 484, pp. 4471–4483, 01 2019.

[109] L. Necib, M. Lisanti, S. Garrison-Kimmel, A. Wetzel, R. Sanderson, P. F. Hopkins, C.-A. Faucher-Giguère, and D. Kereš, "Under the FIRElight: Stellar Tracers of the Local Dark Matter Velocity Distribution in the Milky Way," *The Astrophysical Journal*, vol. 883, p. 27, Sep 2019.

[110] P. W. Graham and S. Rajendran, "New observables for direct detection of axion dark matter," *Phys. Rev. D*, vol. 88, p. 035023, Aug 2013.

[111] L. N. Dinh, J. Sze, M. A. Schildbach, S. C. Chinn, R. S. Maxwell, P. Raboin, and I. McLean, W., "Vacuum outgassing of high density polyethylene," *Journal of Vacuum Science & Technology A*, vol. 27, pp. 376–380, 02 2009.

[112] W.-H. Tan, S.-Q. Yang, C.-G. Shao, J. Li, A.-B. Du, B.-F. Zhan, Q.-L. Wang, P.-S. Luo, L.-C. Tu, and J. Luo, "New Test of the Gravitational Inverse-Square Law at the Submillimeter Range with Dual Modulation and Compensation," *Phys. Rev. Lett.*, vol. 116, p. 131101, Mar 2016.

[113] J. K. Hoskins, R. D. Newman, R. Spero, and J. Schultz, "Experimental tests of the gravitational inverse-square law for mass separations from 2 to 105 cm," *Phys. Rev. D*, vol. 32, pp. 3084–3095, Dec 1985.

[114] S. A. Hoedl, F. Fleischer, E. G. Adelberger, and B. R. Heckel, "Improved Constraints on an Axion-Mediated Force," *Phys. Rev. Lett.*, vol. 106, p. 041801, Jan 2011.

[115] C. Abel, N. J. Ayres, G. Ban, G. Bison, K. Bodek, V. Bondar, *et al.*, "Search for Axionlike Dark Matter through Nuclear Spin Precession in Electric and Magnetic Fields," *Phys. Rev. X*, vol. 7, p. 041034, Nov 2017.

[116] C. D'Urso and E. G. Adelberger, "Translation of multipoles for a $1/r$ potential," *Phys. Rev. D*, vol. 55, pp. 7970–7972, Jun 1997.

[117] E. G. Adelberger, N. A. Collins, and C. D. Hoyle, "Analytic expressions for gravitational inner multipole moments of elementary solids and for the force between two rectangular solids," *Classical and Quantum Gravity*, vol. 23, p. 5463, sep 2006.

[118] C. D'Urso and E. G. Adelberger, "Translation of multipoles for a $1/r$ potential," *Phys. Rev. D*, vol. 55, pp. 7970–7972, Jun 1997.

Appendices

A: Torsion Balance EP tests

Using the picture given by Figure 1.1 and neglecting gravity gradients, both test masses experience the same gravitational acceleration $\boldsymbol{g} = -g\hat{\boldsymbol{z}}_{lab}$ where $g = 9.8$ m/s^2 and $\hat{\boldsymbol{z}}_{lab}$ is local vertical. For simplicity, we define the lab coordinate system with true north $\hat{\boldsymbol{x}}_{lab}$ being perpendicular to the rod axis and $\hat{\boldsymbol{y}}_{lab}$ completing the coordinate system pointing along the rod. In addition to gravitational acceleration, this setup experiences a centripetal acceleration in terrestrial experiments due to the rotation of the Earth at angular frequency $\omega_\oplus = 2\pi f_\oplus$ where $f_\oplus$ is the sidereal frequency of the Earth. Given the radius of the Earth $R_\oplus$ and a lab latitude θ_{lab}, it is easy to show that the centripetal acceleration $\boldsymbol{a}_c$ and total acceleration $\boldsymbol{a} = \boldsymbol{g} + \boldsymbol{a}_c$ felt by the pendulum in the lab are:

$$\vec{a}_c = -\omega_\oplus^2 R_\oplus \sin\theta_{lab}\cos\theta_{lab}\hat{\boldsymbol{x}}_{lab} + {\omega_\oplus}^2 R_\oplus \cos^2\theta_{lab}\hat{\boldsymbol{z}}_{lab}$$

$$\vec{a} = -\omega_\oplus^2 R_\oplus \sin\theta_{lab}\cos\theta_{lab}\hat{\boldsymbol{x}}_{lab} + (\omega_\oplus^2 R_\oplus \cos^2\theta_{lab} - g)\hat{z}_{lab}$$

This formula yields several observations. At the North and South poles or on the equator $\theta_{lab} = 0, \pi/2, \pi$ the acceleration is purely along $\hat{\boldsymbol{z}}_{lab}$ and $\hat{\boldsymbol{z}}$, the fiber axis, is parallel to local down. Hence, there is no sensitivity to an EP-violating torque from the Earth on the pendulum. The optimal angles for an EP experiment are $\theta_{lab} = \pi/4, 3\pi/4$. A more detailed

analysis would take into account that Earth's radius varies, but given the less than 1% change on $R_\oplus$ from the summit of Chimborazo to the Ocean floor, the contribution is negligible. At these latitudes, a torsion balance hangs off the z-axis of the lab frame by a couple of mrad away from the nearest pole (North for the Northern Hemisphere and South for the Southern Hemisphere). So, there are plenty of places where these experiments are worth setting up: the Northern US, parts of Argentina, Chile, several places in Southern Europe, and some countries on the southern border of Russia. Seattle, where our lab is, is a great choice with a latitude of 47.6°. A test mass on a pendulum here experiences a sideways acceleration due to the Earth of 1.68 cm/s^2

Now we will discuss how a simple balance like in Figure 1.1 oriented for maximal EP violation produces a null test of EP. Or in other words, I'll show that if $m_i^{(A)} = m_g^{(A)}$ and $m_i^{(B)} = m_g^{(B)}$, then there is no torque on the balance. Since the balance hangs off-axis, both test masses experience a component of $\boldsymbol{g}$ along $\hat{x}$. We call the gravitational acceleration in this direction g_N and start by assuming this is equal for both test masses. We also define $\boldsymbol{r}_A$ and $\boldsymbol{r}_B$ as the vector positions of the A and B test masses, respectively. With these definitions, we can write the following equations of motion for the two test masses: $\boldsymbol{F}_A = m_i^{(A)}\ddot{\boldsymbol{r}}_A = m_g^{(A)}\boldsymbol{g}$ and $\boldsymbol{F}_B = m_i^{(B)}\ddot{\boldsymbol{r}}_B = m_g^{(B)}\boldsymbol{g}$. For simplicity, we consider the case where the pendulum is balanced so that we do not expect any torque due to gravity $m_g^{(A)} g_N r_A = m_g^{(B)} g_N r_B$. This expression is equivalent to the expression $r_A(\boldsymbol{F_A}\cdot\hat{\boldsymbol{x}}) = r_B(\boldsymbol{F_B}\cdot\hat{\boldsymbol{x}})$, hence we can surmise that $m_g^{(A)} r_A = m_g^{(B)} r_B$ and $m_i^{(A)} r_A = m_i^{(B)} r_B$. Then we have the relation $r_A = l - r_B$ where l is the distance A to B, so plugging in and solving for r_A and r_B we find similar expressions $r_A = m_i^{(B)} l / \left(m_i^{(A)} + m_i^{(B)}\right)$ and $r_B = m_i^{(A)} l / \left(m_i^{(A)} + m_i^{(B)}\right)$ and $m_i^{(A)} r_A = m_i^{(B)} r_B = m_i^{(A)} m_i^{(B)} l / \left(m_i^{(A)} + m_i^{(B)}\right)$. The torque about the fiber axis is $\tau_z = \left(m_i^{(A)} r_A \ddot{\boldsymbol{r}}_A - m_i^{(B)} r_B \ddot{\boldsymbol{r}}_B\right)\cdot\hat{\boldsymbol{x}}$. Additionally, $\ddot{\boldsymbol{r}}_A\cdot\hat{\boldsymbol{x}} = m_g^{(A)} g_N / m_i^{(A)}$ and $\ddot{\boldsymbol{r}}_B\cdot\hat{\boldsymbol{x}} = m_g^{(B)} g_N / m_i^{(B)}$.

Plugging in the above equations, we get an expression for the torque:

$$\tau_z = \frac{m_i^{(A)} m_i^{(B)} l}{m_i^{(A)} + m_i^{(B)}} \left(\frac{m_g^{(A)}}{m_i^{(A)}} - \frac{m_g^{(B)}}{m_i^{(B)}} \right) g_N$$

Hence, we see that the expression inside the parentheses is uniquely 0 if EP holds ($m_i^{(A)} = m_g^{(A)}$ and $m_i^{(B)} = m_g^{(B)}$). Moreover, it is clear that central to this test is to constrain how constant g_N is for the two test masses. In reality, we are sensitive to gravity gradients. The pendulum can not be perfectly balanced, which turns out not to be as big an issue when we derive the full expression 1.2; a torsion balance is only sensitive to the differential acceleration on the test masses regardless of weight or lever arm because the pendulum hangs to balance out those forces. We can write $\hat{\boldsymbol{z}}$ as being in the direction opposite the sum of the forces on the test bodies;

$$\hat{\boldsymbol{z}} = -\frac{\boldsymbol{F}_A + \boldsymbol{F}_B}{|\boldsymbol{F}_A + \boldsymbol{F}_B|}.$$

Then we find the torque about this axis is $\tau_z = \hat{\boldsymbol{z}} \cdot (\boldsymbol{r}_A \times \boldsymbol{F}_A + \boldsymbol{r}_B \times \boldsymbol{F}_B)$

$$\Rightarrow \tau_z = \frac{-(\boldsymbol{F}_A + \boldsymbol{F}_B) \cdot (\boldsymbol{r}_A \times \boldsymbol{F}_A + \boldsymbol{r}_B \times \boldsymbol{F}_B)}{|\boldsymbol{F}_A + \boldsymbol{F}_B|} = \frac{-\boldsymbol{r}_A \cdot (\boldsymbol{F}_A \times \boldsymbol{F}_B) - \boldsymbol{r}_B \cdot (\boldsymbol{F}_B \times \boldsymbol{F}_A)}{|\boldsymbol{F}_A + \boldsymbol{F}_B|}$$

$$= \frac{(\boldsymbol{r}_B - \boldsymbol{r}_A) \cdot (\boldsymbol{F}_A \times \boldsymbol{F}_B)}{|\boldsymbol{F}_A + \boldsymbol{F}_B|}.$$

From this, we see that the torque is proportional to the difference in the directions of the forces and is most sensitive to it in the plane perpendicular to the rod. From the above expression, it is unclear that the rod needs to be level, but $\boldsymbol{g}$ does vary with height. An nm displacement up or down changes the gravitational acceleration towards the Earth on the order of 10^{-15} m/s^2. This height sensitivity motivates careful balancing and metrology of the orientation of the pendulum as well as gravity gradient measurements to ensure nullification of this systematic effect to high enough accuracy and precision not to be a limiting factor in our results.

B: Multipole Formalism

To understand the gravity gradient systematic, modeling complicated mass distributions is crucial. We achieve this with high precision using multipole formalism [116]. Some tools available are analytical expressions for a variety of different shapes [117] as well as expressions for how to translate and rotate multipoles [118]. Eric Adelberger developed in-house Fortran analysis software MULTIN to calculate the gravitational interaction with this formalism. We have also developed python code to implement much of the same basic functionality called the Newtonian Eöt-Wash Toolkit. Here we briefly introduce the relevant aspects of this formalism used to constrain the effects of gravity gradients on our experiments.

We call the multipoles of the pendulum the inner multipoles:

$$q_{lm} = \int \rho_p(\boldsymbol{r}) r^l Y^*_{lm}(\hat{\boldsymbol{r}}) d^3 r. \tag{1}$$

The multipoles of the source distribution, are the outer multipoles:

$$Q_{lm} = \int \rho_s(\boldsymbol{r}) r^{-(l+1)} Y_{lm}(\hat{\boldsymbol{r}}) d^3 r. \tag{2}$$

Y_{lm} are spherical harmonics and the density functions $\rho_p(\boldsymbol{r})$ and $\rho_s(\boldsymbol{r})$ are the pendulum and source bodies, respectively. Figure B.1 shows the density distributions associated with various values of l and m.

Expanding the gravitational potential energy of the test mass in terms of these multipoles in a way equivalent to electrostatics yields

$$V = -4\pi G \sum_{l=0}^{\infty} \frac{1}{2l+1} \sum_{m=-l}^{l} q_{lm} Q_{lm}. \tag{3}$$

The forces exerted on the torsion balance are then derivatives of this potential. In a modern equivalence principle test using a torsion balance, the torsion balance apparatus

rotates relative to the source distribution in order to modulate an EP-violating signal and experiences torques at all the harmonics of the turntable frequency due to the interaction of the Q_{lm} fields. As the turntable rotates $q_{lm} \to q_{lm}e^{-im\phi}$ where ϕ is the turntable angle. For a given m, the contribution of the torque is equivalent to $-m$, so we consider $m \geq 0$ and include the contribution of $-m$ in our expression. Taking all this into consideration, the gravitational torque exerted by each multipole moment is

$$\tau_{lm}(\phi) = 4\pi G \frac{m}{2l+1} \mathrm{Re}\left[i \left(q^*_{lm} Q^*_{lm} e^{im\phi} - q_{lm} Q_{lm} e^{-im\phi} \right) \right]. \tag{4}$$

Since the science signal in these experiments would show up at the 1st harmonic of the turntable, this formalism simplifies what multipole moments to constrain as systematics, namely the ones with $m = 1$. The torsion balance hangs such that the center of mass is below the suspension point $q_{11} = 0$, making it only necessary to constrain for $l > 1$. Another thing to note is that since $Q_{lm} \propto r^{-(l+1)}$, the larger l is, the less significant the contribution to the gravitational torque as our sources are further away than a meter. Previously we have only needed to constrain the effect of the environmental Q_{21} and Q_{31}. In particular, mitigating the most significant contribution from the Q_{21} is crucial. If we can make that negligible, we can focus more on compensating for the Q_{31}, and it may become necessary to constrain for even larger l in which case we would need more in-situ measurement and compensation schemes. We found [78], however, that the effect of the Q_{41} would be many orders of magnitude smaller than the Q_{21} and Q_{31}, so it is unlikely that it will become a leading cause of systematic uncertainty any time soon.

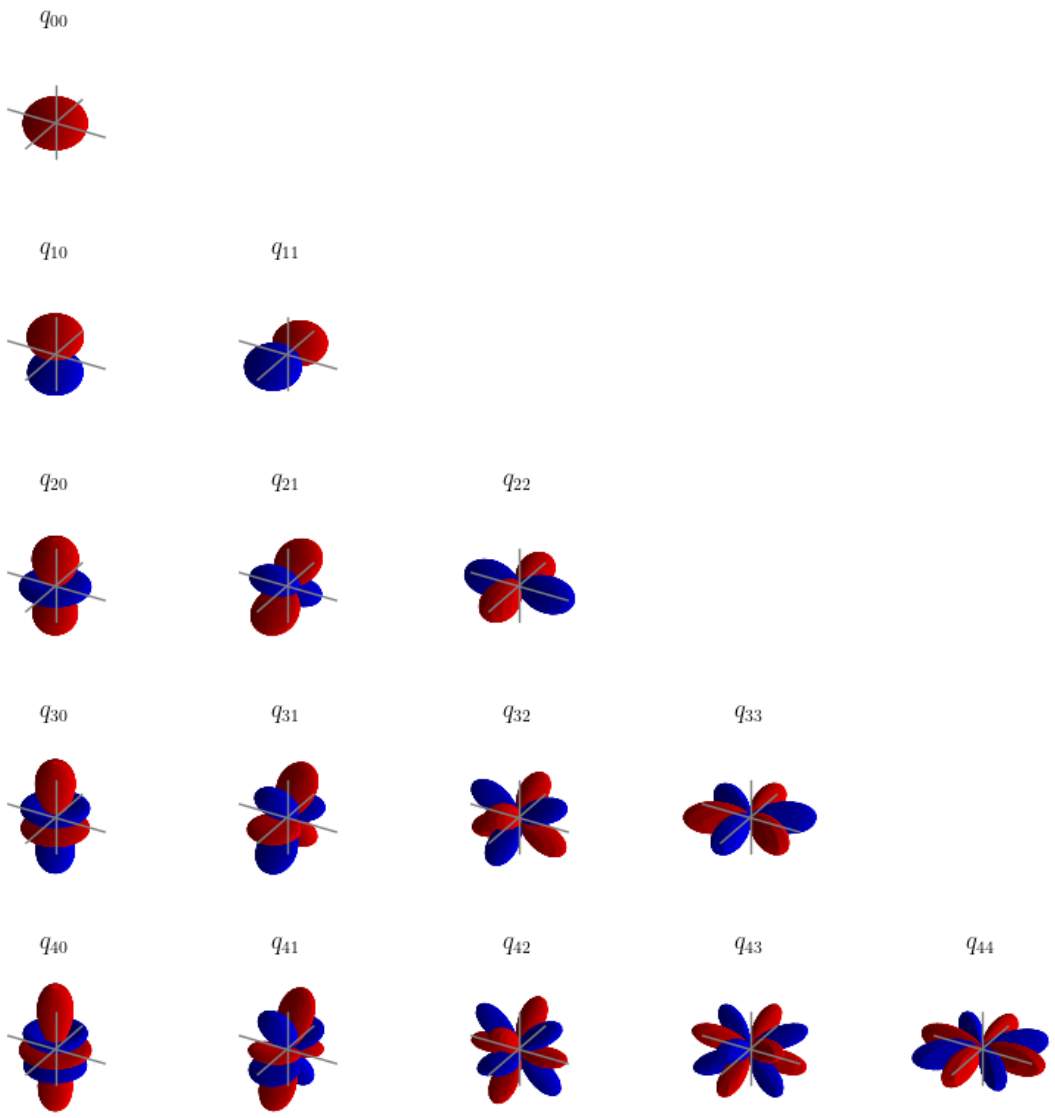

Figure B.1: Visualization of mass distribution associated with the multipole moments; red high density and blue low density regions. `SciPy` was used to calculate the spherical harmonics.